

---

# High-power femtosecond laser-oscillators for applications in high-field physics

Jonathan Brons

---



München 2017



---

# High-power femtosecond laser-oscillators for applications in high-field physics

Jonathan Brons

---

Dissertation  
an der Fakultät für Physik  
der Ludwig-Maximilians-Universität  
München

vorgelegt von  
Jonathan Brons  
aus Krefeld

München, den 24.02.2017

Erstgutachter: Prof. Ferenc Krausz

Zweitgutachter: Prof. Uwe Morgner

Tag der mündlichen Prüfung: 23.03.2017

# Zusammenfassung

In dieser Doktorarbeit werden experimentelle Anstrengungen zur Entwicklung eines kompakten Laseroszillators für Femtosekundenimpulse mit hoher Durchschnitts- und Spitzenleistung beschrieben. Dabei zielt dieser Laser auf neuartige Anwendung in der Spektroskopie und Hochfeldphysik ab, insbesondere dem Antreiben von ineffizienten Frequenzkonversionsprozessen wie der Erzeugung von mittlerer Infrarot- und extrem ultravioletter Strahlung. Die entwickelten Strahlquellen bestehen dabei aus einem kerrlinsenmodengekoppelten Hochleistungsscheibenlaser auf Basis von Yb:YAG mit mehreren MHz Wiederholrate und einer anschließenden Impulskompressionsstufe aus massiven Festkörpern.

Es wird aufgezeigt, dass Kerrlinsenmodenkopplung sowohl durchschnitts-, als auch spitzenleistungsskalierbar ist und die derzeit einzige Methode zur Modenkopplung, die simultan die effiziente Ausbeute der gesamten Verstärkungsbandbreite des Verstärkungsmediums zulässt. Impulse mit mehr als 60 MW Spitzenleistung und hunderten Watt an Durchschnittsleistung können direkt am Oszillatorausgang erreicht werden mit Impulslängen bis hinab zu 140 fs.

Der Hochleistungsoutput des Oszillators wurde in massiven Festkörpermaterialien spektral verbreitert, um die Durchführbarkeit eines effizienten, kompakten und robusten Impulskompressors auszuloten, der sich nicht auf justageempfindliche Fasern verlassen muss. Gestützt durch frühere Arbeiten, sowie neue Experimente, als auch Simulationen konnte festgestellt werden, dass die Nachahmung eines nichtlinearen Quasiwellenleiters zu außerordentlich hoher Effizienz im Durchsatz führen und dabei herausragende Komprimierbarkeit über dem gesamten Strahl sicherstellen kann. Die Impulse mit 60 MW Spitzen- und 150 W Durchschnittsleistung aus einem der entwickelten Oszillatoren wurden in einem sehr kompakten Quasiwellenleiter spektral verbreitert und anschließend mit geschirpten Spiegeln auf 30 fs komprimiert. Durch die hohe Transmission des gesamten Aufbaus von 95 % wurde die Spitzenleistung auf 230 MW hochgetrieben. Simulationen zeigen die Umsetzbarkeit eines Kompressors auf Basis dieser Wellenleiter mit Pulsdauern, die mit 10 fs bis in den Bereich weniger optischer Schwingungszyklen hineinreichen. Untersucht wurde ebenfalls ein anderer Ansatz zur spektralen Verbreiterung, der auf kaskadierten  $\chi^{(2)}$  Nichtlinearitäten während der Erzeugung der zweiten Harmonischen in BBO mit fehlangepasster Phase beruht. Obgleich die Effizienz nicht vergleichbar mit der des Wellenleiteransatzes ist, machen ihn die faszinierende Möglichkeit zu defokussierenden Phasenschüben und Selbstkompression im Kristall zu einem interessanten Ausgangspunkt für sehr kompakte Impulskompressionsaufbauten.

Das Zusammenspiel dieser Entwicklungen zeigt die Realisierbarkeit von unverstärkten, einfachen und kompakten Laserquellen auf, die komplexere und preisintensive Yb- oder Ti:Safir Verstärkersysteme ersetzen können.



# Abstract

This thesis describes experimental work in the development of a compact, high average and peak-power femtosecond oscillator. This laser targets new applications in spectroscopy and high-field physics, especially the driving of inefficient frequency-conversion-processes like the generation of mid-infrared and extreme ultraviolet radiation. The developed sources consist of a high-power Kerr-lens mode-locked Yb:YAG thin-disk oscillator with multi-MHz repetition rate and a subsequent all-bulk pulse-compression stage.

It is shown that Kerr-lens mode-locking is both average and peak-power scalable and is currently the only mode-locking technique that at the same time allows the efficient use of the full gain-bandwidth of the amplifying medium. Pulses with more than 60 MW peak-power and hundreds of watts in average power can be reached as direct oscillator output with down to 140 fs pulse-duration.

The high-power output from the oscillators was spectrally broadened in bulk solids to explore the feasibility of an efficient, compact and robust pulse-compressor that does not have to rely on alignment-sensitive fibers. Leaning on previous work as well as new experiments and computer simulations it was found that the emulation of a nonlinear quasi-waveguide can yield exceptionally high throughput efficiency, while retaining excellent whole-beam compressibility. The 60 MW peak- and 150 W average power pulses from a developed oscillator were spectrally broadened in a very compact quasi-waveguide and subsequently compressed with chirped mirrors to 30 fs pulse duration. By virtue of the 95 % transmission of the whole setup the peak-power was boosted to 230 MW. Simulations show the feasibility of a waveguide based compressor with down to 10 fs pulse duration into the few-optical-cycle regime. A different approach to spectral broadening, relying on cascaded  $\chi^{(2)}$  nonlinearities from phase-mismatched second-harmonic generation in BBO was also investigated. Although the efficiency is not comparable to the waveguide approach, the intriguing possibility of defocusing phase-shifts and self-compression in the crystal make it an interesting starting point for very compact pulse-compression setups.

The combination of these developments demonstrates the feasibility of non-amplified, simple and compact laser sources that can replace more complex and costly Yb or Ti:Sapphire amplifier systems.



## Selected publications

- *J. Brons*, V. Pervak, D. Bauer, D. Sutter, O. Pronin, and F. Krausz, "Powerful 100-fs-scale Kerr-lens mode-locked thin-disk oscillator," *Opt. Lett.* 41, 3567 (2016)
- M. Seidel, G. Arisholm, *J. Brons*, V. Pervak, and O. Pronin, "All solid-state spectral broadening: an average and peak power scalable method for compression of ultrashort pulses," *Opt. Express.* 24, 9412–9428 (2016)
- *J. Brons*, V. Pervak, E. Fedulova, D. Bauer, D. Sutter, V. Kalashnikov, A. Apolonskiy, O. Pronin, and F. Krausz, "Energy scaling of Kerr-lens mode-locked thin-disk oscillators," *Opt. Lett.* 39, 6442–6445 (2014)
- O. Pronin, *J. Brons*, C. Grasse, V. Pervak, G. Boehm, M.-C. Amann, A. Apolonski, V. L. Kalashnikov, and F. Krausz, "High-power Kerr-lens mode-locked Yb:YAG thin-disk oscillator in the positive dispersion regime," *Opt. Lett.* 37, 3543–3545 (2012)
- O. Pronin, *J. Brons*, C. Grasse, V. Pervak, G. Boehm, M.-C. Amann, V. L. Kalashnikov, A. Apolonski, and F. Krausz, "High-power 200 fs Kerr-lens mode-locked Yb:YAG thin-disk oscillator," *Opt. Lett.* 36, 4746–4748 (2011)

A complete list can be found on page 125.



# Contents

<b>Zusammenfassung</b>	<b>i</b>
<b>Abstract</b>	<b>iii</b>
<b>Selected publications</b>	<b>v</b>
<b>1. Introduction</b>	<b>1</b>
<b>2. Mode-locking fundamentals</b>	<b>5</b>
2.1. Laser pulse formation . . . . .	5
2.2. Soliton pulse-propagation . . . . .	7
2.2.1. Dispersion . . . . .	7
2.2.2. Self-phase-modulation . . . . .	8
2.2.3. Fundamental soliton . . . . .	9
2.3. Solitonic mode-locking . . . . .	10
2.3.1. Gain, spectral filtering and loss . . . . .	10
2.3.2. Self-amplitude modulation . . . . .	11
2.3.3. Master equation of mode-locking . . . . .	12
2.3.4. Different dispersion regimes and power scaling . . . . .	13
<b>3. Power scaling of Kerr-lens mode-locked thin disk oscillators</b>	<b>15</b>
3.1. Yb:YAG thin disk . . . . .	15
3.2. Resonator design . . . . .	16
3.2.1. Static resonator section . . . . .	17
3.2.2. Nonlinear resonator section . . . . .	20
3.3. Power-scaling experiments . . . . .	24
3.3.1. Geometrical power-scaling scheme . . . . .	24
3.3.2. Oscillator setup . . . . .	26
3.3.3. ROC scaling . . . . .	32
3.3.4. Influence of dispersion . . . . .	34
3.3.5. Output coupling . . . . .	35
3.4. Triple-pass with large output-coupler transmission . . . . .	36
3.5. Intra-cavity nonlinearities and further power scaling . . . . .	39
3.5.1. Intensity noise . . . . .	43
3.5.2. Influence of air . . . . .	43
3.5.3. Influence of the Kerr-medium . . . . .	48
3.6. Front end for an all thin-disk OPCPA system . . . . .	49
3.7. Summary . . . . .	52

<b>4. Broadband oscillators: the case for Yb:YAG</b>	<b>55</b>
4.1. Yb:CaGdAlO <sub>4</sub> oscillator . . . . .	57
4.1.1. Disk testing and single-mode cavity . . . . .	57
4.1.2. Mode-locking starting issues . . . . .	59
4.2. Distributed Kerr-lens mode-locking . . . . .	60
4.3. Summary . . . . .	61
<b>5. Scalable pulse-compression techniques</b>	<b>63</b>
5.1. Spectral broadening in bulk $\chi^{(3)}$ material . . . . .	66
5.1.1. Self-focusing geometry . . . . .	68
5.1.2. Materials for high power spectral broadening . . . . .	68
5.1.3. Single window broadening . . . . .	69
5.1.4. Nonlinear quasi-waveguide broadening . . . . .	75
5.1.4.1. Waveguide design principles . . . . .	76
5.1.4.2. Simulation of the spatial-spectral homogenization . . . . .	76
5.1.4.3. Compression in a first stage . . . . .	79
5.1.4.4. Compression in a second stage . . . . .	81
5.2. Cascaded $\chi^{(2)}$ nonlinearities . . . . .	86
5.2.1. Spectral broadening with type-I SHG in BBO . . . . .	87
5.2.2. 2-stage compression with $\chi^{(3)}$ and cascading $\chi^{(2)}$ processes . . . . .	91
5.3. Summary . . . . .	96
<b>6. Summary and conclusion</b>	<b>97</b>
<b>A. Appendix</b>	<b>99</b>
A.1. Ray transfer matrices for cavity analysis with a Kerr-lens . . . . .	99
A.2. Numerical mode-calculations with hard-aperture diffraction . . . . .	100
A.3. Solution of the nonlinear wave equation . . . . .	101
A.4. Long-arm autocorrelator . . . . .	103
<b>Bibliography</b>	<b>105</b>
<b>List of publications</b>	<b>125</b>
<b>Data archiving</b>	<b>127</b>
<b>Danksagung</b>	<b>129</b>

# List of Tables

3.1. Pulse-duration dependence on the hard aperture size . . . . .	23
3.2. Material properties of utilized Kerr-media . . . . .	48
3.3. Parameters of the developed KLM oscillators . . . . .	53
4.1. Broadband gain materials and properties . . . . .	56
5.1. Spectral broadening techniques and corresponding typical peak-power ranges . . . . .	64
5.2. Subjective rating of material properties with respect to high power spectral broadening. . . . .	69
5.3. Single-window compression results . . . . .	74
5.4. Waveguide compression results . . . . .	85
5.5. Second harmonic power generated for changing tuning-angle . . . . .	90
5.6. BBO compression results . . . . .	95
A.1. Important ray-transfer matrices. . . . .	100
A.2. Sellmeier coefficients for fused silica . . . . .	103



# List of Figures

1.1. State of the art, high-power mode-locked laser oscillators. . . . .	3
2.1. Circulating pulses in a laser oscillator. . . . .	5
2.2. Illustration of mode-locking . . . . .	6
2.3. Self-amplitude modulation via the Kerr-effect. . . . .	7
2.4. Effect of self-phase-modulation on instantaneous frequency. . . . .	9
2.5. Perfectly saturable and cubic-quintic modulation. . . . .	12
2.6. Sequential model for mode-locking of oscillators. . . . .	12
3.1. Thin disk concept. . . . .	16
3.2. Gain cross-section of Yb:YAG. . . . .	17
3.3. Stability zone shrinking with thin disk passes. . . . .	19
3.4. Focusing section with Kerr-medium. . . . .	21
3.5. KLM sensitivity. . . . .	21
3.6. Saturation parameters for different hard aperture sizes. . . . .	22
3.7. Simulated power transmission for combined hard and “soft” aperture	23
3.8. Geometrical power-scaling . . . . .	25
3.9. Simulated SAM-parameters for different focusing arrangements. . . .	25
3.10. Oscillator sketch for mode-size scaling. . . . .	26
3.11. Mode size distributions inside the KLM resonator. . . . .	27
3.12. Design curves of the utilized HD mirror coatings. . . . .	28
3.13. Thermal images of HD mirrors. . . . .	29
3.14. Disk fluorescence images and output beam-profiles for CW and ML operation. . . . .	31
3.15. Mode-locking instabilities. . . . .	32
3.16. Method to choose comparable focal spot size of the CW mode. . . .	32
3.17. Intensity autocorrelation and spectrum of 900 mm ROC oscillator. . .	33
3.18. Geometrical peak-power scaling. . . . .	34
3.19. Influence of GDD on intracavity peak power. . . . .	35
3.20. Dependence of pulse duration, peak power and output power on output coupler transmission. . . . .	36
3.21. Double-pass oscillator . . . . .	37
3.22. Triple-pass oscillator. . . . .	37
3.23. Sketch of double-pass, reference oscillator and triple-pass oscillator. .	37
3.24. Autocorrelation signal and Spectrum of the 30% OC triple-pass. . .	38
3.25. Extra-, intra-cavity peak power and opt.-opt. efficiency comparison of triple-pass and double-pass reference-cavity for various output-coupler transmissions. . . . .	38

3.26. Triple-pass folding-mirrors in front of the thin-disk module. . . . .	39
3.27. Polarization-dependent spectra with quartz Kerr-medium. . . . .	40
3.28. 2000 mm ROC oscillator sketch. . . . .	41
3.29. Autocorrelation and spectrum for varying KM and GDD values. . .	41
3.30. Autocorrelation and spectrum of 1.5 m ROC-oscillator. . . . .	42
3.31. Extended geometrical peak-power scaling. . . . .	44
3.32. RF-carrier signal of the 2 m ROC oscillator. . . . .	44
3.33. Intensity noise of the 1.5 m ROC oscillator. . . . .	45
3.34. Contribution of the Kerr-plate to the nonlinear phase-shift for varying atmospheric pressure. . . . .	46
3.35. Dependence of peak power and pulse duration on air pressure. . . .	47
3.36. Spectra for varying air pressure. . . . .	48
3.37. Spiking during initiation of KLM. . . . .	50
3.38. Spectra of pulses for different Kerr-medium positions. . . . .	50
3.39. Intra-cavity peak-power in dependence of Kerr-medium position. . .	51
3.40. OPCPA setup seeded by a KLM thin-disk oscillator. . . . .	52
3.41. Layout of the 13MHz seed oscillator. . . . .	52
3.42. Spectrum, FROG-retrieved pulse-shape and beam-profile of the 13 MHz seed-oscillator. . . . .	53
3.43. Average power stability of the TD KLM seed oscillator. . . . .	53
4.1. Gain and emission cross-sections of Yb:YCOB and Yb:CaF. . . . .	56
4.2. Emission spectra of Yb:CALGO . . . . .	57
4.3. Yb:CALGO thin-disk with speckle structures and CW output in multi-mode and single-mode operation. . . . .	58
4.4. 40 MHz Yb:CALGO oscillator setup. . . . .	59
4.5. Spectrum and beam-profile of free-running Yb:CALGO oscillator. . .	60
4.6. Sketch of the 200MHz DKLM oscillator. . . . .	61
5.1. Intensity profiles with prominent self-diffraction due to self-focusing. .	67
5.2. Self-focusing geometry. . . . .	68
5.3. Integrated output spectra for different pulse energies focused into a 10mm thick sapphire crystal. . . . .	70
5.4. 126 fs Autocorrelation trace before and after first compression stage. .	71
5.5. Beam-profile of spectrally broadened pulses before and after spatial filtering. . . . .	71
5.6. Spectra of the two stage, single crystal pulse compressor. . . . .	72
5.7. Spectral broadening in a sequence of windows. . . . .	72
5.8. Spectral broadening with several windows in a single focus. . . . .	73
5.9. Sketch of a lens- or waveguide for nonlinear spectral broadening. . .	75
5.10. Simulated spatial homogeneity after pulse propagation through the nonlinear waveguide. . . . .	77
5.11. Simulated fluence and intensity profiles after 10 waveguide passes. . .	78
5.12. Simulations for varying stability-parameter of the waveguide. . . . .	79
5.13. Simulations for varying nonlinear phase-shift per pass through the waveguide. . . . .	80

5.14. Sketch of waveguide compression stage . . . . .	80
5.15. Calculated mode-size distribution in the utilized waveguide with and without Kerr-lens. . . . .	81
5.16. M-square beam-quality and beam-shape in focus after the first waveguide-pass. . . . .	81
5.17. Simulated and measured spectrum after the first waveguide. . . . .	82
5.18. M-square beam-quality and beam-shape in focus after the second waveguide. . . . .	82
5.19. Measured and FROG-retrieved spectra after second waveguide. 30 fs autocorrelation of the compressed output pulse . . . . .	83
5.20. Measured and retrieved FROG traces after the second pass through the waveguide . . . . .	84
5.21. RF intensity noise spectrum before and after the waveguide. . . . .	84
5.22. Simulated spectrum and Fourier-limited pulse after 30-pass waveguide with dispersion-compensation. . . . .	85
5.23. Fundamental wave transmission through phase-mismatched type-I SHG. Evolution of nonlinear phase-shift along crystal. . . . .	87
5.24. Fundamental wave depletion and saturation of the nonlinear phase-shift with input irradiance. . . . .	88
5.25. Measurement setup for spectral homogeneity after focusing into BBO. . . . .	89
5.26. Measured Fourier-transform limits of broadened spectra for different iris-openings and defocusing phase-mismatch. SH-tuning around phase-matching angle. . . . .	89
5.27. Far-field beam-profiles after spectral broadening in BBO. . . . .	90
5.28. Spatially apertured, broadened spectrum measured for different iris openings. . . . .	91
5.29. Two stage compression setup with quartz and BBO. . . . .	92
5.30. Broadened spectrum after a second broadening stage with BBO. . . . .	93
5.31. Bandpass-filtered beam-profiles after second stage compression using BBO. Beam-profile in the focus. . . . .	93
5.32. Spectrum and autocorrelation traces after the oscillator, after the first and after the second (BBO) compression stage. . . . .	94
5.33. Fractured parts of two different BBO crystals. . . . .	95
A.1. Comparison of ray-transfer-matrix and Fox-Li mode calculation. . . . .	101
A.2. Setup and beam-path of the long-arm autocorrelator. . . . .	104



# List of Abbreviations

ADR	Anomalous Dispersion Regime with net negative (-) group delay dispersion.
AOM	Acousto-optic modulator
BBO	beta-barium borate
CE	Carrier-envelope.
CW	continuous wave
DFG	Difference-frequency generation
DFG	Difference-frequency generation
DKLM	Distributed Kerr-lens mode-locking
fs	Femtosecond
FTL	Fourier transform limit
FW	Fundamental wave
FWHM	Full-width-half-maximum
GDD	Group-delay-dispersion
HA	Hard aperture
HD	Highly dispersive
HHG	High-harmonic generation.
HR	High reflectivity (mirror)
KLM	Kerr-lens mode-locking.
mid-IR	Mid-infrared.
NDR	Normal Dispersion or Chirped Pulse Regime with net positive (+) dispersion.
NEE	Nonlinear envelope equation
OC	Output coupler
OPCPA	Optical parametric chirped pulse amplifier
PCF	Photonic crystal fiber

- RF Radio-frequency
- ROC Radius of curvature
- SAM Self-amplitude modulation
- SESAM Semiconductor saturable absorber mirror
- SEWA Slowly evolving wave approximation.
- SH Second harmonic
- SH-FROG Second-harmonic frequency resolved optical gating
- SHG Second harmonic generation.
- SPM Self-phase-modulation
- TD Thin-disk.
- Ti:Sa Titanium:Sapphire.
- TOD third-order-dispersion
- VBG Volume-Bragg-grating

# 1. Introduction

Since the first demonstration in a gas laser in 1964 [1] different techniques of mode-locking have enabled the direct generation of pulses as short as a few femtoseconds (fs). The transition from the early dye to solid-state media led to an increase of the power output as well as the reliability of the laser-systems such that today ultra-short pulse lasers have become a tool for applications in diverse fields among them e.g. precision-metrology [2], femtochemistry [3], telecommunication [4], multi-photon and cars-microscopy [5, 6] or eye-surgery [7]. While for some of these applications low pulse-energy (typ. few nJ) and moderate peak-power is sufficient or even necessary, others, especially including inefficient spectral conversion-processes, require high repetition-rates as well as high average and peak-power. A prominent example is high-harmonic generation (HHG) by which attosecond pulses can be generated [8]. It relies on tunnel-ionization of noble-gases and requires field-strengths similar to the atomic binding-potential with peak-intensities on the order of  $10^{14} \text{ W/cm}^2$ . Today, pulses that can fulfill such demands are routinely provided by Titanium:sapphire (Ti:Sa) amplified laser systems working up to kHz pulse repetition rate while providing pulses with GW - TW peak-power. Another important example is mid-infrared (mid-IR) generation. Bright, coherent radiation, possibly frequency combs in the mid-IR spectral 'fingerprint' region (2 - 20  $\mu\text{m}$ ) where most molecules exhibit vibrational transitions is also highly sought-after for spectroscopic applications [9]. High power, MHz sources of near-infrared pulses can provide relatively high-power, broadband coverage of a large portion of the mid-IR via difference-frequency generation (DFG) or parametric amplification [10, 11].

Broadband, ultrashort pulse Ti:Sa lasers have been the workhorse in many laboratories since the first observation of Kerr-lens mode-locking (KLM) in 1990 [12]. However, Ti:Sa technology is difficult and expensive to scale in average power<sup>1</sup>, so far precluding the combination of MHz repetition-rates and high pulse-energy (multi- $\mu\text{J}$ ) for improved signal-to-noise ratio. High-power alternatives are found in Yb-doped gain materials, primarily in the form of fiber-, innoslab- and thin-disk (TD) amplifiers, all of which have been shown to handle kW-level average power efficiently [13, 14, 15]. Particularly the thin-disk geometry, due to its minimized interaction-length with the pulse, is useful for reaching relevant peak-powers at MHz rate without the need for further amplification. Their implementation in power-scalable femtosecond oscillators has potential to reduce cost and size as well as to improve the noise performance over amplified systems.

**State of the art high-power ultrafast laser oscillators** The best performing material today is Yb:YAG due to its excellent thermal and mechanical properties,

---

<sup>1</sup>Partly due to a lack of powerful laser-diodes in the Ti:Sa absorption band.

broadband pump-absorption for high-power diode-lasers and not least, availability in superior crystal quality brought about by industrial demands. In 2000 the first thin-disk oscillator based on Yb:YAG [16] was mode-locked with a semiconductor saturable absorber mirror (SESAM) [17] and provided pulses near 700 fs duration. Subsequent developments came to the conclusion that intra-cavity nonlinearities, including the atmosphere, are necessary to allow further energy-scaling<sup>2</sup> in combination with very strong dispersion-compensation. This resulted in pulse-energies up to 80  $\mu\text{J}$  [20], however, with pulse-durations far removed from the bandwidth limitations of the gain material ( $\sim 9$  nm for Yb:YAG).

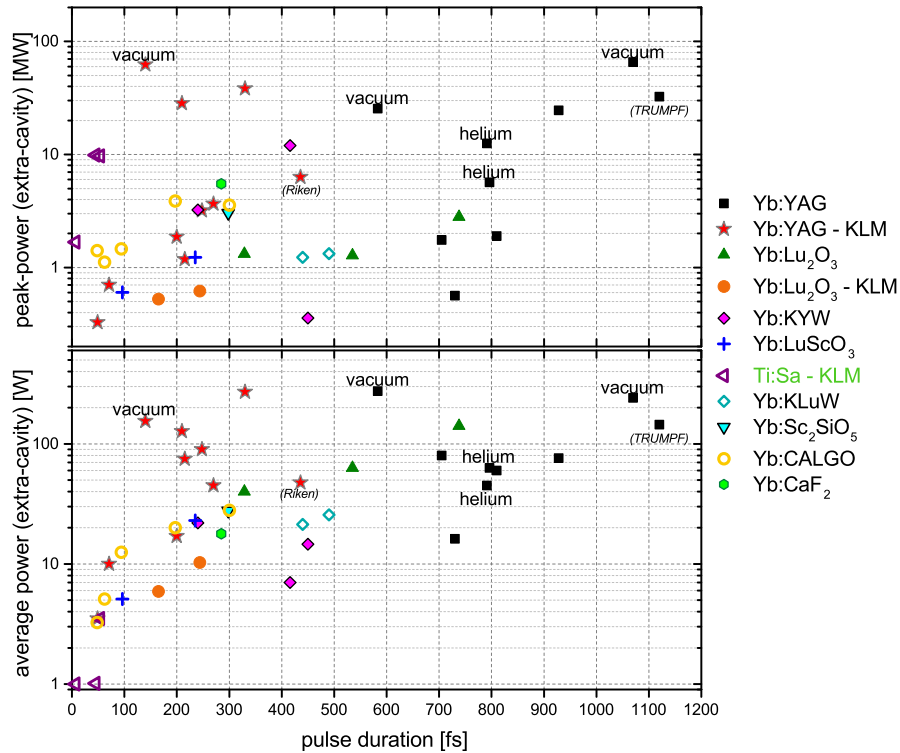
The first demonstration of a Kerr-lens mode-locked thin-disk oscillator in 2011 [21] showed that much shorter pulses could be produced than with SESAM, which is the key feature of this technique. In addition, so far the only high-power thin-disk oscillator for which carrier-envelope (CE) frequency stabilization has been demonstrated was Kerr-lens mode-locked [22]. CE-phase stabilization is obligatory for frequency-comb metrology or attosecond pulse generation. The first aim of this thesis is to demonstrate the power-scalability of multi-MHz thin-disk oscillators using Kerr-lens mode-locking for the shortest possible pulse-durations and exploiting the full emission bandwidth of Yb:YAG ( $< 200$  fs). Peak-powers should approach the 100 MW regime. The corresponding experiments are presented in chapters 3 and 4.

Figure 1.1 displays the peak- and average power performance of state of the art, ultrafast laser-oscillators keyed by gain-material. The results from this thesis, all achieved with Kerr-lens mode-locking, are already included and constitute the shortest pulses generated with Yb:YAG thin-disk oscillators so far.

**State of the art high-power spectral broadening techniques** While Yb-based gain media, especially Yb:YAG, have proven an outstanding platform for high power oscillators, they lack the amplification-bandwidth of Ti:Sa. If Yb gain media are to replace Ti:Sa technology this deficiency has to be overcome by pulse-compression techniques that rely on cavity-external spectral broadening. This is usually done in fibers, which, however do not always prove the most practical solution for the high average and moderate peak-power combination obtained from oscillators. Solid-core photonic crystal fibers offer large broadening factors with reasonable average power handling. This allowed the compression of 4 MW peak-power pulses to 23 fs duration with 250 W average and 34 MW peak-power via a large-mode-area fiber [51]. Not limited by the self-focusing threshold of solids, peak-powers much larger than 4 MW can be launched in gas-filled hollow fibers. Krypton-filled, hollow-core photonic-crystal (Kagomé) fibers have been employed to compress 30 MW peak-power pulses to 31 fs duration with 140 MW peak-power and 76 W average power throughput. Gas-filled capillaries are routinely used to compress the output of high peak-power amplifier systems to the few cycle-regime [52]. Recently this technique has been demonstrated with input average powers as high as 660 W (0.52 mJ pulse energy, 240 fs duration) to yield 6.3 fs long pulses with 17 GW peak-power and 216 W average power throughput [53].

---

<sup>2</sup>With the exception of [18, 19] where high output-coupling ratios were the key.



**Figure 1.1.** – Peak- and average power from state of the art, high-power oscillators. All have been mode-locked using SESAM except those indicated otherwise. All but one (Riken) of the listed KLM oscillators were developed within the research-group at LMU/MPQ. References: (Yb:YAG SESAM) [16, 23, 24, 18, 25, 26, 19, 27, 20] and (Yb:YAG KLM) [21, 28, 29, 30, 31, 32], (Yb:Lu<sub>2</sub>O<sub>3</sub>) [33, 34], (Yb:Lu<sub>2</sub>O<sub>3</sub> KLM) [35], (Yb:KYW) [36, 37, 38], (Yb:LuScO<sub>3</sub>) [39, 40], (Yb:KLuW) [41, 40], (Yb:Sc<sub>2</sub>SiO<sub>5</sub>) [42], (Yb:CALGO) [43, 44, 45, 46], (Yb:CaF<sub>2</sub>) [47], (Ti:Sa - normal dispersion) [48, 49], (Ti:Sa anomalous dispersion) [50].

Other than fibers, bulk solids can also be employed. With a combination of fiber and bulk spectral broadening, 7.7 fs long pulses with a peak-power of 10 MW and 6 W average power were generated from a KLM thin-disk oscillator (1.1  $\mu$ J pulse energy, 250 fs duration) [22]. Cascades of very thin silica plates have been used recently to demonstrate supercontinuum generation, in particular yielding 0.13 TW peak-power with 5.4 fs long pulses from an amplifier system (0.8 mJ pulse energy, 30 fs duration) [54]. Very efficient (91 %), high average power compression was demonstrated by using a multi-pass setup where pulses with 850 fs duration and 41 MW peak-power were passed 38 times through a quasi-waveguide containing fused silica windows. The pulses could be compressed to 170 fs duration yielding 160 MW peak-power with an average power throughput of 375 W. The use of cascaded  $\chi^{(2)}$  processes, such as phase-mismatched second harmonic generation (SHG) has enabled pulse compression with additional degrees of freedom by choosing and tuning the sign and magnitude of the effective nonlinear interaction [55, 56]. Recently type-I SHG was used for compressing the 19 MW peak-power pulses (190 fs duration) from a KLM thin-disk oscillator with 100 W average power [57]. By virtue of self-defocusing nonlinear phase-shifts the setup showed 75 % throughput efficiency and the pulses were compressed to 30 fs, yielding 75 MW peak-power.

The second aim of this thesis was the identification of a scheme for efficient average power scalable spectral broadening that would be best suited for the developed oscillators. The scheme preferably should rely only on bulk materials for maximum robustness. The corresponding experiments are presented in chapter 5.

## 2. Mode-locking fundamentals

### 2.1. Laser pulse formation

Laser pulses are formed inside the resonator of an oscillator. In the simplest case it consists of two mirrors that trap light and shape the longitudinal and transversal modes of the oscillator. A gain medium transfers power into the modes and replenishes losses e.g. due to an output-coupler that transmits a portion of the circulating light.

The oscillator can be persuaded to concentrate the light-energy into a short time-window by several means.

The method of q-switching involves an active or passive modulation of the cavity-losses. During the period of high losses, little or no light circulates in the resonator and the gain of the amplifying medium rises. As the resonator-losses are suddenly decreased, the stored energy in the gain medium is released into a pulse with typically mJ energy and  $\mu\text{s}$  - ns duration until the gain is depleted. The loss modulation, happening on the time-scale of the round-trip time, can be realized actively with electro- or acousto-optical switches or with passive saturable absorbers such as e.g. SESAM [17].

Much shorter pulses are obtained with mode-locking.

**Mode-locking** The longitudinal modes of the resonator oscillate only with integer multiples of the repetition-frequency  $f_{rep}$  which is related to the total round-trip length  $2l_r$  by

$$f_{rep} = \frac{c}{2l_r}$$

with the speed of light  $c$ . Superposition of these resonant, equidistant modes creates an interference-pattern in the time domain. In the ideal case of a fixed phase-relation between all of the modes, single pulses can be formed that are separated by the roundtrip-time  $T_{rep} = f_{rep}^{-1}$  and whose width is inversely proportional to the number of coupled modes inside the oscillator:  $\tau_p \propto N^{-1}$ . In the case of a random phase-relation the light-field behaves like thermal noise and no pulses occur (see figure 2.2).

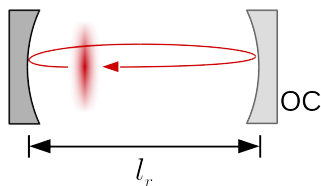


**Figure 2.1.** – Circulating pulses in a laser oscillator.

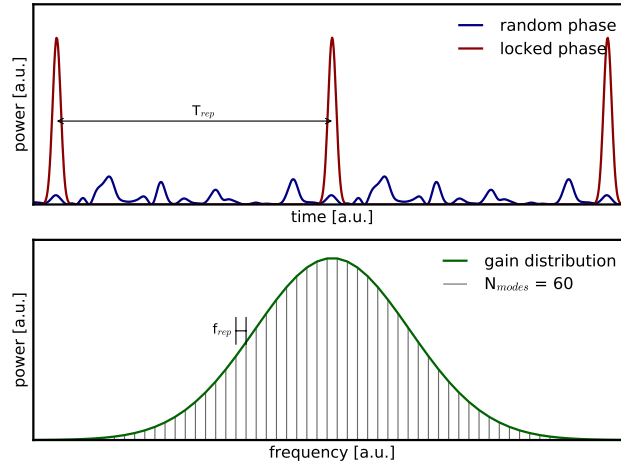


**Figure 2.2.** – (top) A fixed number of  $N_{modes}$  oscillator modes in the time domain producing either noise with random phases or distinct pulses with locked phases. (bottom)  $N_{modes}$  equally spaced modes with a Gaussian intensity distribution in the frequency domain.

Of course the spectral output from any laser is made up only of those longitudinal modes that experience net amplification in the gain-medium and are not filtered out by the finite bandwidth of other oscillator-elements. The larger the gain-bandwidth the more modes can oscillate and the shorter the achievable pulse-duration will be. Pulses as short as a few femtoseconds can be generated with broadband gain material like Ti:Sapphire.

The phase-relation between the modes is not fixed automatically but requires an amplitude- or phase-modulation to stabilize the locked modes. This modulation has to happen with the roundtrip-period of the oscillator. Active modulation was used for the first demonstration of mode-locking, however it is limited to the speed of electronic devices which are far removed from the femtosecond regime. A very prominent passive modulation technique with which femtosecond pulses can be generated is the semiconductor saturable absorber mirror (SESAM)[58, 17]. One or more semiconductor layers are embedded in a mirror-structure and bleach out when light is absorbed and electrons pushed into the conduction-band, thereby modulating the reflectivity of the mirror. However, their finite relaxation time on the order of 10-100 ps, as well as the real absorption in these devices make it very challenging to reach shortest pulses with high-power oscillators. Nonlinear passive modulation techniques such as Kerr-lens mode-locking are more suitable for short pulse-generation.

**Kerr-lens mode-locking** In KLM oscillators the amplitude modulation originates from a self-focusing Kerr-lens. The spatial variation of an intensity-profile  $I(r)$  induces a phase-profile  $\Delta\varphi(r)$  with transverse coordinate  $r$ . In a parabolic approximation (only valid near the beam-center) the phase-front change induced by a Gaussian beam resembles that of a thin lens  $\Delta\phi_{lens} = -\frac{2\pi}{\lambda} \frac{r^2}{f}$ . The Kerr-lens therefore has an

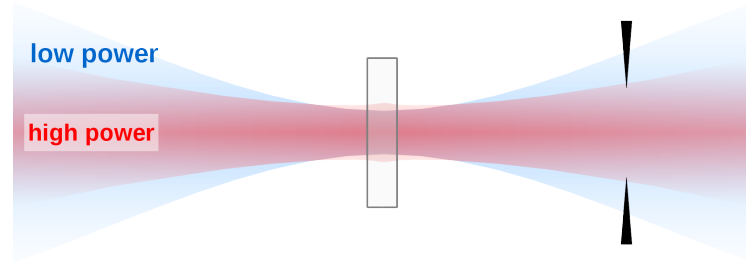


**Figure 2.3.** – Self-amplitude modulation via the Kerr-effect. The pulses see an intensity-dependent lens which changes the transmission through an aperture or the amplification via the gain-overlap.

approximate focal length

$$f_{kerr} = \frac{\pi w^4}{4n_2 P_{pk} L} \quad (2.1)$$

dependent on the peak power  $P_{pk}$ , the  $1/e^2$  beam radius  $w$  and the thickness of the material  $L$ . This approximation implies that the beam remains Gaussian after propagation through the lens. The nonlinear refractive index of nearly all transmissive materials only allows self-focusing lenses with  $n_2 > 0$ .

The exploitation of an intra-cavity Kerr-lens to the effect of mode-locking was first observed (accidentally) by Spence et al. [12] and the mechanism quickly identified by M. Piché et al. [59, 60, 61]. It allows a saturable-absorber-like action but with nearly instantaneous response and relaxation. Also, no real absorption takes place which makes the mechanism suitable for high intra-cavity powers even at strong modulation. The action of a Kerr-lens on the cavity-mode is illustrated in figure 2.3 where gain modulation can occur from a change in transmission through a hard aperture or the overlap between the pumped area/volume and the laser-mode (soft aperture).

## 2.2. Soliton pulse-propagation

The shortest achievable pulses in an oscillator can be formed and sustained in solitary lasers. A solitonic wave-packet does not change its temporal shape on propagation. To prepare the necessary conditions for laser-pulses to exhibit such behavior inside an oscillator one has to take into account the action of both dispersion as well as nonlinearities. Solitonic pulse propagation has been extensively investigated both theoretically and experimentally by numerous researchers and is canonically explained in most text-books (see e.g. [62, 63, 64, 65]).

### 2.2.1. Dispersion

A pulse is described as superposition of plane-wave solutions oscillating at different frequencies

$$E(z, t) = \int_{-\infty}^{\infty} \tilde{E}(\omega) \cdot e^{i(\omega t - \varphi(z, \omega))} d\omega \quad (2.2)$$

with a phase-relation  $\varphi(\omega) = k(\omega)z$ . The dispersion relation  $k(\omega) = \frac{\omega n(\omega)}{c}$  is given by the refractive index  $n(\omega) = \sqrt{1 + \chi^{(1)}(\omega)}$ , describing the material's linear polarization  $P = \epsilon_0 [\chi^{(1)}E + \chi^{(2)}E^2 + \chi^{(3)}E^3 + \dots]$ . This implies that light at different frequencies sees different optical path-lengths inside a medium. A Taylor expansion of  $\varphi(\omega)$  around the central frequency  $\omega_0$  yields the dispersion coefficients  $D_n$

$$\varphi(\omega) = \sum_{n=0}^{\infty} \left. \frac{\partial^n \varphi}{\partial \omega^n} \right|_{\omega_0} \frac{(\omega - \omega_0)^n}{n!} = \sum_{n=0}^{\infty} D_n \frac{(\omega - \omega_0)^n}{n!} \quad (2.3)$$

The effect of dispersion on a pulse can then be characterized by the different coefficients

- $D_1 = \left. \frac{\partial \varphi}{\partial \omega} \right|_{\omega_0}$  results in a linear frequency-dependence of the spectral phase and a time-shift of the pulse, namely with the group velocity  $v_g = \frac{\partial \omega}{\partial k}$ .
- $D_2 = \left. \frac{\partial^2 \varphi}{\partial \omega^2} \right|_{\omega_0}$  results in a quadratic frequency-dependence of the spectral phase and describes pulse broadening and a linear frequency-chirp in time. It is called *group-delay-dispersion* (GDD) and has the most important contribution to dispersive pulse-shaping in soliton mode-locked oscillators and pulse-compression for many-cycle pulses. For values of  $D_2 > 0$  the lower frequencies in the pulse have the fastest group-velocity and the pulse is said to be up-chirped, the lower frequencies arriving first (down-chirp for  $D_2 < 0$ ). The GDD is usually stated in the units  $fs^2$  and refers to the spectral phase-change due to an optical element or propagated distance. Contrary, the *group-velocity-dispersion* (GVD)  $\frac{\partial^2 k}{\partial \omega^2}$  describes the spectral phase-change per propagation-length and is often given in units of  $fs^2/mm$ .
- $D_n$  with  $n > 2$  can often be neglected for relatively narrowband pulses in unchirped solitonic oscillators. Third order dispersion (TOD,  $n = 3$ ) becomes important for broadband pulses and is a limiting factor for reaching shortest pulses in Ti:Sa oscillators. Fourth order dispersion ( $n = 4$ ) is often required for pulse-stretching/compression via gratings but can also be of considerable interest for dissipative soliton stability in chirped-pulse oscillators [66].

### 2.2.2. Self-phase-modulation

Apart from the usually negligible third harmonic-generation a third order nonlinear susceptibility  $\chi^{(3)}$  leads to an intensity-dependent refractive index  $n(I) = n_0 + n_2 I$ , giving rise to the self-focusing Kerr-effect as well as self-phase modulation (SPM). The time-scales on which the electronic polarization responds is on the order of few femtoseconds and can be treated as instantaneous for the relevant pulse-durations in this work.

When considering the time-dependent intensity-profile of a pulse, the same profile is imprinted on the pulse's temporal phase via the nonlinear refractive index of the

material and a phase-difference

$$\Delta\varphi(t) = -n_2 I(t) \cdot \frac{L\omega_0}{c} \quad (2.4)$$

The instantaneous frequency of an unchirped pulse then changes with time

$$\omega(t) = \omega_0 + \frac{d}{dt}\Delta\varphi(t) \quad (2.5)$$

and power is transferred into new frequency components. The effect is plotted in figure 2.4 for a  $sech^2$  shaped pulse and  $n_2 > 0$ <sup>1</sup>.

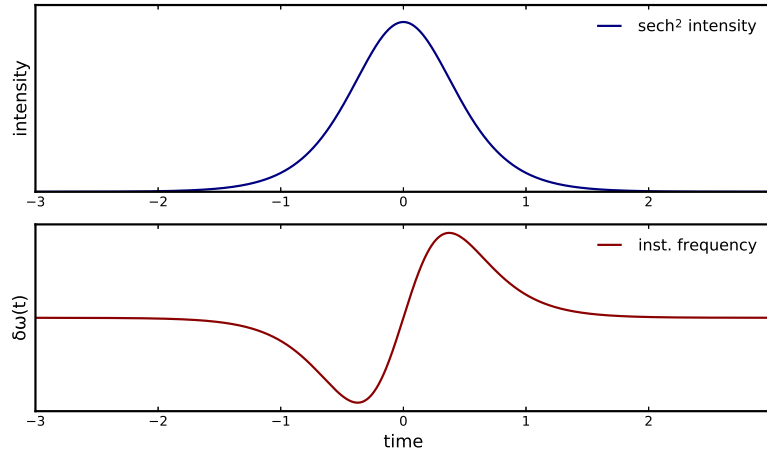


**Figure 2.4.** – Effect of self-phase-modulation on instantaneous frequency.

For Gaussian- or  $sech^2$ -pulses a linear up-chirp results with the newly created lower frequencies in the rising part of the pulse. This chirp can be compensated for by anomalous dispersion ( $D_2 < 0$ ). However, SPM does not necessarily lead to enhanced spectral width but can also produce spectral narrowing upon propagation in anomalously dispersive material or when an initial down-chirp exists [67, 68].

For single-mode Gaussian beams in oscillators one often defines the SPM-coefficient  $\gamma = \frac{2\pi}{\lambda} \int_0^L n_2 \frac{2}{\pi w^2(z)} dz = \frac{4n_2}{\lambda} \frac{L}{w_{eff}^2}$  along the propagation length. The maximum nonlinear phase-change is then estimated by just multiplying with the peak power and summing over all  $N$  cavity elements.

$$\Delta\varphi_{nl} = \sum_{i=0}^N \gamma_i P_{pk} \quad (2.6)$$

### 2.2.3. Fundamental soliton

The simplest case of propagation through a repeating waveguide or cavity with only  $\chi^{(3)}$  nonlinearity and GDD is described by the nonlinear Schrödinger equation 2.7 under the slowly varying envelope approximation.

<sup>1</sup>Nearly all transparent materials have  $n_2 > 0$  in the NIR region.

$$\frac{\partial}{\partial z} A = i \frac{D_2}{2} \frac{\partial^2}{\partial \tau^2} A - i \gamma |A|^2 A \quad (2.7)$$

Only the envelope  $A(z, \tau)$  of the field needs to be considered in the local pulse-frame  $\tau = t - z/v_{g,\omega_0}$ , traveling with the central group-velocity. The energy contained in the pulse is  $W = \epsilon_0 c n_0 \int_{-\infty}^{\infty} |A|^2 dt$ .

Requiring steady-state (constant phase-shift) equation 2.7 can be solved analytically and yields the unchirped, fundamental *sech* soliton in the case of  $D_2 < 0$

$$A(\tau) = A_0 \text{sech}(\tau/T) \quad (2.8)$$

where  $|A_0|^2$  is the peak power  $P_{pk}$  and  $T$  is the pulse-width.  $T$  is related to the full-width-half-maximum (FWHM) duration of the *sech*<sup>2</sup> pulse by  $T_{fwhm} = 1.76 \cdot T$ . This soliton solution is only possible when the linear frequency-chirp due to SPM is exactly canceled by anomalous GDD. Otherwise the pulse disperses and changes its shape. The solution can exist for pulse-energies  $W$  and pulse-durations  $T$  that fulfill the conditions

$$W = \frac{2|D_2|}{\gamma T} \quad (2.9)$$

and

$$T = \sqrt{\frac{|D_2|}{\gamma P_{pk}}} \quad (2.10)$$

### 2.3. Solitonic mode-locking

Additionally to SPM and dispersion the oscillator model must also include other elements such as gain, loss, spectral filtering and self-amplitude modulation (SAM). In order to avoid pulse destabilization the peak-power of the soliton,  $P_{pk}$ , has to stay below a certain threshold power [65, 66] which can strongly depend on the behavior of the SAM and the dissipative effects in the oscillator.

#### 2.3.1. Gain, spectral filtering and loss

The action of the gain medium and the linear loss  $l$  is approximately modeled via the contribution

$$\frac{\partial}{\partial z} A = \left( \frac{g_0}{1 + W/W_s} - l \right) A \quad (2.11)$$

Where  $g_0$  is the unsaturated gain and  $W_s$  the saturation-energy<sup>2</sup>.

The constant gain over the pulse-duration is a valid assumption for solid-state oscillators and their long upper-state lifetimes. Especially with the large saturation-fluences of Yb:YAG in the thin-disk geometry the gain saturates as a result of

<sup>2</sup>This simple form for the saturation-intensity is only valid in the limit of low pump intensity. The real saturation intensity is slightly higher[69].

average power and single-pass saturation is negligible. A more accurate model usually employed includes the temporal evolution of the gain  $g$  according to  $\partial_t g = (g - g_0)\tau_g^{-1} - g|A|^2 W_{sat}^{-1}$  with the effective upper-state lifetime  $\tau_g$ . For a pulse to be stable the net saturated gain  $g - l$  needs to be negative, such that only the high-power pulse sees amplification but not the CW-background.

The finite amplification bandwidth of the gain medium can be usually well described through a Lorentzian shape with bandwidth  $\Omega_g$  in the spectral domain and is a main source of spectral shaping/filtering. The filtering action can be expressed via a Taylor-expansion around  $\omega_0$  which reads in the time domain [70]

$$\partial_z A(z, \tau) \approx g(\omega_0) \left( 1 - 1/\Omega_g \partial_\tau + 1/\Omega_g^2 \partial_\tau^2 + \dots \right) A(z, \tau)$$

### 2.3.2. Self-amplitude modulation

Two models for the SAM are considered in theory.

- (i) The perfectly saturable absorber

$$q_{ps}(t) = \frac{\mu_{ps} \zeta_{ps} |A(t)|^2}{1 + \zeta_{ps} |A(t)|^2} \quad (2.12)$$

which describes the nonlinear gain modulation of a 'perfectly saturable' device with modulation depth  $\mu_{ps}$  and inverse saturation power  $\zeta_{ps}$ . This type of fast absorber model is used in prominent mode-locking theory [71], however with the linearized assumption, i.e. far from saturation such that  $q_{ps,lin}(t) = \mu_{ps} \zeta_{ps} |A(t)|^2$ .

- (ii) The 'cubic-quintic' nonlinear gain

$$q_{cq}(t) = \kappa(|A(t)|^2 - \zeta_{cq} |A(t)|^4) \quad (2.13)$$

with  $\kappa$  the inverse loss-saturation power. The effective modulation depth  $\mu_{cq}$  in the cubic-quintic case is reached at the power  $P_{max} = \frac{1}{2\zeta_{cq}}$  and has the value  $\mu_{cq} = \frac{\kappa}{4\zeta_{cq}}$ . This type of absorber is considered e.g. by V. Kalashnikov [66].

The perfectly saturable model (2.12) is best describing the effect of single hard aperture mode-locking (compare simulations in figure 3.6) while the cubic-quintic model seems a better approximation for the realistic case of several intra-cavity apertures, both hard or soft. Figure 2.5 illustrates the saturation behavior of these modulator-models with the instantaneous power. Simulations of the cavity-transmission with several hard apertures (see figure 3.7) support the cubic-quintic model for realistic cavities. The saturation of the SAM is very important in general to suppress q-switching or q-switched mode-locking [72, 73], a situation in which the mode-locked pulse-train is modulated by a periodic envelope that has a period of oscillation much longer than the repetition-rate of the oscillator. Such q-switched mode-locked pulses can, at the q-switch peak, exhibit much larger pulse-energy than the stable mode-locked soliton and lead to damage of the oscillator.

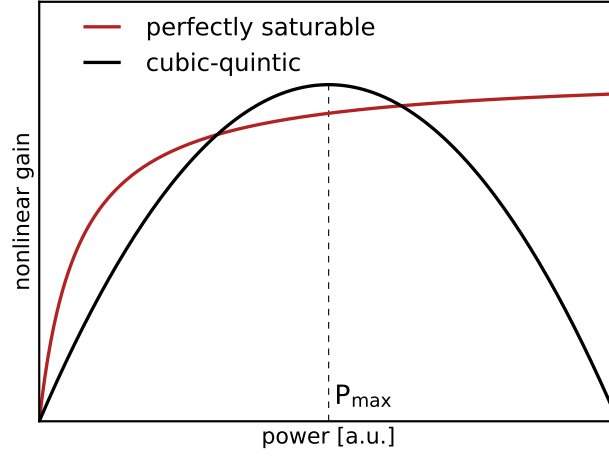


**Figure 2.5.** – Power modulation for *perfectly saturable* and *cubic-quintic* modulation.

### 2.3.3. Master equation of mode-locking

A master-equation of mode-locking, first introduced by Haus et al. [74], combines all relevant effects

$$\frac{\partial}{\partial z} A(z, \tau) = \left[ g - l + \frac{g}{\Omega_g^2} \frac{\partial^2}{\partial \tau^2} + \mathfrak{F}(|A|^2) \right] A(z, \tau) + i \left[ \frac{D_2}{2} \frac{\partial^2}{\partial \tau^2} - \gamma |A|^2 \right] A(z, \tau) \quad (2.14)$$

where  $\mathfrak{F}(|A|^2)$  describes the SAM and can be replaced either with the perfectly saturable (equation (2.12)) or the cubic-quintic saturable absorber model (equation (2.13)). Figure figure 2.6 illustrates the simplified sequential action of a single pass through the cavity on the propagating pulse.

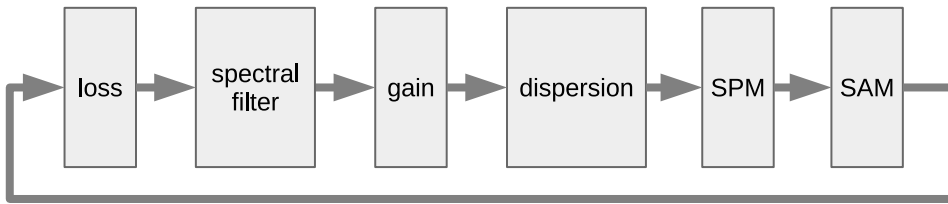


**Figure 2.6.** – Sequential model for mode-locking of oscillators.

In the non-dissipative approximation<sup>3</sup> with anomalous dispersion ( $D_2 < 0$ ) the fundamental soliton solution is

$$A_{adr}(\tau) = \sqrt{P_{pk}} \operatorname{sech}^2 \left( \frac{\tau}{T} \right) \quad (2.15)$$

<sup>3</sup>Negligible loss and gain, low spectral filtering, small, linear SAM.

The minimum achievable pulse duration  $T$  is in general strongly influenced by the SAM. By using a linearized, perfectly saturable absorber model an attempt at providing such a limit is given by [74, 75]

$$T_{fwhm} \propto \sqrt{\frac{2g}{\Omega_g^2 \mu_{ps}}} \quad (2.16)$$

This implies that pulses can be shortened if the modulation-depth  $\mu_{ps}$  is made large. Consider a pulse that propagates in the cavity. The shorter it becomes, the more spectral bandwidth it acquires and the wings of the spectrum see less gain than a CW background (due to e.g. spectral filtering or finite bandwidth of dispersive mirrors and radiation into dispersive wave). In order to keep the gain advantage for the short pulse, the gain-difference for the pulse needs to be increased which is accomplished by a growth of the modulation-depth.

### 2.3.4. Different dispersion regimes and power scaling

Solitonic mode-locking is generally possible in two regimes with either net positive or negative intra-cavity dispersion. To date the highest peak-power pulses are obtained from oscillators in the anomalous dispersion regime (ADR, negative GDD) where the pulses are *sech*<sup>2</sup> solutions to the Master equation and are largely unchirped. The onset of instabilities limits the obtainable peak power with these solitons to a characteristic threshold power. It was shown both theoretically and experimentally that the normal dispersion regime (NDR, positive GDD) can offer a more universal approach to avoiding these instabilities [76]. The NDR allows the existence of chirped solitons<sup>4</sup> with a favorable scaling of the pulse-energy with net positive intra-cavity dispersion  $W_{NDR} \propto |D_2|^2$  instead of  $W_{ADR} \propto |D_2|$  [66]. The GDD required to reach a certain pulse energy in the NDR is about an order of magnitude smaller than that required in the ADR. Analogous to chirped pulse amplification the main effect exploited in chirped pulse oscillators is the avoidance of high peak-powers that destabilize the pulse due to nonlinearities. With growing energy of the circulating soliton its chirp grows and can become very large with stretching-factors on the order of  $\sim 100$  [48]. In the NDR the pulse energy from a KLM Ti:Sa oscillator could be increased to half a  $\mu\text{J}$  and more than 10 MW peak power after compression [48, 79, 76]. The intra-cavity peak-power was reduced to approximately 5 % compared to the ADR with the pulse chirped to 1.5 ps FWHM duration. Similar results had been reported previously [80]. Tight focusing with such an oscillator already allowed the ionization of helium [49].

The NDR was realized as well in SESAM mode-locked oscillators with Yb doped gain materials [81, 41]. An attempt at direct comparison between the ADR and NDR is given in [41]. Up to 730 nJ, 490 fs pulses are generated in a SESAM-mode-locked Yb:KLu(WO<sub>4</sub>)<sub>2</sub> thin-disk oscillator in the ADR. In the NDR the performance was reduced with 270 nJ energy and 440 fs pulse-width (after compression) as well as

<sup>4</sup>Normal dispersion is primarily used in mode-locked fiber oscillators to scale the energy-output but was first investigated in Ti:Sa oscillators [77]. Ilday et al. in 2004 showed for the first time an all normally dispersive Self-Similariton mode-locked fiber oscillator generating 10 nJ pulses [78].

strongly increased noise. The authors attribute the much reduced performance using chirped pulses to (i) increased losses due to a new SESAM with higher modulation-depth and lower saturation-fluence as well as (ii) to the use of material windows to provide the necessary positive GDD. The increased SAM of the SESAM was necessary to keep the oscillator in stable single-pulse operation in the chirped NDR. In a later experiment the same research-group managed to extract 7  $\mu\text{J}$  pulses from a 1 MHz, cavity-dumped Yb:KYW bulk-oscillator at 67 % dumping-depth in the NDR [38]. The pulses were estimated to have a peak-power of  $>12$  MW after partial compression to 416 fs. The energy-scaling in this case was not a feature of the NDR but was made possible by the large fraction of energy dumped in combination with the low repetition frequency. As the authors stated the main motivation to rely on the NDR was to avoid the need for anomalous dispersion compensation with large values of net negative GDD. More recently, record GDD values on the order of  $-100,000$  fs<sup>2</sup> per round-trip have become feasible using highly dispersive mirror technology [82, 83], as was shown e.g. in [19, 28].

Initial experiments with an Yb:YAG KLM thin disk oscillator in the NDR were also unable to show superior performance to the unchirped ADR [84]. The main difficulty lay in the inability to starting the pulse-buildup, probably due to insufficient saturation of the SAM from the much lower intensity of the chirped pulses. When the slope of the SAM with respect to power is flat an initial power-fluctuation does not see a distinct gain-advantage over the remaining continuum and is less likely to grow into a steady soliton before it is dispersed. Opposed to the SAM in KLM oscillators that depends on the instantaneous intensity, SESAM saturate with fluence. Therefore long pulses with relatively low peak power yet reasonable energy content can easily saturate the absorber. This can be an advantage during pulse buildup, in particular for operation with long pulses in the NDR. However, as reported in [41, 38], the modulation depth of the used SESAM had to be relatively high in order to keep the pulses stable. This poses a problem for high power operation since the non-saturable losses in the SESAM grow along with the modulation-depth [85, 86, 39]. Congruent with [38] the larger positive GDD values in the KLM case also reduced the obtainable bandwidth.

Overly optimistic numerical predictions, favoring the NDR for reaching the 'fundamental limits' for mode-locked lasers were published recently in [87]. In these estimations, however, the pulse buildup dynamics are entirely neglected. Taking into account the experimentally observed starting difficulties in the NDR and the advantage of unchirped output pulses in the ADR, the experiments for this work concentrated on power scaling in the latter. Notwithstanding these experiments were restricted to the ADR they deal with increasing the peak-power threshold beyond which the solitons destabilize. This addresses an issue fundamental to both dispersion regimes and should help improving the KLM performance also in the NDR, provided high-power, chirped-pulse oscillator performance catches up with that in the unchirped soliton-regime.

## 3. Power scaling of Kerr-lens mode-locked thin disk oscillators

### 3.1. Yb:YAG thin disk

Not surprisingly, thermal effects have maybe the strongest impact on the performance of laser oscillators and have historically been the main limiting factor in power scaling solid state lasers. The contribution to a thermal lens stems from both the thermal dependence of the refractive index as well as mechanical deformation of the heated material [88, 89, 90]. Apart from thermal lensing, thermal stress induced birefringence can lead to depolarization of the light field and thus higher losses or destabilization of the laser.

In 1994 Giesen et al. [91] introduced the thin disk geometry for efficient cooling of the gain medium. The concept relies on maximizing the surface to volume ratio of the laser active medium by having it shaped as a thin disk of typically 100 - 200  $\mu\text{m}$  thickness and several mm in diameter. One side is reflection coated and contacted to a heat sink while the other is anti-reflection coated as depicted in figure 3.1. The thin disk is intended for pumping on a large area for which inexpensive, high power laser diodes are predestined. Power scaling is realized by simultaneously increasing pump and laser mode area in the thin disk, which acts as an active mirror.

The nearly one dimensional heat-flow in the medium in direction of the heat sink suppresses the transverse temperature dependence of the refractive index and thus thermal lensing. The remaining thermal lens is largely due to mechanical deformation and bulging of the thin disk material, which requires strong contacting to a stiff heat-sink [93]. In order to absorb a large portion of the pump light in the thin disk the pump beam is recycled by reflecting it many times back onto the disk via a pump arrangement. Several tens of pump passes can thus be realized with high pump absorption.

Due to the high mechanical stress during high-power pumping and also during the manufacturing process, not every host material is suitable for the thin disk geometry. While originally proposed, Yb:YAG has proven itself in high-power operation, with average laser power as high as 1.4 kW in pulsed operation and with diffraction limited beam quality from a single disk [15]. The highest power extracted from a single Yb-doped thin disk in near single mode operation is 4 kW [94].

A most important parameter that influences the heat production in the laser crystal is the quantum defect. It is the fractional difference of energy  $1 - \lambda_{pump}/\lambda_{lase}$  between the absorbed pump photons and the emitted laser photons. For Yb<sup>3+</sup> doped materials this quantum defect is particularly low which makes them suitable for high power lasers. In Yb:YAG the quantum defect is  $\sim 9\%$  when pumping in the wide

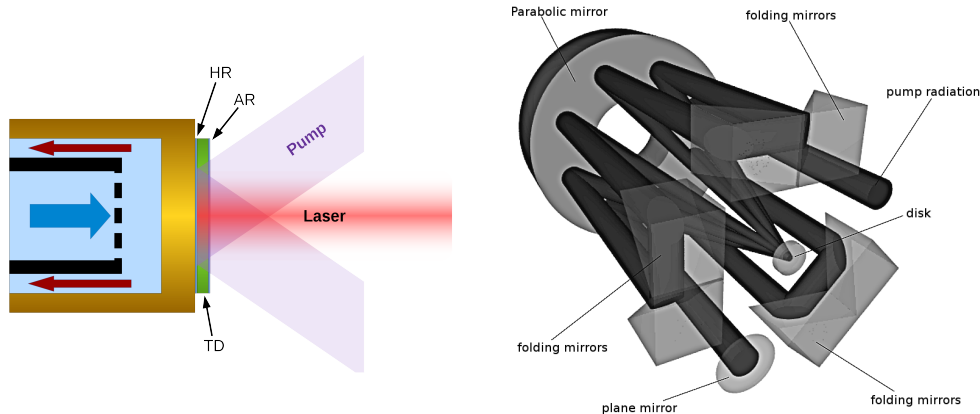


**Figure 3.1.** – (left) Thin disk concept (not to scale). HR: highly reflective coating, AR: anti-reflection coating, TD: thin disk. The heat sink is water cooled from the backside. (right) Pumping-scheme. The pump-light is folded back and imaged several times onto the thin-disk to maximize the absorption. Adapted from [92].

absorption band at 940 nm while, for example, the very common high power gain material Nd:YAG has a quantum defect of  $\sim 24\%$ . Pumping the narrow zero phonon line of Yb:YAG at 969 nm the quantum defect is even lower with only  $\sim 6\%$ . Not only the heat generation influences the thermal performance of the laser but also the ability to transport and dissipate it. Materials with high heat-conductivity both in the laser host as well as the heat-sink are therefore desirable.

Owing to the simple energy level structure of  $\text{Yb}^{3+}$ , Yb:YAG does not suffer from up-conversion or cross-relaxation losses. However, some not entirely understood quenching mechanisms reduce the upper state lifetime of  $\sim 1$  ms and limit the maximum doping concentration near 10 % at. [96, 93]. This, in turn, limits the minimal thickness of Yb:YAG thin-disks, the reduction of which would be beneficial for heat extraction.

In terms of ultrashort pulse generation the thin-disk geometry is ideal since power scaling demands large mode areas in a thin gain medium which reduces nonlinear phase accumulation for intense, short pulses. This greatly helps reduce the demand on pre-chirping in regenerative amplifiers and gives more fine control over nonlinear phase balancing in soliton mode-locked oscillators. The broadened emission line of Yb:YAG at 1030 nm has an approximate bandwidth of 8 nm which would allow to generate pulses with durations as low as 140 fs. This value, however, is usually not reached due to the large output-coupler losses for high-power extraction and the accompanying gain-narrowing.

## 3.2. Resonator design

Generally the design features of a high-power KLM thin disk oscillator do not differ much from its CW counterpart. The dominant optimization precept is the avoidance of thermal lenses. Because of their low thickness a TD oscillator compels

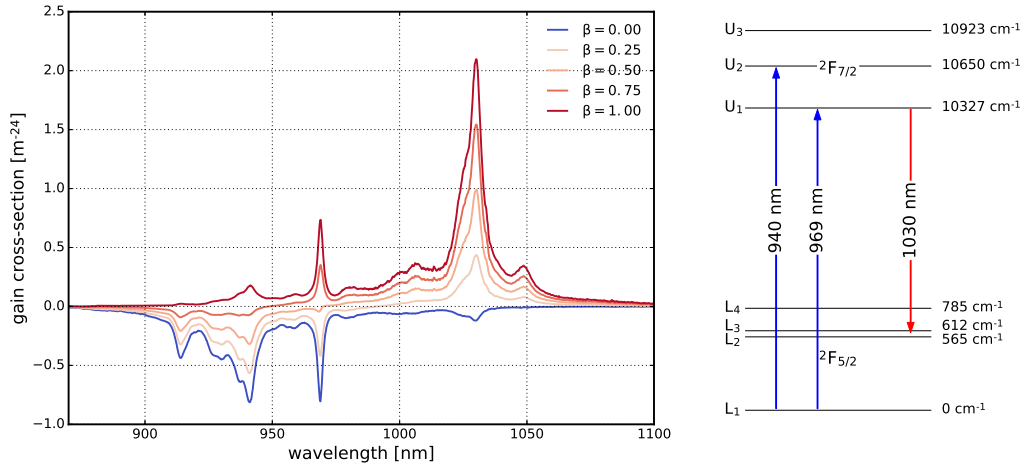


**Figure 3.2.** – (left) Gain cross-section of Yb:YAG for different inversion levels. Data from [95]. (right) Energy levels of  $\text{Yb}^{3+}$  in YAG. Data from [93].

the separation of gain and Kerr-medium unlike the most compact setup of most modern, soft aperture, low power KLM oscillators. One can therefore split the cavity design into separate parts. One part that deals with the gain from the TD and the essential, static mode-shaping optics and at least one other part that includes fashioning the main nonlinear elements to provide the dynamic mode-shaping for SAM.

### 3.2.1. Static resonator section

A linear resonator consists of at least 2 mirrors that are arranged such that a light beam bouncing in between is perfectly reflected back onto itself. In continuous wave (CW) operation resonant longitudinal modes can form a standing wave pattern in the oscillator and give rise to effects like spatial hole burning<sup>1</sup>.

KLM resonators can be realized either with a linear or with a ring resonator. Ring resonators for mode-locking in general require more thought than do linear resonators which intrinsically can support only unidirectional pulse-propagation and do not require additional elements to enforce this prerequisite for stable mode-locking. Additionally, the amount of optical elements and space to produce the same interaction volume between resonator mode and gain in ring resonators is approximately twice that of the linear setup. The same is true for the number of dispersive elements (mirrors in the most case). However, ring lasers tend to be more robust against spurious back reflections due to a lack of resonant coupling between forward and backward traveling pulses [98, 99]. A thin-disk KLM ring oscillator has been realized already with the goal of unidirectional intra-cavity HHG [29].

<sup>1</sup>An effect unwanted in narrow line-width, CW lasers but supposedly beneficial for short pulse generation under certain conditions [97]

### Resonator stability

If the resonator is stable<sup>2</sup> a transversal cavity-mode can be found. Restricting cavity analysis to paraxial fundamental Gaussian mode solutions is usually sufficient in order to characterize stable cavities without taking into account diffraction at apertures or mode-altering elements such as a gain profile or non-parabolic self-focusing. The calculus of ray-transfer (ABCD) matrices is the most efficient way to quickly analyze TEM<sub>00</sub> modes of paraxial stable resonators. The method is briefly explained in the appendix A.1.

Varying either a distance between some resonator elements or the refractive strength of an element results in a certain number of regions in which an oscillator is stable, also called stability zones. The number of distinct zones depends on how many times the cavity-mode revisits or passes said distance or element during one round trip through the resonator<sup>3</sup>. Outside these stable regions no fundamental Gaussian mode can exist and the transversal mode-sizes either diverge or converge at the cavity elements. In laser operation this manifests itself as increasing diffraction losses on approaching the stability limits.

The overall mode area scales linearly with the resonator length [100]. This has an important implication for power scaling as large mode-sizes can only be achieved with relatively long oscillators, naturally limiting the repetition-rate of the oscillator. One can introduce intra-cavity telescopes to expand the mode in one arm [101, 31], however, the mode size in the opposing arm will shrink, possibly limiting peak powers or fluences due to mirror damage thresholds.

### Thermal lenses

It can be shown that the mode size in an element exhibiting a variable (thermal) lens limits the range over which the lens's refractive power can be varied before the resonator becomes unstable [102].

$$w_0^2 = \frac{2\lambda}{\pi} \frac{1}{\Delta p} \quad (3.1)$$

Here  $w_0$  is the mode radius at the position of the variable lens at the condition of dynamic stability. The condition of dynamic stability is the minimal beam size change with the thermal lens and can be expressed as  $\frac{dw}{dp} = 0$ .  $\Delta p$  is the range of refractive power over which the resonator containing this lens is stable. The dynamically stable point lies typically near the center of the stability-zone. This finding, equation (3.1), shows a strong limitation of power scaling with beam area and emphasizes again the importance of thermal management, especially for the gain medium. Several methods to compensate these effects in the resonator have been thought of, however, the thin disk approach, mostly avoiding the appearance

---

<sup>2</sup>Unstable resonators are not suitable for femtosecond solitonic mode-locking.

<sup>3</sup>From a mathematical view this is a consequence of the fundamental theorem of algebra when solving for the roots of the polynomial produced e.g. by multiplication in the ray transfer matrix formalism.

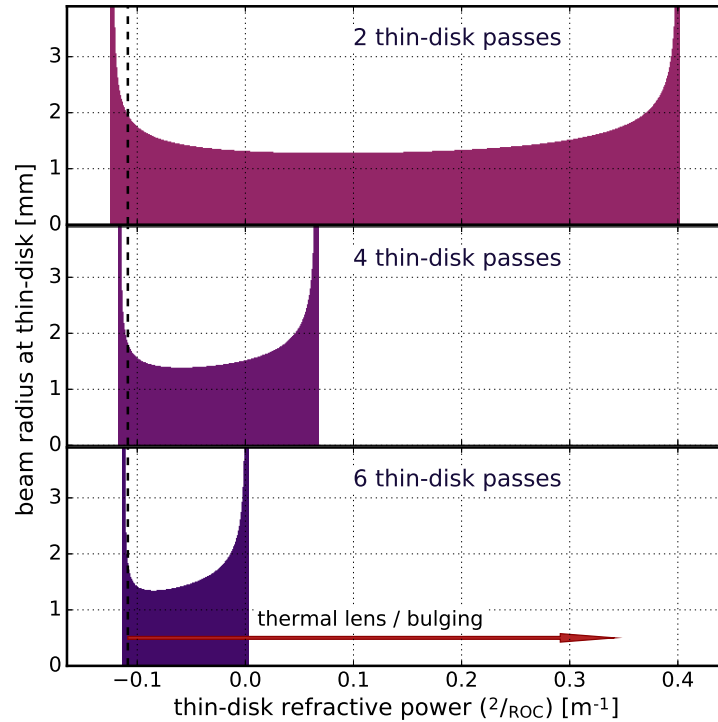


**Figure 3.3.** – Shrinking of the stability zone width dependent on varying number of passes through the thermal lensing element.

of thermal lensing and stress induced depolarization has proven the most successful approach.

Owing to its low thickness the gain provided by the thin-disk is relatively low. In order to compensate for this shortcoming and to allow high output coupling ratios the laser mode can be made to travel several times per round trip through the thin-disk. In order to keep the mode-sizes constant for all passes and not change the cavity an imaging system was realized in [19], allowing the cavity mode to pass 44 times through a thin disk in one round-trip. This enabled an output coupling transmission of more than 70 %. Although such an approach to power scaling seems a most elegant solution it has a not insignificant drawback. The difficulties arise from a cumulative narrowing of the cavity's stable zone with increasing number of passes on the thin-disk that is caused by the thermal lens. The situation is illustrated in figure 3.3. Section 3.2.2 will shed light on why this makes implementation in KLM oscillators more challenging than e.g. in SESAM oscillators which can operate near the point of dynamic resonator stability, i.e. close to the center of the stable zones depicted in figure 3.3.

### Gain-mode-matching

Different transverse cavity modes of order  $m, n$  exhibit differing mode frequencies [100].

$$\nu_{mn,q} = \frac{c}{2L} \left( q + \frac{m+n+1}{2\pi} \zeta_{Gouy} \right) \quad (3.2)$$

where  $c$  is the speed of light,  $L$  is the cavity length,  $\zeta_{Gouy}$  is the round-trip Gouy phase-shift and  $q$  the longitudinal mode order. Unless the resonator is degenerate exactly at the stability border ( $\zeta_{Gouy}$  is integer multiple of  $\pi$ ) the higher order modes contribute additional frequencies that are offset from the fundamental resonances. These additional frequencies can not be mode-locked simultaneously and can destabilize mode-locking by introducing noise at the beating frequency and limit the overall oscillator performance [62, 103]. Therefore it is desirable to only have one single transverse mode oscillating in the resonator. The fundamental Gaussian resonator mode generally has the smallest transversal extent and an optimum matching to the soft aperture of the pumped region on the disk can serve as a filter for higher order modes. A simple estimation shows the next higher order mode to have a factor  $\sqrt{2}$  larger beam-radius than the TEM<sub>00</sub> [100]. This serves as criterion to set the  $1/e^2$  beam diameter of the fundamental mode to approximately 70 % of the disk's pump-spot and enable both suppression of higher order modes as well as fair pump-power use. However, the mode-pump overlap is worse than in multi-mode operation and generally the efficiency will not be as high. The achieved mode-locked efficiencies with Yb:YAG in this work stayed below 40 % whereas Yb:YAG multi-mode CW oscillators can typically reach more than 50 % optical to optical efficiency [94].

Another way to filter out higher order modes is by inserting a mode-filter which can simply consist of a plate with a properly sized hole. A KLM resonator at the stability edge (see section 3.2.2) is likely to show signs of strong astigmatism with the laser beam being several times larger in one transverse direction than in the perpendicular one (see, e.g. [21]). By inserting a hard aperture as filter the mode can be forced to nearly Gaussian shape (see e.g. figure 3.14). Interestingly with such an aperture the net diffraction losses in CW could be reduced with respect to the unfiltered resonator mode, resulting in higher CW output power.

### 3.2.2. Nonlinear resonator section

In order to provide the high intensities required to induce a noticeable lens in the Kerr-medium it is usually placed in the focus of a telescope or focusing section. This is implemented as an added section to the previously described, static resonator section and consists of two additional concave mirrors<sup>4</sup>. These are thought to be arranged in an Newtonian imaging fashion which we shall call *q-preserving* since it does not alter the complex Gaussian beam parameter  $q$ <sup>5</sup>. This is realized by placing the mirrors as indicated in figure 3.4. The *q-preserving* condition is fulfilled if  $d = f_1 + f_2$  and the only effect of adding the mirrors to the cavity would be extending it's length but not change the mode-sizes if  $f_1 = f_2$ .

<sup>4</sup>Lenses can also work, however, both chromatic aberrations or absorption in the lens material might dissuade from use in broadband or high-power oscillators

<sup>5</sup>Except for mirroring the image beam

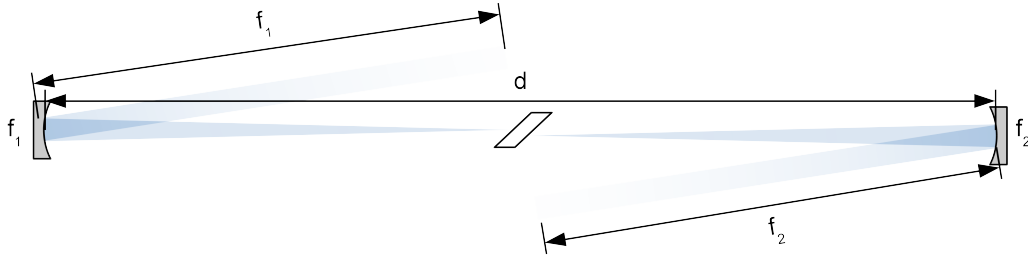


**Figure 3.4.** – Focusing section with Kerr-medium.  $f_{1,2}$  are the effective focal lengths of the concave mirrors. For the imaging condition  $d = f_1 + f_2$

It was quickly realised that KLM resonators work best near the edges of stability where the resonator mode becomes increasingly sensitive to changes of intra-cavity lenses and facilitates KLM start-up and the shortest achievable pulses [104, 105, 106]. A measure for KLM sensitivity at a certain plane in the resonator can be defined as

$$s = \frac{1}{w(P=0)} \left. \frac{dw}{dP} \right|_{P=0} \quad (3.3)$$

where the sensitivity  $s$  is the initial slope of the mode-radius  $w$  with intra-cavity power  $P$  normalized to the zero power mode-size. It is obvious that hard aperture mode-locking requires a negative value of  $s$  to have a beneficial effect on the SAM. The sign and magnitude of  $s$  depend on the longitudinal position within the cavity.

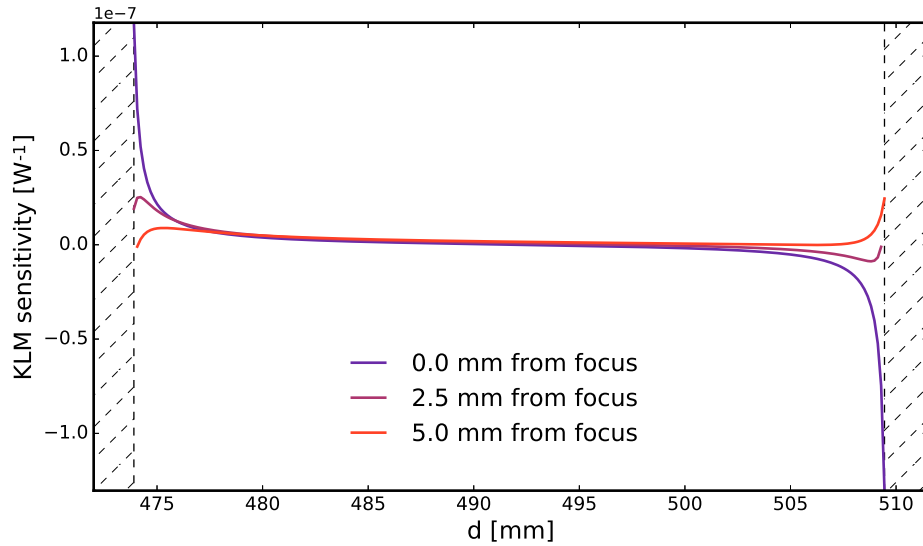


**Figure 3.5.** – Simulation of KLM sensitivity  $s$  as function of mirror-separation  $d$  for several distances  $a$  of the Kerr-medium from the focus. The cavity is unstable in the hatched region.

**KLM resonator with apertures** The most intuitive approach to viewing the action of self amplitude modulation is with a hard aperture, a solid wall with a cutout

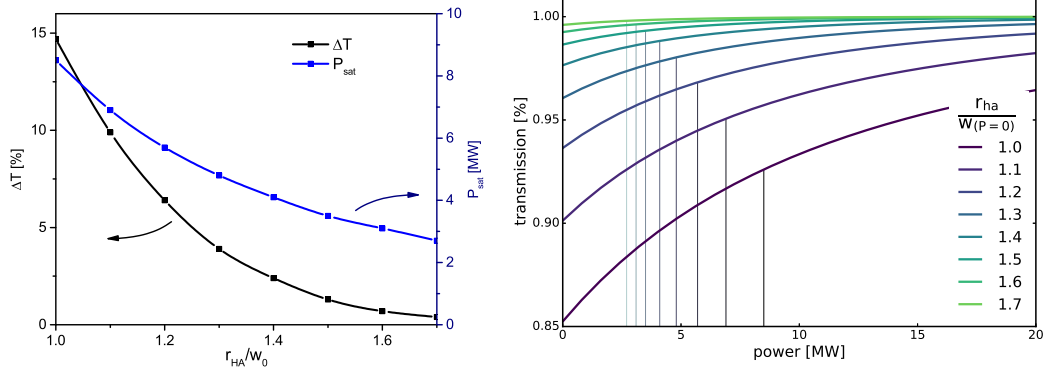


**Figure 3.6.** – Simulation results for ray-transfer matrix-calculation of a resonator including a single hard-aperture with hole-radius  $r_{ha}$  normalized to the beam-radius for zero peak-power (CW): (left) Saturation power  $P_{sat}$  and difference in hard-aperture transmission  $\Delta T$  for different hard-aperture sizes. (right) Transmission of the fundamental cavity mode for varying intra-cavity power and hard aperture sizes. The values of  $P_{sat}$  are indicated by vertical lines

in the center that transmits only a fraction of the total power in the laser beam. One can model the single-pass transmission with the Gaussian beam ray-transfer matrix formalism A.1, however the results will be quantitatively very inaccurate if applied to a resonator. The reason is that this formalism can not take into account diffraction at an aperture which would in turn alter the shape of the mode. It is possible to account for diffraction at apertures in numerical mode-calculations (see section §A.2), however, the operations required can be computationally quite costly and are not necessarily useful for optimization of the KLM cavity. Nonetheless the ray-transfer-matrix approach still is useful to obtaining a qualitative impression of the SAM action in a particular resonator.

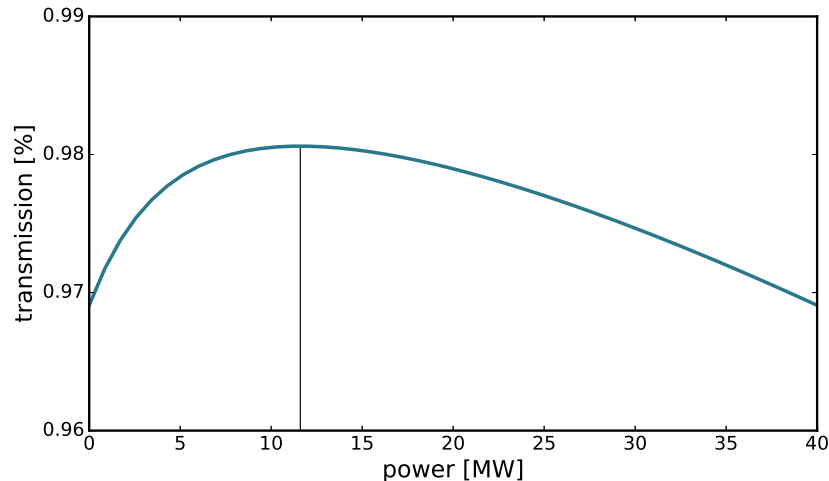
**Self-amplitude modulation saturation with a hard aperture** Figure 3.6 shows some estimated SAM parameters as well as power transmission derived from ray-transfer-matrix simulations. The size of a hard aperture with radius  $r_{HA}$  has a clear influence on the important saturation power  $P_{sat}$  and naturally the difference in cavity transmission  $\Delta T$  that strongly influence the maximal peak power and minimal pulse duration achievable when mode-locked (see section 2.3.3). While smaller apertures increase the modulation depth and also push the saturation power the aperture size obviously can not be decreased arbitrarily since the nonsaturable losses for the CW mode as well as for the pulses increase dramatically as seen in the transmission curves on figure 3.6 (right). The hard aperture radius  $r_{HA}$  is normalized to the CW mode radius  $w_0$ .

Table 3.1 from one of the early mode-locking experiments demonstrates the influence of smaller apertures on the pulse duration.

**Saturation of the self-amplitude modulation with soft and hard apertures** The transmission curves and parameters displayed in figure 3.6 only show the hypothetical

aperture diameter [mm]	2.5	2.7	3.0
$\Delta\tau_{fwhm}$ [fs]	330	340	360

**Table 3.1.** – Experimental data for the pulse-duration dependence on the hard aperture size.



**Figure 3.7.** – Ray-transfer matrix simulation of an arbitrary power-dependent resonator-mode via a Kerr-lens. The Gaussian-beam transmission through two hard apertures (one at the thin-disk, one at the end-mirror) is plotted and a value for the saturation-power  $P_{max}$  is indicated by the vertical line.

case of a single hard aperture in the resonator. One generally has to also care for at least one more soft aperture that originates from the gain profile and has a non-uniform shape with finite extent. In typical KLM lasers the gain is provided by high beam-quality pump sources and the gain-profile is Gaussian over the length of the crystal. The overlap between mode and saturated gain then defines the SAM and in the KLM lasers considered so far<sup>6</sup> lead to various optimized designs [107, 108, 109, 110]. Thin disk lasers are usually pumped with low beam-quality sources and the pump profile resembles rather a top-hat or super-Gauss profile. A (very crude) approximation for SAM then models the gain profile as another hard aperture. Again, quantitative estimations are hardly realistic, especially since now the effective soft aperture additionally depends on the oscillator dynamics which in turn modifies the mode-profile and cavity transmission. The shape of the gain-profile can be altered quite strongly by saturation effects (see e.g. figure 3.14 a,b) or [69]).

Modeling a thin-disk KLM cavity with the ray-transfer-matrix approach and with hard apertures at the end-mirror and thin-disk while neglecting diffraction leads to a roll-off of the SAM near a power  $P_{max}$ . This can be seen in figure 3.7.

In this section some important guidelines for high-power thin-disk resonators are given. In particular a possibly limiting factor of the thermal lens to KLM multi-pass

<sup>6</sup>gain crystal = Kerr-medium

cavities for high output-coupling ratios is considered. So far, soft-aperture KLM in combination with a weak SESAM (modulation-depth  $<0.1\%$ , [21]) or without (authors experiments) was realized with a thin-disk. However, experience showed that the combination with a hard aperture and no SESAM allowed the generation of shorter pulses as well as more reliability in the KLM starting process. Ray-transfer matrix calculations are used to illustrate the dynamic behavior of the power-dependent cavity-losses. Taking into account multiple hard aperture transmission motivates the fast, cubic-quintic saturable absorber model (see section 2.3.2) notwithstanding the limited quantitative significance of the simulations.

### 3.3. Power-scaling experiments

In the following section the experimental results achieved with two different oscillator base frames are presented and discussed. The subsections are chosen to include the most influential 'knobs' on laser performance and power scaling. The main results have been published in [28] and [32].

#### 3.3.1. Geometrical power-scaling scheme

The initial concept behind the geometrical power scaling scheme was based on a quite naive understanding of oscillator dynamics that, nevertheless, led to some intriguing experimental results. Consider a working KLM oscillator in steady state with a certain set of parameters including GDD, SPM, SAM, gain, linear loss as well as pulse duration. The assumption was, that this set of parameters stays fixed, except for the SPM-coefficient  $\gamma_{spm}$ . Increasing the mode size  $w_{kerr}$  in the Kerr-medium by a factor  $N$  (figure 3.8) would result in a shrinking of  $\gamma_{spm}$  by the factor  $N^2$  since  $\gamma_{spm} \propto 1/w_{kerr}^2$ . In order to keep the pulses stable, the nonlinear phase-shift  $\phi_{nl} \approx \gamma_{spm} \cdot P_{pk}$  would require to stay fixed. Since all other parameters should remain as before the peak power needs to grow by  $N^2$ . The first expectation was therefore a quadratic scaling of the peak-power with the mode-diameter or the ROC of the focusing section respectively. Apart from gain-saturation this consideration completely neglected the experimentally elusive, yet highly important influence of the focusing section on the SAM.

Figure 3.9 shows the simulated growth of  $P_{max}$  in the experimentally used resonators. The SAM parameters are simulated by single-pass transmission through several hard apertures. The apertures were positioned near the end-mirror and at the thin-disk. Since the influence of aperture-diffraction is completely neglected this is a very poor quantitative model, however, the simulation should be able to catch the qualitative trend of the SAM parameter  $P_{max}$ . For the tried out ROC in experiment (0.5 to 2.0 m) an approximately linear growth of  $P_{max}$  with the mode-size seems not too far fetched. This behaviour most likely explains the linear rise in peak-power that was observed experimentally (see section 3.3.3) instead of the expected quadratic growth.

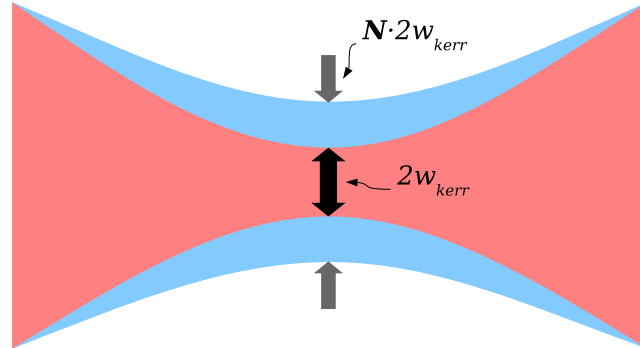


**Figure 3.8.** – Geometrical power-scaling. The mode-diameter,  $2w_{kerr}$  is increased by a factor  $N$ , decreasing the SPM coefficient  $\gamma_{spm}$  by  $N^{-2}$ .

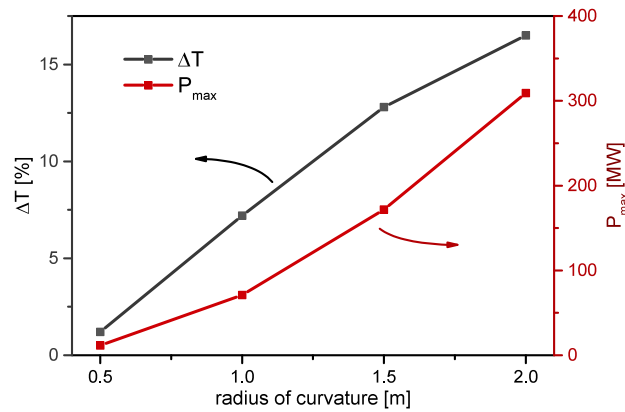


**Figure 3.9.** – Simulated single-pass transmission through a cavity used in experiment with apertures at the thin-disk (diameter 3.6 m) as well as at the output-coupler (diameter 5.5 mm). The SAM-parameter  $P_{max}$  (red, right y-axis, see section 2.3.2) is deduced from the power-transmission-curve which was calculated for different radii-of-curvature of the focusing-mirrors in the nonlinear resonator-section (x-axis). The fundamental cavity mode through the 3 apertures was calculated with the ray-transfer matrix formalism.  $\Delta T$  (left y-axis) is the difference in transmission between zero power and  $P_{max}$ . The reason for the steady rise in  $\Delta T$  is that the zero-power mode-size at the apertures (of fixed size at the thin-disk) increased slightly along with the radius of curvature, therefore decreasing the single-pass transmission for the low-power mode.

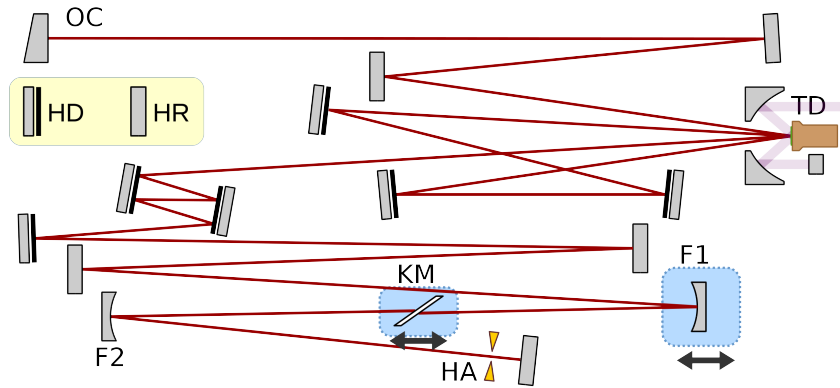


**Figure 3.10.** – Oscillator sketch with ROC up to 900 mm. OC: output-coupler, HD: highly-dispersive mirror, HR: highly reflective mirror, HA: hard aperture, KM: Kerr-medium, TD: thin-disk, F1,F2: spherical focusing mirrors.

### 3.3.2. Oscillator setup

#### Static gain section

To explore this train of thought experimentally, a Kerr-lens mode-locked thin-disk oscillator was set up with a linear resonator. Mimicking the previously tested resonator described in [21] was not possible for the desired output powers  $>100$  W since the required mode- and pump-spot-size was larger. Additionally the utilized thin-disk from TRUMPF Laser GmbH had a nearly flat curvature in contrast to the previously utilized module from Dausinger + Giesen GmbH with a curvature of 6 m. The resonator was designed following the guidelines laid out in sections 3.2.1 and 3.2.2. Its layout is sketched in figure 3.10. The nearly flat, 0.1 mm thick thin-disk with a radius of curvature (ROC) of  $\sim 20$  m was revisited 4 times during one round-trip. This implies 8-fold passing of the pulse through the Yb:YAG disk, which allowed the use of an output-coupler with an optimum of 21 % transmission (see section 3.3.5).

The disk was pumped in the zero-phonon-line at 969 nm with up to 800 W pump-power from volume-Bragg-grating (VBG), wavelength-stabilized CW laser diodes<sup>7</sup>. A multi-mode fiber was used for convenient delivery of the pump radiation to the imaging optics. A pump spot radius of 3.3 mm allowed a maximum single-pass pump intensity of  $\sim 9$  kW/cm<sup>2</sup> with nearly flat-top pump-profile. An advantageous side-effect of the large pump-area is the easy alignment and determination of transverse mode shape by observing the intensity pattern of the emitted green light caused by cooperative luminescence in Yb:YAG [111]. For a sufficiently close distance between

<sup>7</sup>Unfortunately these VBG diodes gave up the ghost fairly quickly due to back-reflections from the pump-optics. The VBG feeds a not insignificant part of the diode-laser output back to the diodes. According to the manufacturer, the additional, unabsorbed pump-power that was fed back into the diode-module exceeded the threshold for safe diode operation, resulting in a significantly reduced lifetime. By today the reliability of VBG stabilized diodes has been improved as the manufacturer assures, however, all further oscillator experiments were conducted with non-stabilized yet proven (plus significantly cheaper) laser-diodes emitting at 940 nm.

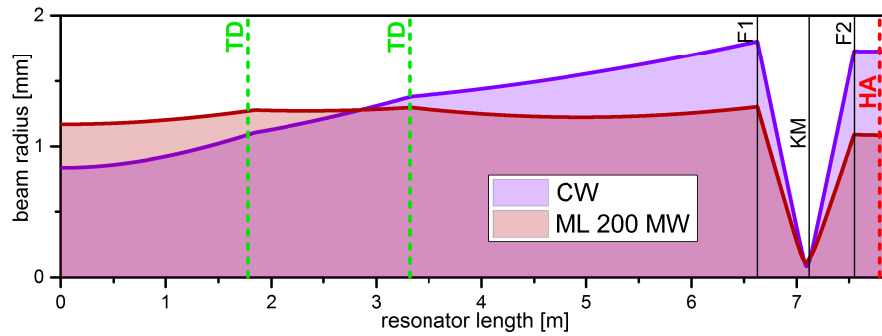


**Figure 3.11.** – Simulated CW and mode-locked mode size distributions inside the resonator.

two consecutive passes of the oscillator mode through the pumped disk the mode-size in the disk does not change drastically. For a larger number of passes, however, an imaging configuration is required.

### Nonlinear section and Kerr-medium

A nonlinear resonator section was inserted close to the end-mirror of the linear cavity. The stability-edge was approached by shifting the position of curved mirror F1 (figure 3.10) via manipulation of a micrometer-screw on a translation-stage as indicated. The Kerr-medium consisted of a 1 mm thick sapphire plate (see also section 3.5.3). Selection of the polarization direction was ensured by placing the KM under Brewster's angle, resulting in linear, p-polarized laser output. A further translation stage allowed shifting the Kerr-medium along the propagation axis.

### Aperture

A critical part of the resonator design is the choice of the aperture positions and sizes. A hard aperture (HA) was positioned near the end mirror as indicated in figure 3.10. Figure 3.11 shows the simulated change of the intracavity mode sizes from CW (zero power) to ML operation (200 MW). One can easily identify an ideal position for the hard aperture near the end-mirror, where the beam radius shrinks the most with increasing power. The aperture had to be water-cooled and was thus made from copper. Different hole-sizes, ranging from 4 to 5.5 mm diameter were used. An X-Y manipulation stage allowed adjustment of the transverse HA position.

### Dispersive mirrors

The intracavity GDD was provided by highly dispersive (HD), dielectric multilayer mirrors [82]. The used mirror design provided  $-3000 \text{ fs}^2$  GDD per mirror reflection with a nominal bandwidth of  $\sim 10 \text{ nm}$  and high reflectivity of  $>99.95 \%$  (see figure 3.12 for GDD design curve). With up to 6 HD mirrors the total GDD per round-trip could be varied from  $-48,000$  to  $-6000 \text{ fs}^2$  in steps of  $6000 \text{ fs}^2$  (figure 3.10). The positioning

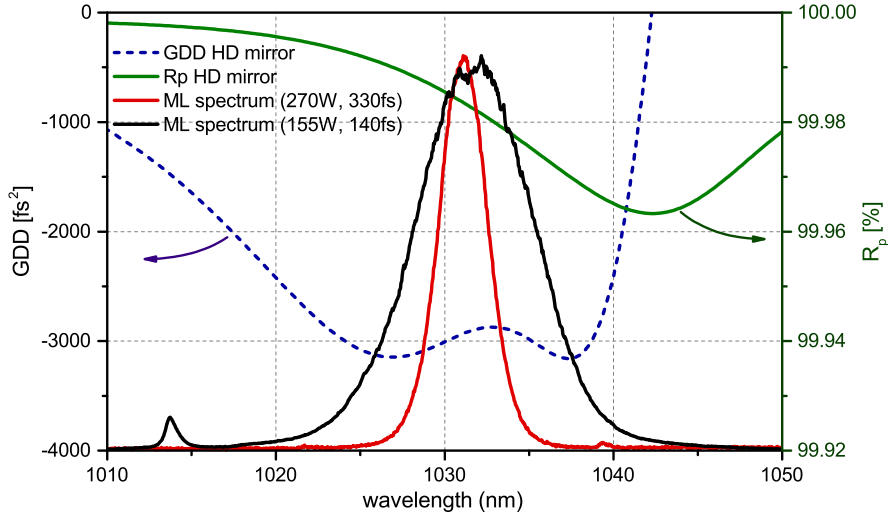


**Figure 3.12.** – GDD and reflectivity design curves of the utilized HD mirror coatings. The red and black lines shows the mode-locked output spectrum in the 900 mm and 2000mm ROC configurations as comparison in arbitrary units.

in the cavity was picked with the largest possible spot-size on the HD mirrors in mind. This was a necessity to suppress damage to the coatings during the startup phase of the oscillator. Until a reliable way to start mode-locking in these high power oscillators was found (see section 3.5.3) sporadic spiking of the oscillator tended to damage the cavity optics, especially the HD-coated mirrors or the Kerr-medium.

Due to their narrow bandwidth small coating errors could reduce the oscillator's bandwidth noticeably, making a selection process for the utilized mirrors necessary.

The HD mirror coating is a bit more complex than that of simple high reflectivity (HR) mirrors, typically employing quarter-wave-stack designs. The higher number of coating layers and locally enhanced electric field strength inside the HD layer-structures give rise to stronger absorption and thus heating of the mirror. The utilized design was fairly optimized for low light absorption, however, the high intra-cavity average power still leads to a considerable temperature gradient on the mirror surface which can cause thermal lensing effects and limit the output power [112]. Further reduction of the thermal gradient can be achieved by coating mirror substrates with high thermal conductivity. Figure 3.13 shows temperature profiles of mirrors with substrates made of fused silica, sapphire and silicon, all with the same HD-coating. The temperature rise is caused by 3.6 kW circulating intra-cavity average power in CW operation and recorded with an IR camera.

The Fused silica mirror shows a peak to valley difference of more than 10 °C while in both sapphire and silicon mirrors one is hard-pressed to discern the temperature rise of less than 0.5 °C. Notwithstanding these measurements show a clear advantage of using substrates with high thermal conductivity, all further experiments were carried out using Fused silica. Sapphire, being a very hard material, is difficult to polish and most substrates exhibit more surface defects than fused silica ones do. This leads to a lower damage-threshold of the coating which was noticeable

(a) Fused silica,  $\Delta T_m = 11.6^\circ\text{C}$ (b) Sapphire,  $\Delta T_m = 0.3^\circ\text{C}$ (c) Silicon,  $\Delta T_m = 0.5^\circ\text{C}$ 

**Figure 3.13.** – Thermal images of HD mirrors with different substrates. The dynamic range was adjusted for each image. The temperature difference  $\Delta T_m$  between temperature-peak and mirror-edge is written below each image.

during mode-locking initiation. While the coating on the silicon mirror did not exhibit a strong gradient, the non-reflected part of the laser radiation was absorbed in the substrate, quickly leading to elevated average substrate temperatures beyond 50 °C without active cooling. The highest intra-cavity average powers achieved in all experiments stayed below 1.4 kW and the improvements to the in-house HD coating design<sup>8</sup> allowed stable operation in KLM regime even with Fused silica substrates.

### Cw vs. ML

Before mode-locking the oscillator was aligned and warmed up in CW operation. The bad mode-pump overlap and diverging beam-sizes while close to the stability-edge (see figure 3.11) gave rise to high diffraction-loss and inefficient laser operation. Figures 3.14 display typical fluorescence intensity images of the pumped disk while running in CW and in ML regime. In order to initiate pulse formation mirror F1 was perturbed by pushing the translation stage and releasing again. The procedure is better described in section 3.5.3. Once mode-locked the mode-pump overlap improved and the intra-cavity power increased drastically. At lower output coupler transmission ( $\leq 15\%$ ) the difference could be as high as 300%. With output coupler transmissions  $>20\%$  and high pump intensity, thermal lensing did play a more dominant role and the difference between CW and ML output power diminished to no more than 60%. These large average power differences are indicative of strong SAM.

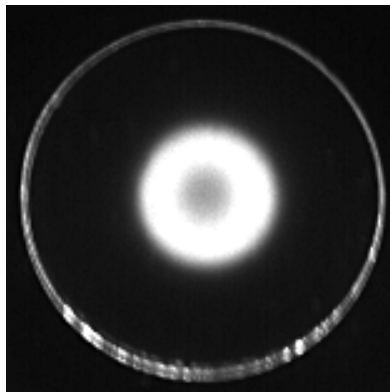
Near the stability edge the CW resonator mode becomes astigmatic since the optical axis necessarily impinges on an optical element under some angle. Stronger refractive power of the elements increase the astigmatism (see e.g. A.1). In figure 3.14 c) the mode astigmatism is barely discernible, due to the intra-cavity apertures strongly clipping and shaping the horizontal part of the mode. Removal of the hard aperture leads to beam profiles as depicted in [21]. Mode-locking shifts the resonator mode in the stability diagram, making it more stable and mitigates the effects of astigmatism.

### Instabilities

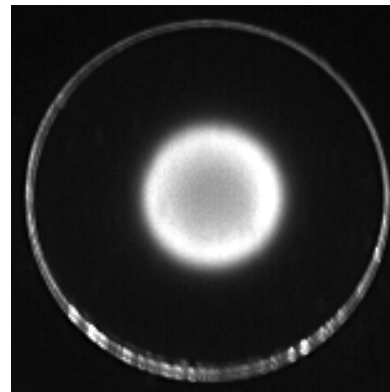
The fundamental soliton is only observed for a specific energy of the pulses which is adjusted via the gain. Pumping significantly above the mode-locking threshold in general results in instabilities. These could be observed in the shedding off of power to the CW continuum which was visible as CW background in the optical spectrum. The pump power could be reduced until the CW background in the spectrum vanished to yield background-free, single pulses. Above a certain pump power level the pulses started splitting up being noticeable in sudden jumps of the optical spectrum shape when increasing or decreasing the pump power. This way one can count the number of pulses circulating in the oscillator. The spectrum retained its near  $sech^2$  shape on multi-pulse transitions, however the bandwidth dropped with each additional pulse in the cavity. In case the inter-pulse separation was very

---

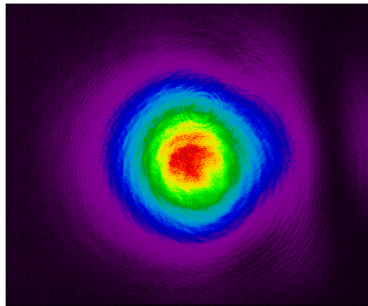
<sup>8</sup>The coatings were designed and fabricated by the LMU internal ultrafast coating group, led by Vladimir Pervak and proved superior to other, commercial mirrors under testing.



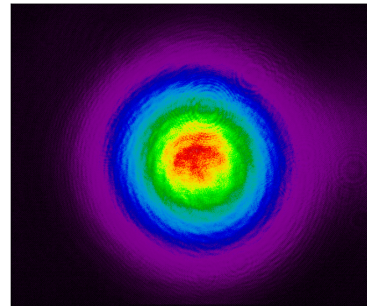
a) Disk: CW - 50 W



b) Disk: ML - 140 W



c) Beam-profile: CW - 50 W



d) Beam-profile: ML - 140 W

**Figure 3.14.** – a)-b): Fluorescence images of the pump-spot on the thin-disk. c)-d): Output beam-profiles.

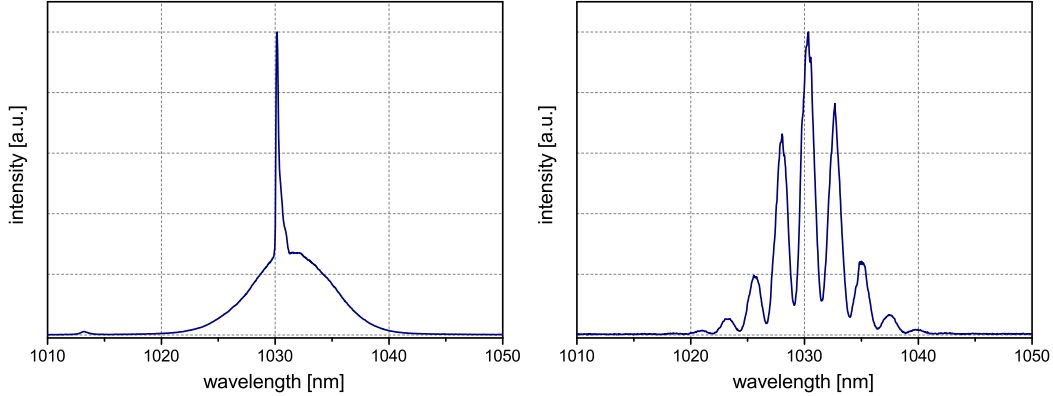


**Figure 3.15.** – Mode-locking instabilities. (left) Spectrum with typical CW breakthrough. (right) Modulated spectrum with two pulses closely spaced.

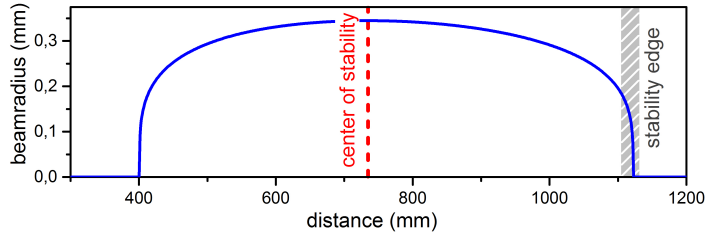


**Figure 3.16.** – Method to choose comparable focal spot size of the CW mode.

close, the spectrum became strongly modulated. See figure 3.15 for typical spectra indicative of these instabilities.

Counting the jumps in the spectrum or looking for modulation is, however, not sufficient to prove fundamental mode-locking. Therefore, to ascertain single pulse operation additional measurements with a fast photo-diode and oscilloscope and an autocorrelator are necessary.

### 3.3.3. ROC scaling

Additionally to providing a focus for driving KLM and tuning the resonator stability, the nonlinear resonator section allows a relatively independent scaling of the Kerr-medium mode-size. By picking curved mirrors F1, F2 (figure 3.10) with concave radii of curvature of 500, 600, 700, 800 and 900 mm the mode beam-radii in the focus were varied proportionally. Determination of the absolute focal spot-size inside the cavity is relatively tricky and quite error-prone and was therefore approximated from the focal spot sizes value of the designed CW mode. The maximum waist-size over the whole parameter range of the stable zone (figure 3.16) is then comparable with other cavity configurations since it does not explicitly depend on the mirror separation  $d$  (figure 3.4). The absolute mode-radius (x-axis in figures 3.18) is therefore not accurate but the scaling is.

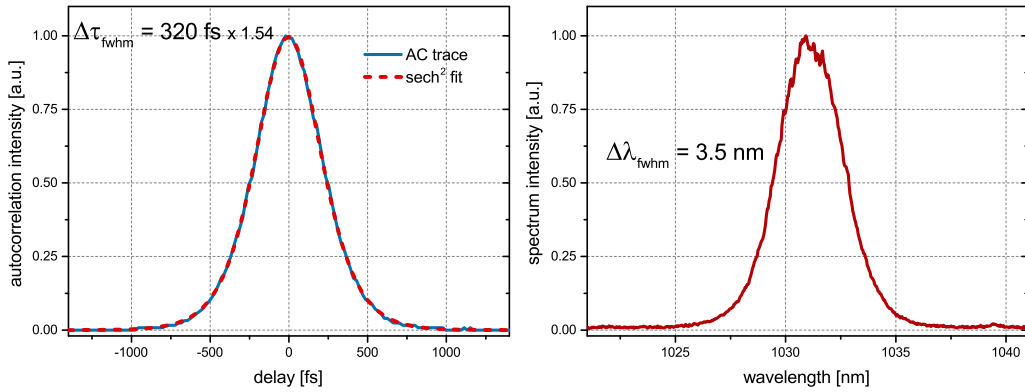


**Figure 3.17.** – Intensity autocorrelation trace with  $sech^2$  fit and spectrum of the output pulses with 40 MW peak power from the 900 mm ROC-oscillator.

The resulting measurements for the intracavity peak power and pulse duration are summarized in figure 3.18. In the investigated parameter range the peak power shows a clearly linear scaling with nearly constant pulse duration around 330 fs. The GDD was kept at a constant  $-48,000 \text{ fs}^2$  for all configurations and so was the output coupler transmission with 21 %. With 900 mm curvature a maximum of 270 W average output power was measured. The pulse duration was measured with an intensity autocorrelator to be 320 fs (figure 3.17). Together with 3.5 nm FWHM optical bandwidth the time-bandwidth product yields  $\sim 0.315$  confirming unchirped  $sech^2$  shaped pulses. At 18.8 MHz this corresponds to an intra- and extra-cavity peak power of more than 180 MW and about 40 MW respectively. The output pulse energy corresponds to above 14  $\mu\text{J}$ . The nonlinear phase-shift of  $0.46\pi$  was deduced from the soliton area theorem (equation (2.10)) that requires a SPM coefficient  $\gamma_{spm}=0.0077 \text{ MW}^{-1}$ . Estimation of the factor  $\gamma_{spm}$  from mode-calculations for given intra-cavity peak-power yields  $0.0071 \text{ MW}^{-1}$ .

It is interesting to note that these power levels could be reached with the oscillator operating in normal air atmosphere. Similar peak power in SESAM mode-locked oscillators required evacuation of the oscillator housing or flooding with Helium to reduce the nonlinear contribution from air [26, 27, 20]. A likely explanation is the much higher modulation-depth obtainable from KLM oscillators [113].

The main instability preventing power scaling in mode-locked, solitonic oscillators is multiple pulse formation when a critical peak power is reached. This results in more than one pulse circulating in the oscillator during a round-trip period<sup>9</sup> (see also figure 3.15). To ascertain clean pulses without satellites that would be masked by the low bandwidth of a sampling oscilloscope and photodiode (typ.  $>100 \text{ ps}$ ), the oscillator output was measured in a long-arm autocorrelator with a scan range of 2.6 ns. The more accurate intensity autocorrelator used to measure the pulse duration only had a scan range of 15 ps. Additionally, the intensity noise was measured with

<sup>9</sup>Under certain circumstances the resulting pulses can be very stable and have a fixed inter-pulse distance at integer fractions of the round-trip time, which is exploited in harmonic mode-locking to increase the repetition rate of a laser [114].

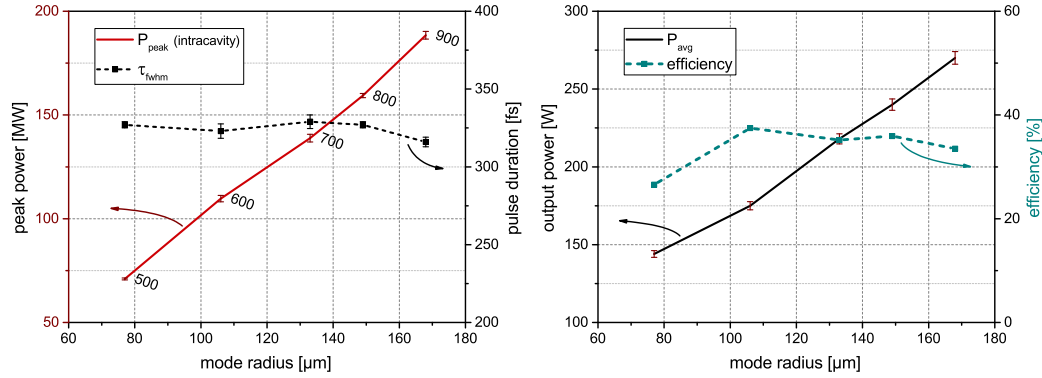


**Figure 3.18.** – Demonstration of intra-cavity peak power scaling with varying mode-radius in the Kerr-medium. The pulse duration stays approximately constant. The mode-radii are estimated from the maximum mode-size over the telescope stability range.

a 12 bit sampling oscilloscope with 3.5 GHz bandwidth and 40 GS/s sampling-rate. The characteristic rms value of 1 % could be determined in a frequency window of 1 Hz - 1 MHz. A strong source of noise was identified in turbulences from heated air inside the oscillator-housing.

### 3.3.4. Influence of dispersion

The minimal dispersion value required for stable operation in the oscillator with 900 mm ROC was at least  $-18,000 \text{ fs}^2$  GDD, introduced by 6 reflections on HD mirrors. Below this value the pulse buildup became unreliable with audible q-switching and damage to the Kerr medium. At this dispersion level the autocorrelation traces yielded 210 fs pulses with 127 W average power coupled out, corresponding to  $6.8 \text{ μJ}$  pulse energy. The intra-cavity peak power evaluated to 135 MW. The pulse measurements were repeated for increasing GDD per round-trip in steps of  $-6000 \text{ fs}^2$  up to  $-48,000 \text{ fs}^2$  with 16 reflections on the HD mirrors. At  $-48,000 \text{ fs}^2$  the pulse duration was 330 fs with 230 W average power and  $12.2 \text{ μJ}$  pulse energy coupled out. This corresponds to 156 MW intra-cavity peak power. The intra-cavity values are displayed in figure 3.19.

It is obvious that increased dispersion-compensation with higher GDD values can not influence the peak power obtainable in the cavity which remained nearly constant with the GDD. This is not surprising and congruent with the statement of the soliton area theorem as discussed already in sections 2.2.3 and 2.3.3. An increase of the negative GDD rather has the effect of compensating the rise in energy by increasing the pulse duration.

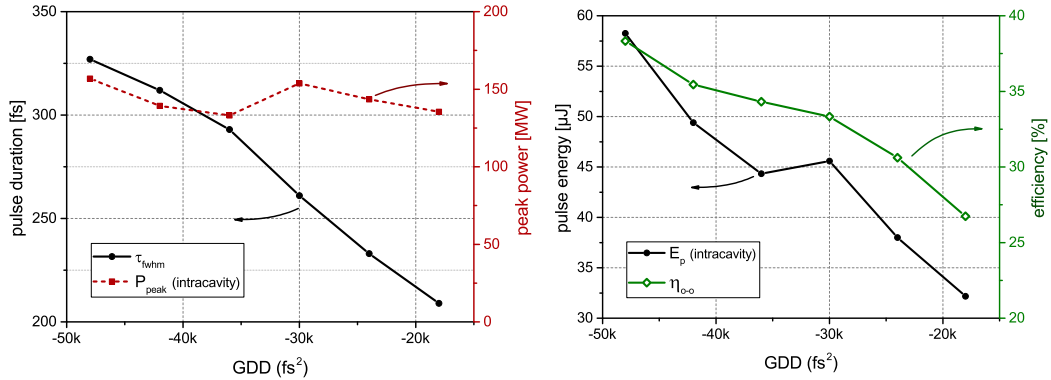


**Figure 3.19.** – (left): Intracavity peak power and output pulse duration and (right): pulse energy and optical-to-optical efficiency with varying GDD.

Note that the peak power is lower than the  $\sim 180$  MW maximum observed with the 900 mm ROC configuration in section 3.3.3. The reason was that during the here described GDD scaling experiment the hard aperture had a hole diameter of 5.5 mm. The optimal diameter of 5.0 mm allowed increasing the peak-power by a significant 20 %.

### 3.3.5. Output coupling

The most straightforward scaling of the output power is increasing the output coupler (OC) transmission. By doing so the gain has to be raised accordingly which leads to a narrowing of the spectrum and longer pulses (see e.g. [115]). Low OC losses therefore result in shorter pulses. The effect of the OC transmission on the performance of the 900-mm-ROC-oscillator was measured for OC transmissions ranging from 5 % to 25 %. These measurements were done before the final optimization of the hard aperture. Figure 3.20 (left) shows the effect on the pulse duration and intra-cavity peak power. Both peak-power and pulse duration change by 21 % and 25 % respectively. The difference could be attributed to different SAM and gain due to increasing thermal load on the thin disk for higher OC transmission. Nevertheless the longer pulse duration is tolerable when compared to the increase in output peak-power, see figure 3.20 (right). The use of higher output-coupling rates was hindered by the rollover in efficiency and the upper power limit of the pump-laser.

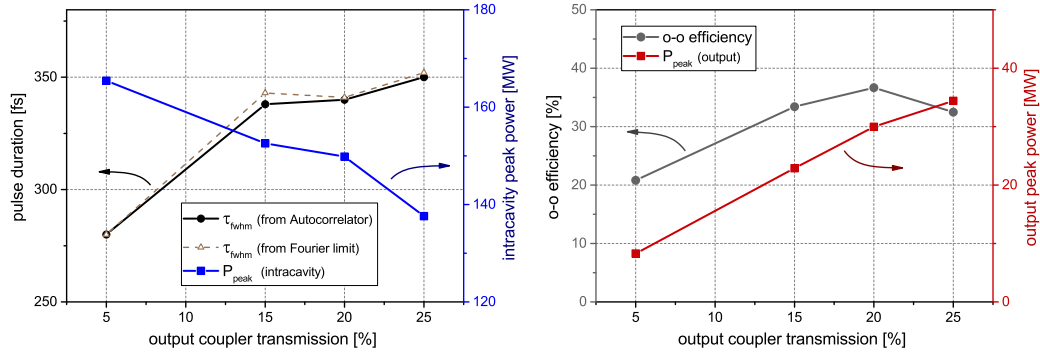


**Figure 3.20.** – (left) Dependence of pulse duration and intra-cavity peak-power on the output-coupler transmission. (right) Dependence of optical-optical efficiency and output peak power on the output-coupler transmission.

To boost the output power further an increased number of passes through the thin-disk is necessary. In a quick and dirty experiment it was tried to further pursue the approach of non-imaging disk passes as seen in figure 3.10 with three passes over the thin-disk<sup>10</sup>. However, due to low efficiency and increased thermal lensing as well as the, at that time, limited pump-diode power, this experiment was quickly abandoned. Investigation of the combination of KLM and the active multi-pass approach to power scaling ([116, 112]) is needed and currently carried out within the research group (see section §3.4).

### 3.4. Triple-pass with large output-coupler transmission

After the first failure to accomplishing an efficient 'triple'-pass, a simplified experiment was initiated. The experiment was planned by the author while the measurements and experimental realization was carried out by Markus Pötzlberger.

In order to check whether a triple-pass has a fundamentally limited applicability in KLM-resonators both a reference oscillator with double-pass as well as a triple-pass oscillator were realized (figure 3.23). The oscillators were operated with gradually increasing output-coupler transmission, while everything else (nonlinearity, GDD, focusing sections) were kept the same. The initially low output-coupler losses (<10 %) reduced the pump-power requirements such that possibly a pump-intensity limit for the utilized thin-disk might be deduced.

The intra-cavity GDD was  $-15,000 \text{ fs}^2$  and a 3 mm thick sapphire Kerr-medium was placed in the focusing section with curved 1 m ROC mirrors. The output-coupler transmission was increased until 20 % for the double-pass and up to 30 % for the triple-pass oscillator. As can be seen in figure 3.25, the triple-pass intra-cavity peak-power (the main indicator for oscillator performance) stayed comparable to or better than that of the double-pass oscillator. With 30 % output-coupler transmission the average output power was  $\sim 130 \text{ W}$  with 220 fs long pulses (figure 3.24) and 18 MW

<sup>10</sup>The mode is redirected 12 times through the thin-disk volume during one round-trip.

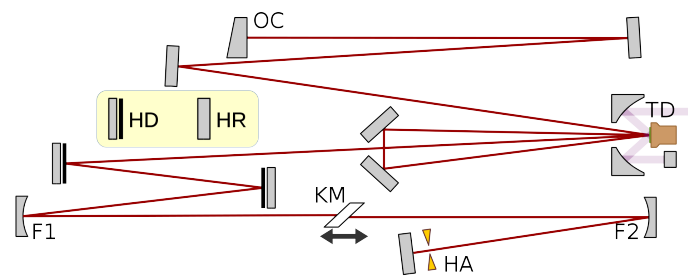


**Figure 3.21.** – Reference, double-pass oscillator

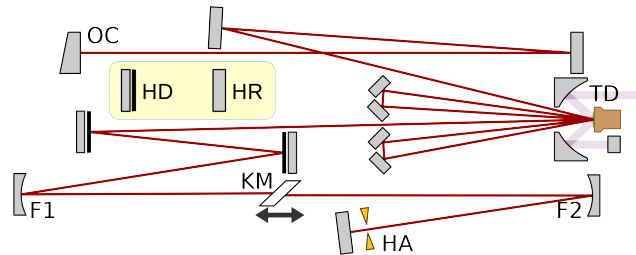


**Figure 3.22.** – Triple-pass oscillator.

**Figure 3.23.** – (top): Double-pass oscillator with 28 MHz repetition-rate. (bottom): Triple-pass oscillator also with 28 MHz repetition-rate. OC: output-coupler, HD: highly-dispersive mirror, HR: highly reflective mirror, HA: hard aperture, KM: Kerr-medium, TD: thin-disk, F1,F2: spherical focusing mirrors, both with 1 m ROC.

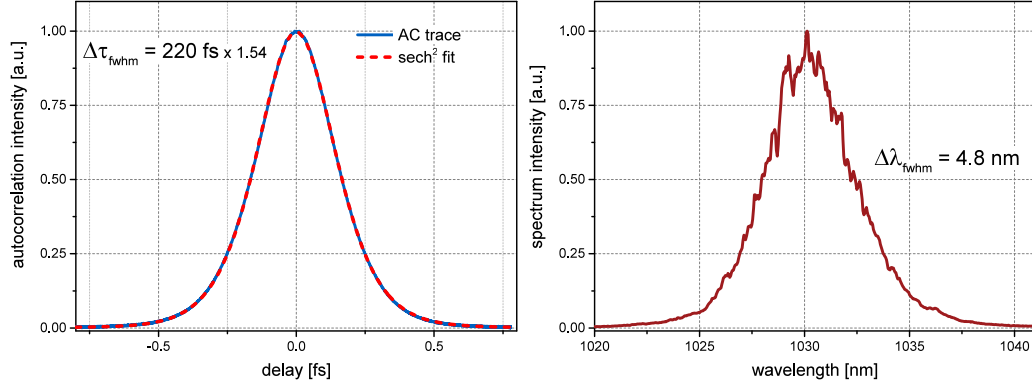


**Figure 3.24.** – (left): Autocorrelation signal of the 30 % OC triple-pass with 220 fs pulse duration. (right): Spectrum output of same oscillator.

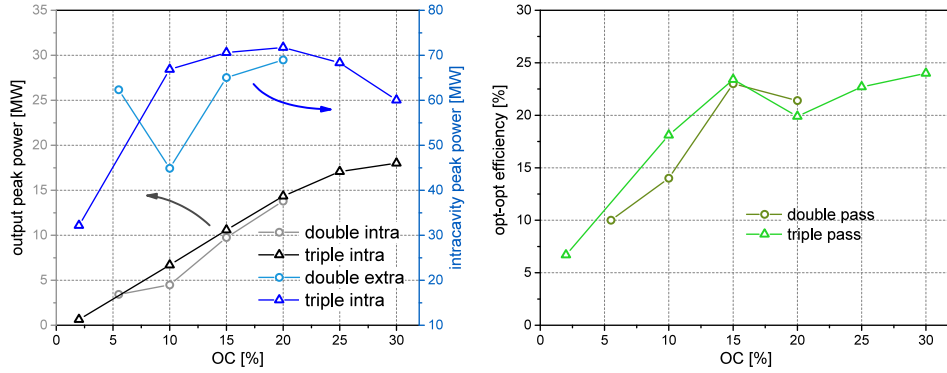


**Figure 3.25.** – (left): Extra- and intra-cavity peak powers measured with triple-pass and double-pass reference-cavity for various output-coupler transmissions. (right): Optical-to-optical efficiencies of both oscillators for different output-coupler transmissions.

output peak-power. With a temperature-stabilized housing the output-power could be stabilized having an rms power fluctuation of 0.1 % over the working-day.

Two factors could possibly be deemed responsible for the failure of the first ‘quick-and-dirty’ triple-pass tryout (section 3.3.5). (i) The higher pump-irradiation of up to 10 kW/cm<sup>2</sup> as compared to 6.7 kW/cm<sup>2</sup>. (ii) The higher intra-cavity average power of 1.3 kW as compared to 430 W. Case (i) is the most likely. The only three times higher average power (ii) would not be sufficient to induce a noticeable curvature-change in the additional 2 HR folding mirrors.

The demonstration of the triple-pass in an efficient KLM oscillator gives hope for drastically improved power output from KLM thin-disk lasers. For example, the doubling of the output-coupler-transmission of the currently top-performing KLM-oscillator [32] would yield pulses with 130 MW peak-power.

A next step is the realization of an imaging multi-pass as described in [69, 112] with more than three passes and output-coupling rates larger than 30 %. Possibly a thin-disk with reduced thickness might be required to sustain a clean thin-disk curvature [112]. However, there would be a trade-off between curvature-change and

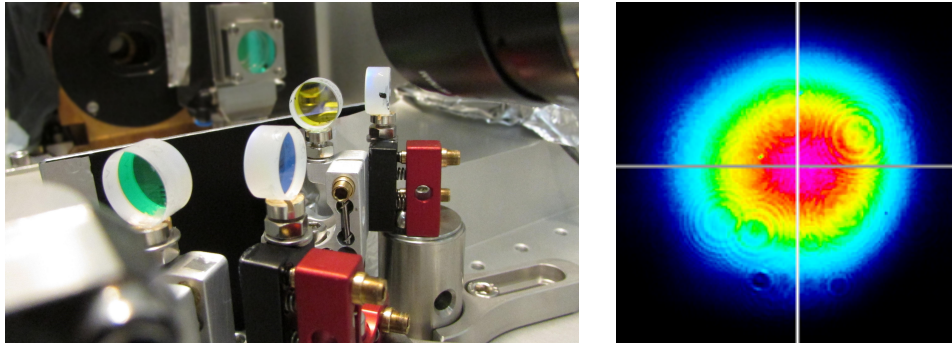


**Figure 3.26.** – (left): Triple-pass folding-mirrors in front of the thin-disk module in the temperature-stabilized oscillator-housing. (right): Output beam-profile of the triple-pass oscillator.

available gain in the oscillator, due to the limits of Yb:YAG doping-concentration.

### 3.5. Intra-cavity nonlinearities and further power scaling

In order to facilitate subsequent pulse-compression, pulses shorter than the  $\sim 300$  fs reached from the oscillator (oscillator with 900 mm ROC, see section 3.3.3) were deemed highly beneficial. To extract shorter pulses, the value of the intra-cavity GDD had to be reduced. With  $-18,000$  fs<sup>2</sup> per round-trip the pulse-duration reduced to 210 fs and the output pulse-energy to  $\sim 7$   $\mu$ J (see section 3.3.4) with 127 W average output power. This setup with a sapphire KM of 1 mm thickness and a reduced-pressure environment (500 mbar of air) for improved pointing-stability was plagued by frequent damage to the KM, occurring within a few days of operation. It was assumed that the reduced air-pressure might contribute to KM-degradation due to inferior heat removal from less convection. However, cooling the KM did not improve the situation. In the ensuing quest to finding a suitable Kerr-material with better long-term stability than sapphire, crystalline quartz (SiO<sub>2</sub>) was the next-best candidate due to its large band-gap energy as well as higher heat-conductivity as compared to fused silica (also SiO<sub>2</sub>). An already available 3 mm thick quartz window took the place of the 1 mm thick sapphire for testing purposes. The output peak-power reduced from 28 MW to only 22 MW which was a little surprising and must be attributed to the change in SAM and/or different thermal lensing in the quartz plate<sup>11</sup>. The pulses showed a significantly shorter duration and could be tuned from 160 fs to 190 fs. Prolonged utilization in the oscillator over few days did not produce any sign of degradation. Due to its intrinsic birefringence the quartz-crystal placed under Brewster's angle, despite the c-cut, rotated a small fraction of the intra-cavity power to the s-polarization, along with a negligibly small portion of second harmonic radiation (figure 3.27(right)). The source of the depolarization can be an imperfect c-cut, or stress-induced birefringence in the thin-disk. The spectral content of the two polarization directions is compared in figure 3.27(left). The much

<sup>11</sup>The soliton area-theorem, eq. 2.10 on page 10 predicts a reduction to about 12 MW.

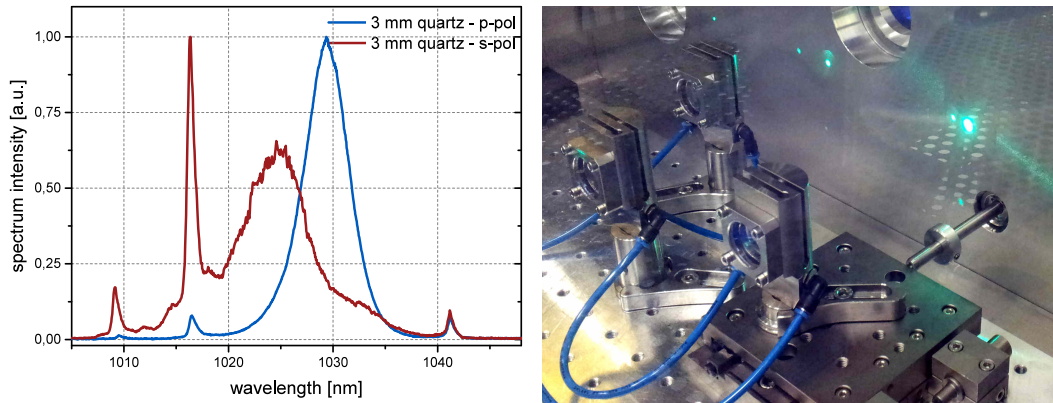


**Figure 3.27.** – (left): Polarization-dependent spectra from oscillator with 3 mm crystalline quartz Kerr-medium. (right): Second-harmonic radiation generated within the oscillator and leaking through the 1030 nm HR-coatings.

larger spectral bandwidth and blue-shift of the s-polarized light might originate from strong cross-phase modulation in the quartz as commonly observed with vector solitons in birefringent, mode-locked fiber lasers [117, 118, 119].

**Power scaled oscillator relying on strong Kerr-nonlinearity** A further experiment was carried out with the goal to increase the oscillator peak-power while retaining the enhanced bandwidth and short pulse duration of the oscillator using quartz for a KM, such as described above. The overall cavity design remained similar to that in section 3.3.1 with only a small adjustment to the static resonator section, namely a reduction of the distance between the consecutive TD passes. The resonator setup is sketched in figure 3.28.

By picking a nonlinear resonator section with 2000 mm ROC focusing mirrors, the peak power was expected to double with respect to the 900 mm ROC oscillator. Spanning over 2 m from mirror F1 to F2 the nonlinear section had to be folded twice with plane HR mirrors. A set of turning mirrors on a translation stage was arranged to provide stability tuning while keeping the optical axis aligned. This was especially important when trying to find the mode-locking threshold while scanning over a relatively large distance of a few centimeters with the translation stage. A low noise, 100 mm travel stage allowed to shift the KM along the optical axis. As explained in section 3.5.3 this was necessary to allow power optimization with the Kerr-medium position over the relatively long Rayleigh range of the intra-cavity focus. Keeping the same KM as in section 3.3.1, sapphire with a thickness of 1 mm, for better comparison did not turn out fruitful. The oscillator was hard to mode-lock and only very narrow-band pulses with few tens of Watt output power could be observed. At the same time the housing needed to be evacuated down to 500 mbar to start mode-locking.

A 6 mm thick quartz KM instead allowed uncomplicated pulse-buildup. Minimization of the GDD down to  $-9,000 \text{ fs}^2$  even allowed the generation of  $\sim 125 \text{ fs}$  pulses (figure 3.29), however with only 70 W average and 32 MW peak output power of

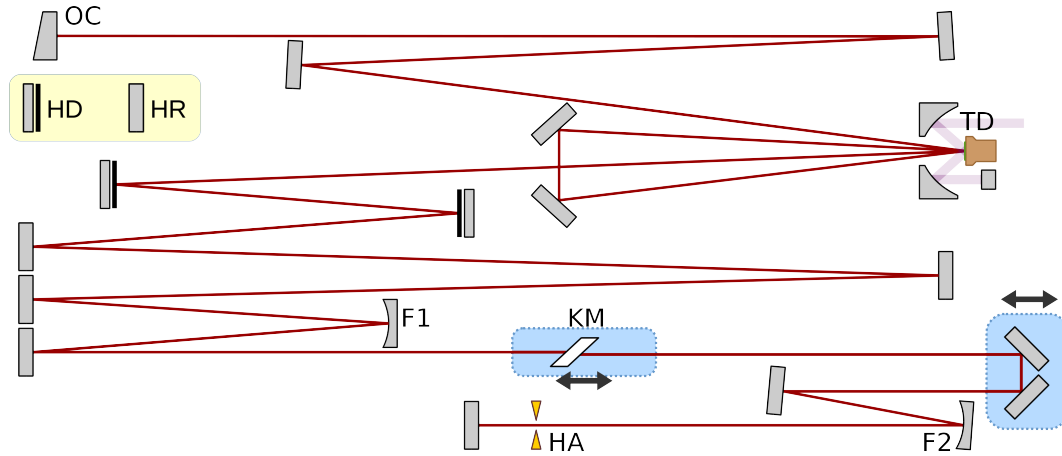


**Figure 3.28.** – 2000 mm ROC oscillator sketch. OC: output-coupler, HD: highly-dispersive mirror, HR: highly reflective mirror, HA: hard aperture, KM: Kerr-medium, TD: thin-disk, F1,F2: spherical focusing mirrors.

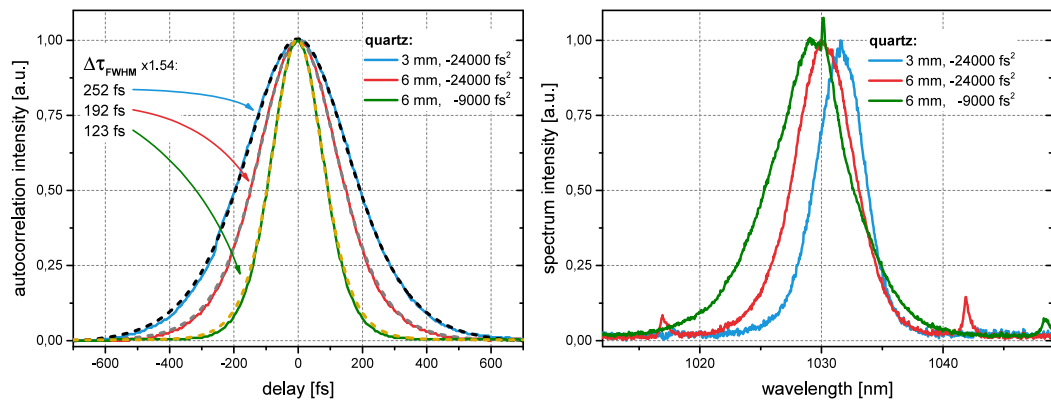


**Figure 3.29.** – Oscillator autocorrelation and spectrum traces with 3 and 6 mm thick crystalline quartz KM for varying intra-cavity GDD values.

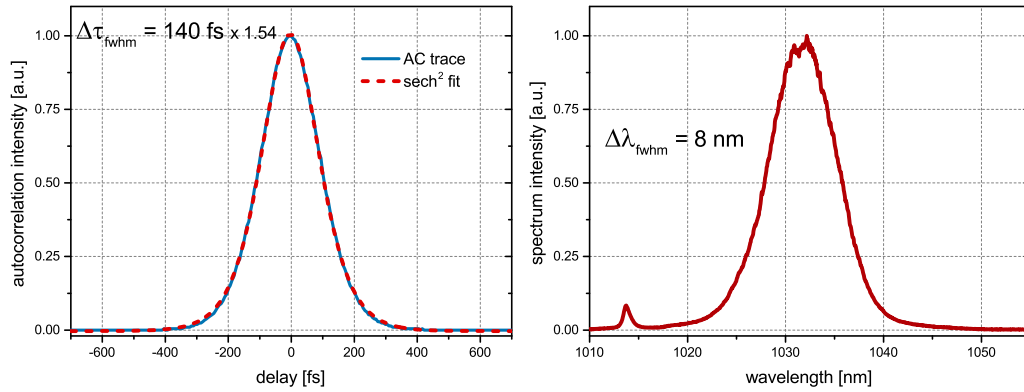


**Figure 3.30.** – Intensity autocorrelation trace with  $sech^2$  fit and spectrum of the output pulses with 62 MW peak-power. The KM was 5 mm thick sapphire.

which 3 W were in the rotated s-polarization. This corresponds to an intra-cavity peak-power of 200 MW. At  $-24,000 \text{ fs}^2$  the pulse-duration increased to 150 fs with 153 avg. output-power, corresponding to 300 MW intra-cavity peak-power. A further reduction of the pulse-duration via a quartz KM of 10 mm was not possible and resulted at best in 150 fs pulses with a much reduced intra-cavity peak-power of only 120 MW. This seems reasonable since an increased SPM due to the thicker KM has to be traded off against the earlier saturation of the SAM.

In order to avoid the depolarization-losses observed with the birefringent quartz it was replaced again with sapphire of varying thicknesses<sup>12</sup>. Unlike in the 900-mm-ROC oscillator the sapphire-KM did not degrade<sup>13</sup>. This might have several reasons (i) less impurities in the crystals, (ii) reduced local temperatures due to higher sample-thickness and transport into the depth of the bulk crystal, (iii) stronger SAM and therefore higher stability against noise-induced peak-power fluctuations. The highest peak-powers were obtained for a sapphire-plate of 5 mm thickness.

The optimal GDD of  $-12,000 \text{ fs}^2$  was introduced by four reflections per round-trip on mirrors with the proven HD coating (3.3.2 on page 27). The output coupler transmission was kept at 15 % and a hard aperture hole diameter of 5.0 mm proved the best compromise between opt.-opt. efficiency and pulse-duration. The relatively low GDD value prohibited mode-locking under normal air atmosphere such that the intra-cavity nonlinearity had to be reduced by evacuating the oscillator housing to  $\sim 500 \text{ mbar}$ .

Under these conditions the oscillator could be mode-locked starting with about 430 W intra-cavity CW radiation which increased up to 1030 W average power in ML operation. With a repetition rate of 15.6 MHz the pulse energy is calculated as 66  $\mu\text{J}$  intra- and 10  $\mu\text{J}$  extra-cavity, corresponding to 155 W average output power. The optical spectrum had a bandwidth of 8 nm and a pronounced red-shift

<sup>12</sup>The choice was between quickly available windows from a shelf in the lab, namely 1, 2, 3 and 5 mm thickness.

<sup>13</sup>The sapphire-plate with optimized thickness has been working for the last 1 1/2 years continuously at the published oscillator-parameters ([32]) without a single occurrence of damage.

of the peak wavelength is visible<sup>14</sup> (figure 3.30). Another pronounced feature is the Kelly sideband, visible as small spike displaced from the central wavelength<sup>15</sup>. The autocorrelation trace shows a FWHM pulse width of 140 fs (x 1.54) with a near perfect *sech*<sup>2</sup> shape. Thus the time-bandwidth product evaluates to  $\sim 0.315$  which proves unchirped *sech*<sup>2</sup> shaped pulses with an intra- and extra-cavity peak power of more than 410 MW and 62 MW respectively. Single pulse operation was again verified with a digital sampling oscilloscope (time resolution  $> 100$  ps), a long-arm autocorrelator (2.6 ns scan range, see A.4) and an accurate autocorrelator with 15 ps scan range. The SPM factor  $\gamma_{spm}$  of this cavity is estimated from the soliton area theorem to be  $0.0046 \text{ MW}^{-1}$  and  $0.0041 \text{ MW}^{-1}$  from mode-calculations. At 410 MW intra-cavity the resulting nonlinear phase shift per round-trip is therefore  $0.61\pi$  and  $4/3$  times higher than in the 900 mm ROC cavity.

In a 1 Hz - 1 MHz window the rms intensity noise was measured to be  $< 0.5 \%$ . This compares to the noise level of the only high power mode-locked oscillator that has been carrier-envelope-phase stabilized so far and raises hope that the same might be done in the future for such an oscillator with a peak-power more than 15 times higher [22].

The obtained intra-cavity peak power fits closely to the linear extrapolation of the previously obtained peak power results, even slightly overachieving.

### 3.5.1. Intensity noise

The intensity noise of the oscillator was measured on a photodiode with a radio-frequency (RF) spectrum-analyzer as well as with a sampling oscilloscope. The carrier signal at 15.6 MHz was 75 dB above the side-band level (see figure 3.32). The most significant noise sources lay in the acoustic range above 1 kHz<sup>16</sup> and below 9 kHz being typical of technical noise as from the attached chiller-pumps and turbulent water-flow. Frequencies lower than 25 Hz lay outside the measurement range. The integrated rms intensity noise of  $\sim 0.2 \%$  in the bandwidth 25 Hz - 12 kHz fits well to the rms value of  $\sim 0.3 \%$  measured with the sampling oscilloscope (see figure 3.33).

### 3.5.2. Influence of air

By integrating over the caustic of a Gaussian beam one can easily show that the nonlinear coefficient  $\gamma_{spm}$  is a constant for all beam waist sizes. This means that, provided a pulse can propagate freely over a considerable portion of the caustic, including the focus, the nonlinear phase collected by the pulse is independent of the focal spot size.

---

<sup>14</sup>These red-shifts are more commonly seen in high bandwidth oscillators [120, 121]. The numerical investigation in [121] suggests Raman-scattering and re-absorption in the gain as the main causes for the spectral shift.

<sup>15</sup>The Kelly sidebands should actually be symmetric, It is not clear why the red spike is not also visible. They both turn up with a different spectrometer, e.g. figure 5.32 on page 94.

<sup>16</sup>Relaxation oscillations of Yb:YAG with  $\sim 1$  ms upper state lifetime.

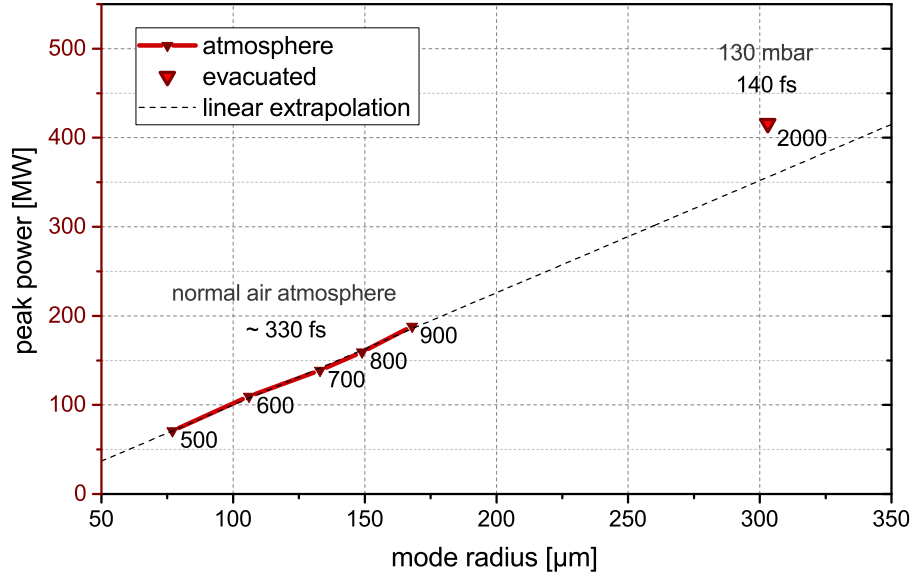


**Figure 3.31.** – Extended geometrical peak-power scaling with higher intra-cavity nonlinearity. The figures underneath each triangle indicate the ROC used in the nonlinear resonator section.

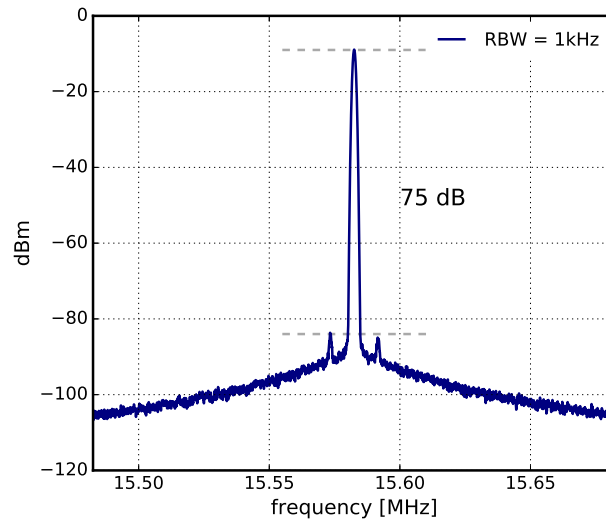


**Figure 3.32.** – Carrier signal at the repetition rate of the 2 m ROC oscillator. The signal level is 75 dB above the side-bands.

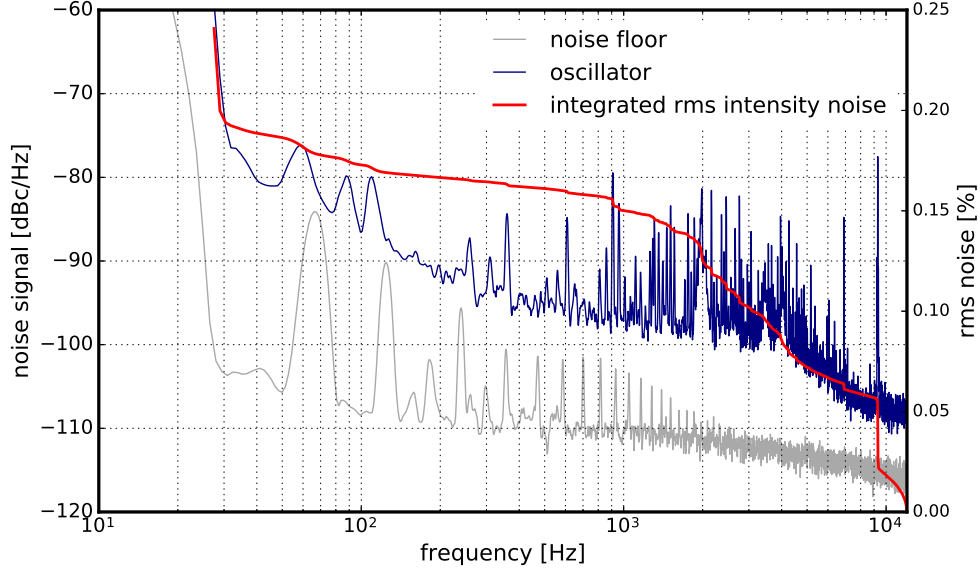


**Figure 3.33.** – Low frequency intensity noise of the oscillator.

$$\gamma_{spm} = \frac{4n_2}{\lambda} \int_{-\infty}^{\infty} \frac{dz}{w^2(z)} = \frac{4n_2\pi^2}{\lambda^2} \quad (3.4)$$

Furthermore, the fraction of nonlinear phase arising from a bulk medium of thickness  $t$  located in the focus can then be estimated just as easily.

$$\begin{aligned} \frac{\gamma_k}{\gamma_k + \gamma_{air}} &\approx \frac{n_{2,k} \int_0^{t/2} \frac{dz}{w^2(z)}}{n_{2,air} \int_{t/2}^{\infty} \frac{dz}{w^2(z)} + n_{2,k} \int_0^{t/2} \frac{dz}{w^2(z)}} \\ &= \frac{n_{2,k} \arctan\left(\frac{\lambda t}{2\pi w_0^2}\right)}{\pi n_{2,air} - 2(n_{2,air} - n_{2,k}) \arctan\left(\frac{\lambda t}{2\pi w_0^2}\right)} \end{aligned} \quad (3.5)$$

Here  $\gamma_k$ ,  $\gamma_{air}$  are the respective contributions of the KM and air to the SPM coefficient with their respective second order nonlinear refractive indices  $n_k$  and  $n_{air}$ . This expression gives an upper bound for the contribution of the Kerr-medium to the total nonlinear phase-shift in geometrically power-scaled, air filled oscillators.

If we extend the geometrical power scaling scheme even further as depicted in figure 3.34 the fractional contribution of air to the nonlinear phase shift increases. In general this is not beneficial. In this situation thermally or otherwise induced pressure variations in air have an increased contribution to oscillator noise due to the nonlinear coupling to SPM and SAM. Also, the nonlinear mode-shaping that provides the necessary SAM is then no more solely defined by the Kerr-medium but Kerr-lensing in air would contribute as well, making controlled optimization of the SAM more difficult. The only way to avoid the atmospheric influence is by

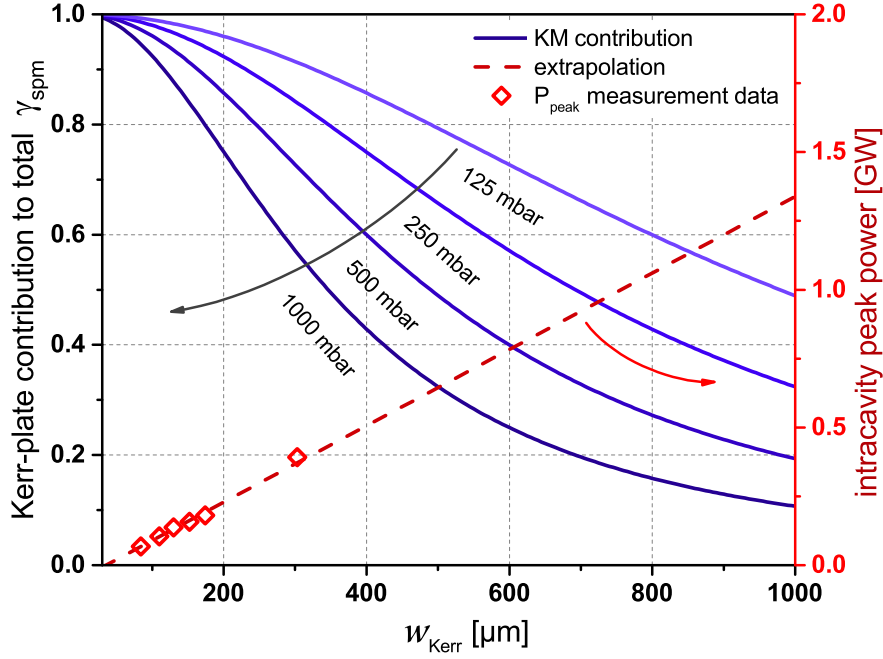


**Figure 3.34.** – Left y-axis: Fractional contribution of the Kerr-plate to the total nonlinear phase-shift inside the oscillator for different atmospheric air pressure. Right y-axis: achieved and extrapolated trend of the peak-power scaling.

evacuation. Figure 3.34 shows some upper bounds for the Kerr-medium contribution to the nonlinear phase-shift over the KM mode-size with varying pressures. The experimentally obtained peak powers are also depicted. One can see that for 'low' power KLM oscillators, such as the ones studied in section 3.3.2, operation under normal air-pressure corresponds to Kerr-medium contributions of  $\gamma_k/(\gamma_k + \gamma_{air}) > 0.8$ . The oscillator in section 3.5 was only stable after reduction of the air-pressure to  $< 500$  mbar, corresponding roughly to the same fractional contribution. Reaching the GW-level by linear extension of the obtained results would require pressures  $\leq 100$  mbar.

For the oscillator described in section 3.3.1 with up to 900 mm ROC, varying the air pressure or flooding with different gases had only negligible influence on the output parameters. Evacuation of the 900 mm ROC oscillator housing down to 450 mbar lead to a small increase in average output power by a factor of 3 %. The effects on the optical spectrum and pulse duration were negligible. A further reduction of the pressure would have required an increase in pump power to avoid destabilization. However, the pump-diodes available at that time were already driven at their maximum output power and no attempts were made to evacuate this particular setup any further.

This behavior changed, when the mode size in the KM was increased as in section 3.5. Reduction of the air pressure inside the 2000 mm ROC oscillator housing yielded a much steeper increase in peak power (figure 3.35). The peak-power dependent

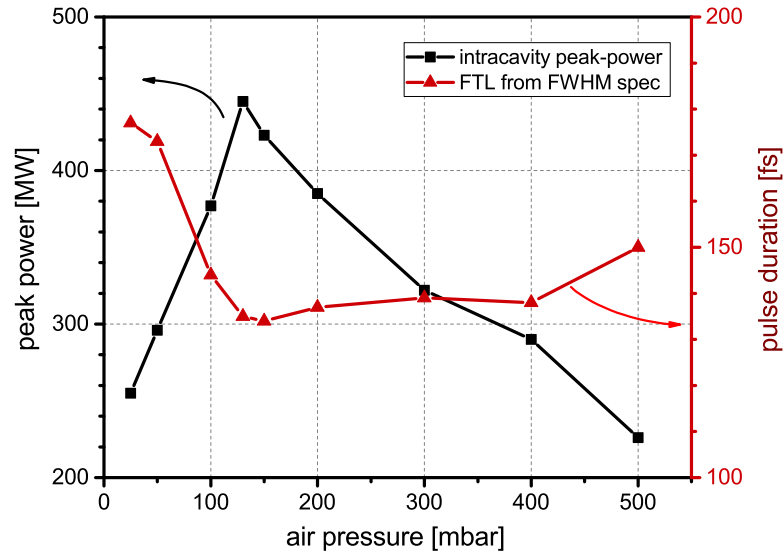


**Figure 3.35.** – Dependence of intra-cavity peak power and pulse duration on the residual air pressure inside the oscillator housing.

red-shift of the optical spectrum is also visible in figure 3.36. A critical pressure of 130 mbar was measured, below which the peak power began dropping and the pulse duration also increased. The existence of this critical pressure and comparison with experimental data from [122] suggest another physical mechanism at play. Experience from previous experiments prompts me to believe that a thermal influence might be responsible. Due to the lower gas density at low pressure, the heat removal by convection is greatly reduced such that the temperature in the mirror surface can rise. A strong effect in the HR coatings is unlikely, however the HD mirrors show a higher tendency to absorb and heat up. Since small errors below 0.5 % in the coating thickness, induced by thermal expansion and stress, can already make a big difference in the HD mirror properties [82]. Taking into account that the optical bandwidth of the pulses already begins to exceed the bandwidth of the HD mirrors (see 3.12 on page 28) this might lead to the observed drop in the peak power and change in pulse duration. Additional thermal lensing might also influence the cavity mode. Measurement of the mirror-temperatures in the evacuated state are still to be carried out.

Should the temperature-rise hypothesis turn out to be appropriate, it can seriously impede further power scaling in cavities with larger ROC that require even lower air-pressure. Possible solutions are the use of substrates with high thermal conductivity (see *Dispersive mirrors* on page 27) or flooding with a gas of low nonlinearity such as Helium. A reduction of the intra-cavity average power either by larger output coupler transmission or by an increase in cavity length might also help to lower temperatures in the coatings and raise the extra-cavity peak power of the pulses.

Along with the intra-cavity peak power the optical spectrum red-shifted (figure 3.36).

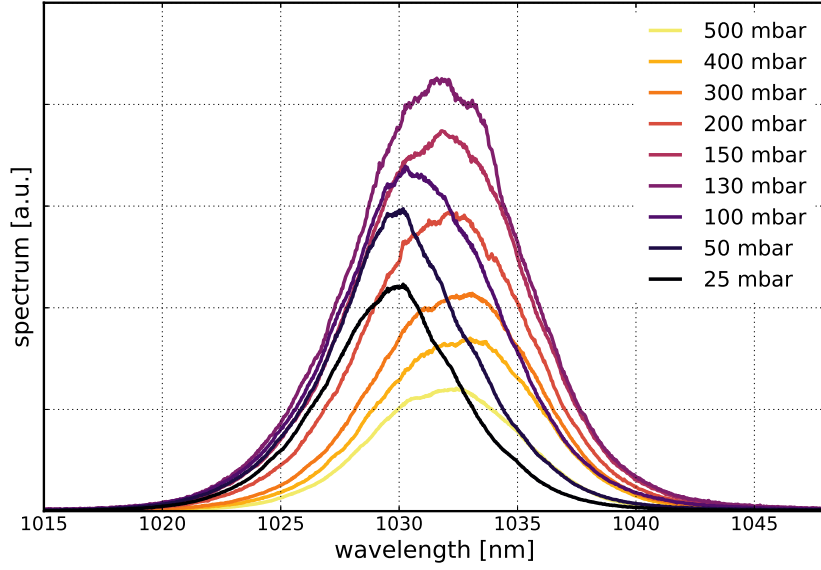


**Figure 3.36.** – Spectra for varying air pressure inside the oscillator housing. The y-scaling is exaggerated in order to better distinguish between different pressure values.

	SiO <sub>2</sub> (fused)	Al <sub>2</sub> O <sub>3</sub>	CaF <sub>2</sub>	YAG
$n_2 \times 10^{-20}$ [m <sup>2</sup> W <sup>-1</sup> ]	2.5 [123]	3 [124]	1.9 [125]	7.5 [125]
band gap [eV]	9.9 [126]	8.8 [126]	10 [125]	4.7 [127]
thermal conductivity [Wm <sup>-1</sup> K <sup>-1</sup> ]	1.38 [125]	46 [125]	9.7 [125]	13.4 [125]
dn/dT x 10 <sup>-6</sup> [K <sup>-1</sup> ] *	9 [128]	13 [129, 130]	-12 [128]	9 [125]

**Table 3.2.** – Nonlinear refractive index, band-gap and thermal conductivity for some interesting materials around 1  $\mu$ m wavelength. \* Thermo optical coefficients near  $\sim$ 300  $^{\circ}$ K and also 1  $\mu$ m wavelength.

Once the air pressure fell below 130 mbar the spectrum centered again at the peak-emission wavelength of Yb:YAG.

### 3.5.3. Influence of the Kerr-medium

#### Material choice

The approximation of the Kerr-lens as a thin-lens model is a fair assumption for the high power KLM oscillators studied. The Rayleigh lengths considered are easily an order of magnitude longer than the dimensions of the utilized Kerr-media. For a given caustic the strength of the Kerr-lens is thus only defined by the thickness  $d$  and  $n_2$  of the transmitting material. One can therefore predict that changing Kerr-medium parameters ( $d$  and  $n_2$ ) impacts only the saturation power of the SAM.

Less trivial to predict are thermal lenses arising from sample impurities and intrinsic absorption of the Kerr-materials. It was at first quite surprising that

simply exchanging a sapphire plate for a fused silica plate of the same thickness was detrimental for laser performance. A non-negligible thermal lens in the KM could be unambiguously identified, which limited the intra-cavity average power and prevented mode-locking. The high intensities in the KM would suggest multi-photon absorption as possible main contributor to heating and therefore high band gap materials should be the first choice. However, seeing that thermal instabilities arise already in CW mode, linear absorption in contaminants is more likely. The critical parameter seems to be thermal conductivity, completely ruling out glasses (see table 3.2 for some of tried materials). Aside from the material the second biggest impact factor was the choice of supplier, some of them offering wildly differing material quality and purity.

### Peak-power optimization

The KLM oscillator performance depends not only on the resonator's proximity to the stability edge but also on the position of the Kerr-medium relative to the focus in the nonlinear focusing section. In order to optimize the SAM parameters, i.e. the saturation power ( $P_{max}$  for a cubic-quintic modulator), the Kerr-medium has to be moved out of the focus. This leads to a decrease of the initial slope of the SAM (or KLM sensitivity  $s$ . See equation (3.3)). While the maximal peak power is optimized with increasing distance to the focus, the ability to initiate stable pulse buildup decreases. Apart from the inability to start ML the spiking during initiation of mode-locking turned out to be a real problem in KLM oscillators with high intra-cavity peak-powers of 50 MW or more. With insufficient saturation of the SAM the tendency toward spiking increases during the transient pulse-buildup phase [72]. The oscillator might still be persuaded to initiate mode-locking by increasing the pump-power beyond the threshold required for stable mode-locking, however, perturbations can then easily damage the intra-cavity optics, especially the Kerr-medium and HD mirror coatings (figure 3.37).

A solution to this issue is constituted of designated positions for the Kerr-medium for starting and for optimized KLM operation. After initiation of KLM in the starting position where the SAM more easily saturates, the KM is shifted into the position of optimal operation. Figures 3.38 and 3.39 demonstrate the KM-position dependent change in the spectrum and peak-power of the pulses.

Heeding this starting and optimization procedure the intra-cavity peak-power can be raised by more than a factor 2 when the Kerr-medium is properly adjusted while avoiding damage to optics. In principle the combination of KLM with a SESAM might also provide the desired smooth pulse-buildup. However, this would add the inherent problems of high-power SESAM-design, among them thermal lensing or hard to control wavefront distortions from the SESAM surface irregularities. Active modulation might likewise be an alternative way to control the pulse-buildup.

## 3.6. Front end for an all thin-disk OPCPA system

In order to boost the stability of a planned regenerative thin disk amplifier and consequent optical parametric chirped pulse amplifier (OPCPA) chain a high power

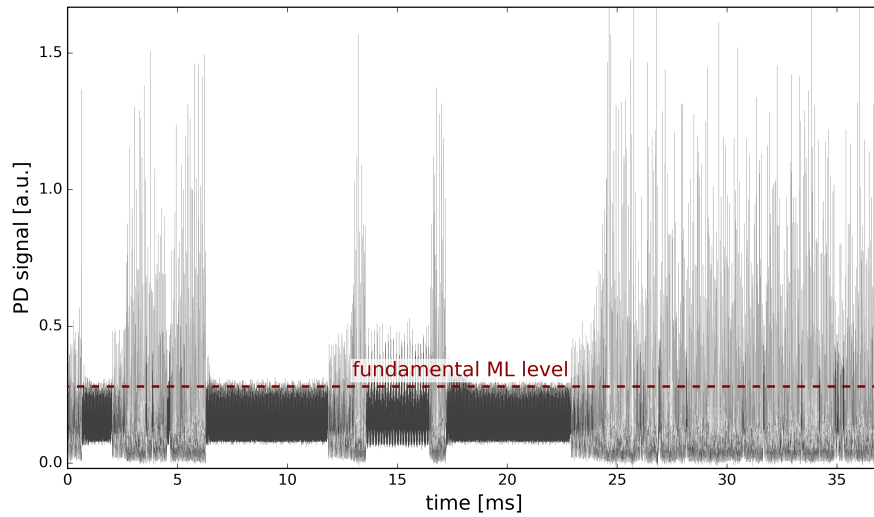


**Figure 3.37.** – Spiking during initiation of KLM.

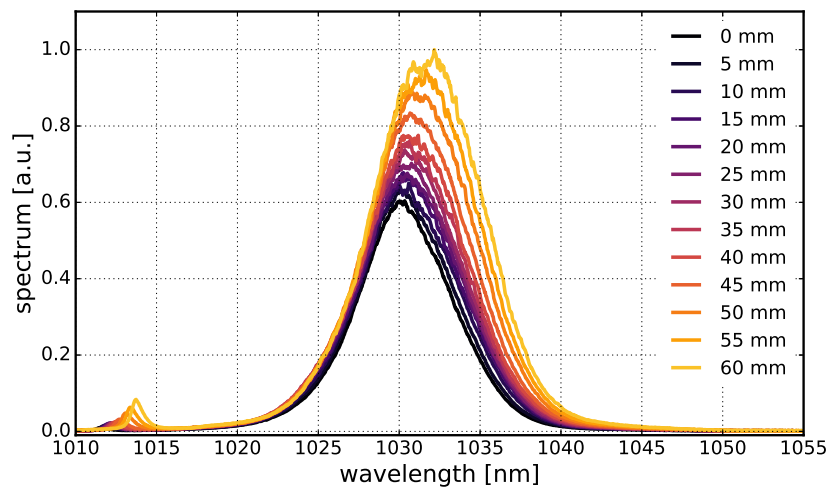


**Figure 3.38.** – Spectra of pulses with shift of the Kerr-medium position. Position '0 mm' is closest to the focus of the CW mode.

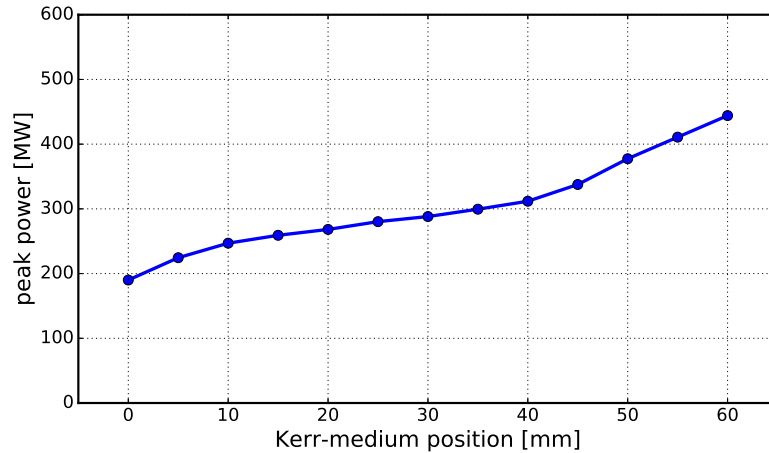


**Figure 3.39.** – Intra-cavity peak-power in dependence of the Kerr-medium position. Position '0 mm' is closest to the CW mode focus.

seed source had to be built. The output pulses of the amplifier were intended to be CEP-stable. Although this goal was later realized more elegantly via difference-frequency generation (DFG, described in [131]) the initial, main motivation for the KLM seed-oscillator was that the first and at that time only demonstration of CEP-stability in a high-power oscillator was within this research-group with a KLM TD-oscillator [22]. CEP-stabilization was initially planned via the use of an intra-cavity acousto-optic modulator (AOM) but never implemented due to the demonstration of the DFG-scheme. As a secondary advantage of a high pulse-energy seed, the output bandwidth from a chirped-pulse regenerative amplifier can be increased by reducing the amount of amplification necessary and thereby lessening the effect of spectral gain narrowing [132]. Therefore, shorter pulses and better re-compression quality can be achieved. The seed pulse energies required to give an improvement were expected to lay in the  $\mu\text{J}$  region, which are not reached directly with fiber oscillators but can naturally be generated with thin disk oscillators. The pulse duration from the regenerative amplifier could be reduced as described in [133]. The amplified output pulses with 20 mJ energy at 5 kHz repetition rate were compressed to 1 ps.

The initial design goals for the oscillator were

- low noise and low drift for better CEP-stabilization.
- high pulse energy and relatively large spectral bandwidth
- low repetition rate for easy pulse picking
- high reliability and operation in air

To achieve low drift and high reliability the average power output from the oscillator was limited by a relatively long resonator. The resonator length was  $\sim 12$  m corresponding to 13 MHz pulse repetition rate. With a 13 % output coupler a

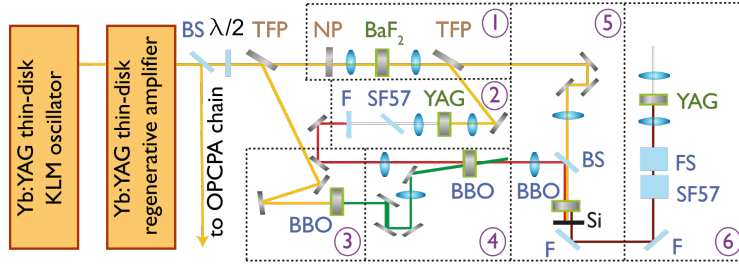


**Figure 3.40.** – OPCPA setup seeded by the KLM thin-disk oscillator. The oscillator seed is amplified in a regenerative amplifier to 20 mJ pulse energy 5 kHz repetition rate. Steps 1 to 4 are used to derive a CEP-stable seed in the BBO at point 5 via difference frequency generation as described in [131]. The figure is adapted from the same source.

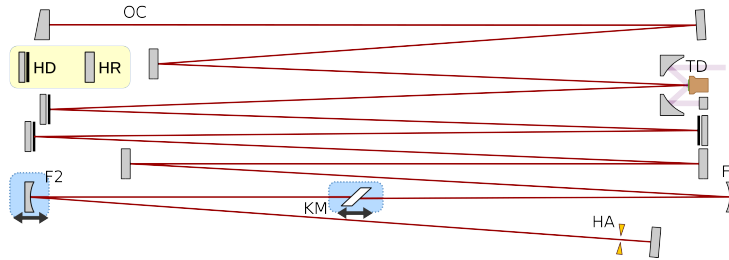


**Figure 3.41.** – Layout of the 13 MHz seed oscillator. OC: output-coupler, HD: highly-dispersive mirror, HR: highly reflective mirror, HA: hard aperture, KM: Kerr-medium, TD: thin-disk, F1,F2: spherical focusing mirrors.

single-pass on the Yb:YAG thin disk provided sufficient gain. The nonlinear KLM section was chosen symmetric and consisted of curved 1 m ROC mirrors with a 1 mm thick sapphire Kerr-medium in the focus and a water cooled hard aperture (5 mm diameter) near the end-mirror. Together with an intra-cavity GDD of  $-18,000 \text{ fs}^2$  per round-trip the oscillator is mode-locked producing  $2 \mu\text{J}$  pulses with 350 fs pulse duration. The average output power is 25 W.

The whole setup was built on a water-cooled breadboard resulting in relatively low thermal drift. The alignment between consecutive turn-on and shut-down events is stable such that the oscillator can run without realignment from day to day. The rms beam pointing deviation is  $<0.6 \%$  of the beam-size over the course of one hour. The average output power stability over a typical working day is displayed in figure 3.43 and measures 0.6 % rms deviation during  $\sim 6$  hours.

The laser has been in operation continuously since the last 3 years and demonstrates the high reliability that KLM thin-disk oscillators can reach. Experiences for long-term operation of

### 3.7. Summary

To conclude this section a summary of the parameters of the developed Kerr-lens mode-locked thin-disk oscillators is given in table 3.3.

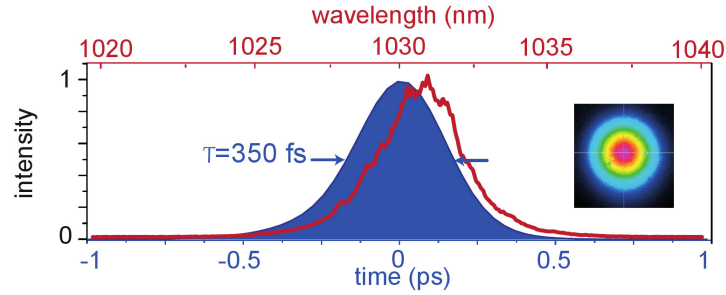


**Figure 3.42.** – 3 nm wide spectrum and FROG-retrieved pulse-shape of the 13 MHz seed-oscillator. The inset shows the output beam-profile. Figure taken from [133]

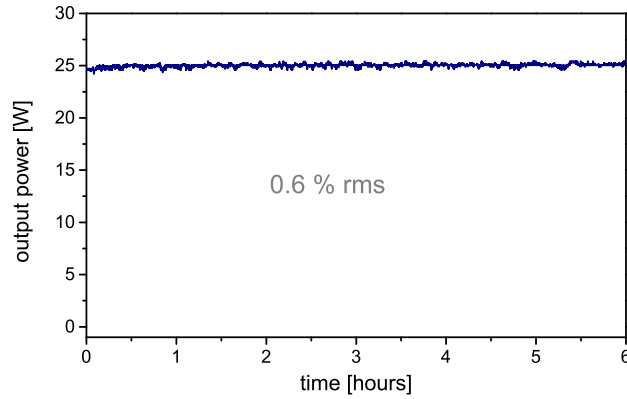


**Figure 3.43.** – Average power stability of the TD KLM seed oscillator during a typical working-day.

		atmosphere			evacuated
$\lambda_{center}$	[nm]	1030 (Yb:YAG)			
$f_{rep}$	[MHz]	18.8	28	13	15.6
ROC	[m]	0.9	1.0	1.0	2.0
OC transmission	[%]	21	30	13	15
GDD	[fs <sup>2</sup> ]	-48,000	-15,000	-18,000	-12,000
$\Delta\lambda$	[nm]	3.4	4.8	3	8
$\Delta\tau_{fwhm}$	[fs]	320	220	350	140
$P_{avg}$ (extra / intra)	[W]	270 / 1300	130/430	25/190	155 / 1030
$E_p$ (extra / intra)	[ $\mu$ J]	14 / 68	4.6/15	1.9/15	10 / 66
$P_{pk}$ (extra / intra)	[MW]	39 / 188	18/62	4.8/37	62 / 416
rms intensity noise (1Hz-1MHz)	[%]	<1	<1	<1	<0.5
$M_{x,y}^2$		1.1	-	-	1.1
$\phi_{nl}$ (estimated)		$0.46\pi$	$>0.7\pi$	$>0.2\pi$	$0.61\pi$

**Table 3.3.** – Parameters of the developed KLM oscillators.

It was shown experimentally that power scaling of Kerr-lens mode-locked oscillators is a natural continuation to the precept of increased mode-sizes in a thin disk gain medium. The geometrical power scaling applied to KLM allows the generation of pulses with 39 MW peak power under normal atmospheric conditions and still exploit a large fraction of the available gain bandwidth from Yb:YAG. Further increasing the mode size in the Kerr-medium under reduced air pressure confirmed a near linear geometrical scaling of the peak power up to 62 MW with near gain bandwidth limited pulse duration of 140 fs. This combination of ultrashort pulses and high peak- as well as average power is unattained with any other mode-locking technique, including SESAM.

The identified limitations to average power scaling appear to be of thermal origin. The Kerr-lens material requires careful selection and testing due to large spread in production quality. The observed peak power clamping at low pressure air environment might also be a symptom of increased mirror heating due to decreased convection. The use of mirror substrates with high thermal conductivity should cure this shortcoming.

## 4. Broadband oscillators: the case for Yb:YAG

This chapter briefly describes available gain materials and perspectives for power scaling mode-locked thin-disk oscillators with different, broadband gain materials. An oscillator with the broadband Yb:CaGdAlO<sub>4</sub> is investigated experimentally.

Not insubstantial efforts are being put into finding new gain materials that are suitable for both high power laser operation as well as short pulse generation. A paper in 2009 [134] attempted to identify the most suitable candidates for the use in thin-disk lasers with perspectives of generating sub 100 fs pulses. Today, 2017, it is still unclear whether any of these can be suitable replacements for Yb:YAG. Some of these material that have been mode-locked in the thin-disk geometry are displayed in 4.1. The maximum achieved average power in mode-locked operation as well as the minimum achieved pulse durations are displayed (the values are mostly not achieved simultaneously but originate from different reports). Also the values for thermal conductivity and the (FWHM) emission-bandwidth are written although<sup>1</sup>. The rather long pulses that have been demonstrated for nearly all of these materials are owed to the SESAM used for mode-locking rather than the limited available gain bandwidths. Yb:YAG may serve here as benchmark where SESAM mode-locking typically produces >500 fs long pulses in high-power operation.

The most promising alternative laser hosts are members of the sesquioxides (Lu<sub>2</sub>O<sub>3</sub>, Sc<sub>2</sub>O<sub>3</sub>, Y<sub>2</sub>O<sub>3</sub>, LuScO<sub>3</sub>) since they are isotropic crystals and exhibit good thermal conductivity and hardness, moderate emission cross-sections and slightly larger bandwidth than Yb:YAG. However, they have a melting temperature around 2400 °C [141] which makes them hard to produce in sufficient quality and size and has inhibited widespread use in thin-disk lasers so far<sup>2</sup>. Alternatively, these materials might have a future in ceramic form which is easier to produce in large diameters than single crystals [142, 143]. An impressive average power output of 141 W has been obtained from an Yb:Lu<sub>2</sub>O<sub>3</sub> mode-locked oscillator, however not with a significant advantage in bandwidth [34].

The tungstates (KLuW, KYW) have been shown to mode-lock with moderate output power >20 W [36, 41], however, anisotropy and also their rather low thermal conductivity makes them unlikely candidates for operation at higher power.

---

<sup>1</sup>For some of the very broadband material it is very hard to give an accurate number for the emission bandwidth due to strong changes in the spectrum at slightly differing values of the inversion

<sup>2</sup>Some of the authors early experiments involved mode-locking an Yb:Lu<sub>2</sub>O<sub>3</sub> thin disk oscillator. The results were far below expectation and experiments eventually aborted due to low disk quality.

material	$\sigma_{el}$ [ $10^{-20} \text{ cm}^2$ ]	$\kappa_{th}$ [ $W/mK$ ]	$\Delta\lambda_{em}$ [ $nm$ ]	FTL [ $fs$ ]	min. ML $T_{fwhm}$ [fs]	max. ML $P_{avg}$ [W]
Yb:YAG	1.89	11	8[135]	140	49*[30]	275[27]
Yb:CALGO	0.75	6.6	-	-	62[136]	28[43]
Yb:Lu <sub>2</sub> O <sub>3</sub>	1.26	12.8	13[137]	87	329[33]	141[34]
Yb:Sc <sub>2</sub> O <sub>3</sub>	1.44	18	12[137]	95	103**[138]	8.6**[138]
Yb:Y <sub>2</sub> O <sub>3</sub>	0.92	13.4	14[137]	80	547***[139]	7.4***[139]
Yb:LuScO <sub>3</sub>	0.89	3.9	22[137]	52	96[40]	23[39]
Yb:KYW	3	-	16[135]	69	240[36]	22[36]
Yb:KLuW	2.5	3.3	25[135]	45	440[41]	25.6[41]
Yb:YCOB	0.45	2	-	-	270[140]	4.7[140]
Yb:CaF <sub>2</sub>	0.16[135]	-	-	-	445[47]	6.6[47]

**Table 4.1.** – Gain materials and important laser properties from mode-locked thin-disk oscillators.  $\sigma_{el}$ : laser emission cross-section,  $\kappa_{th}$ : thermal conductivity,  $\Delta\lambda_{em}$ : emission-bandwidth, FTL: Fourier transform limit, min. ML  $T_{fwhm}$ : minimum achieved pulse-duration in experiment, max. ML  $P_{avg}$ : maximum achieved average power output in experiment. \*Distributed KLM. \*\*Mode-locked with dual-gain laser. \*\*\*Ceramic. Data are from [134] unless marked otherwise.

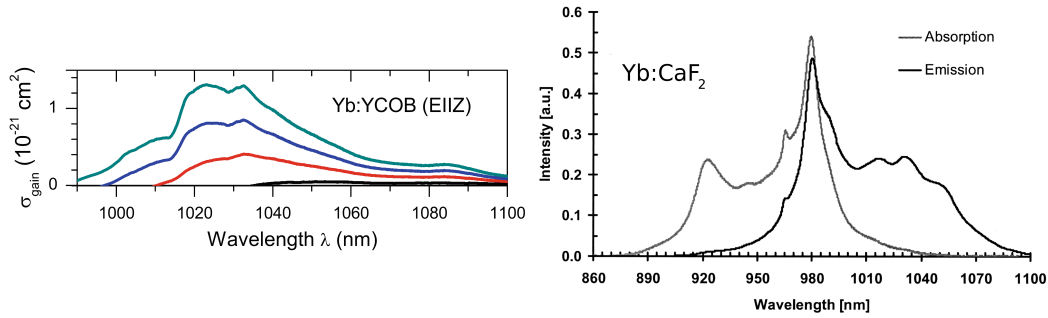


**Figure 4.1.** – Gain and emission cross-sections. (left): Yb:YCOB. The gain cross-section is plotted for the inversion levels  $\beta=0.05, 0.15, 0.25$  and  $0.3$  (bottom to top). Figure adapted from [134] (right): Yb:CaF<sub>2</sub>, absorption and emission cross-section. Figure adapted from [144].

Both Yb:CaF<sub>2</sub> and Yb:YCOB have a large bandwidth (figure 4.1) that should support sub 30 fs pulses. However, the low gain seems to hamper high-power operation. Yb:CALGO has recently received quite some attention due to its very wide emission bandwidth and yet large thermal conductivity [145]. The shortest SESAM mode-locked pulses from a thin-disk have been generated with this material [136], however at low average power. The gain is very low which seems to make it unsuitable for high output coupling in thin disk lasers. An own, failed attempt at Kerr-lens mode-locking this material in the thin-disk configuration is described in section §4.1.

## 4.1. Yb:CaGdAlO<sub>4</sub> oscillator

The high thermal conductivity and simultaneous broad emission bandwidth of Yb:CaGdAlO<sub>4</sub> (Yb:CALGO) have sparked the hope of high-power, SESAM-mode-locked thin-disk oscillators with pulse durations below 100 fs [146]. Such an oscillator has been realized, however, with low output power (5.1 W - 62 fs, [136]) that makes it difficult to justify the more complex and expensive thin-disk geometry (12.5 W - 94 fs were generated from an Yb:CALGO bulk-oscillator in [44]). Transferring this gain material into a KLM thin-disk oscillator seems a reasonable approach to reaching substantially shorter pulses and possibly higher output power than with SESAM mode-locking [147].

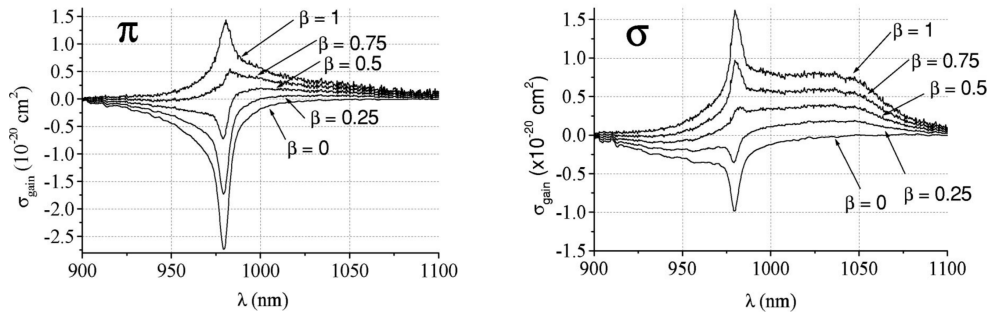


**Figure 4.2.** – Emission spectra of Yb:CALGO for different inversion levels  $\beta$  and polarization directions from [145]

### 4.1.1. Disk testing and single-mode cavity

In the following experiment such a KLM oscillator was built, using a 5 % Yb-doped, 200  $\mu\text{m}$  thick CALGO disk that was bonded to a diamond heat-sink. The crystal was c-cut to avoid polarization-issues and stress/depolarization from differing thermal expansion coefficients, since CALGO is a uniaxial crystal. The Yb:CALGO thin-disk was pumped via fiber-coupled, VBG-stabilized laser diodes, lasing at 976 nm. Even though this wavelength is not optimal for pumping Yb:CALGO these diodes were already available in the lab from a previous laser experiment. As for any new thin-disk but especially this previously untried gain-material initial testing of the disk quality was crucial in determining safe operation-parameters. The disk was

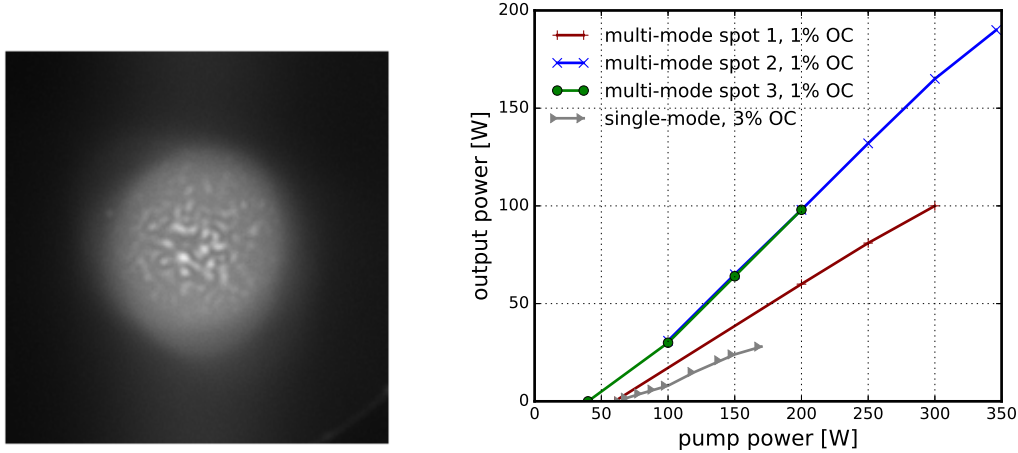


**Figure 4.3.** – (left) CCD-image of pump-irradiated Yb:CALGO thin-disk with speckle structures. (right) CW output in multi-mode and single-mode operation.

tested in a simple multi-mode cavity consisting of the disk and one concave mirror with 1 % output coupler transmission. The pump-spot was adjusted for  $\sim 2.5$  mm diameter. After short-pass filtering the crystal revealed several scattering centers as well as speckle structures on a CCD-camera when pumped (figure 4.3). Also the CW-multi-mode optical-to-optical efficiency changed when moving the pump-spot to different positions on the disk which indicates some crystal inhomogeneity. Despite the poor quality the multi-mode laser showed acceptable performance with 60 % slope- and 50 % optical-optical-efficiency even up to  $7 \text{ kW/cm}^2$  incident pump irradiation, similar to [146].

Single-mode operation was realized in a linear X-shaped cavity as depicted in figure 4.4 with a repetition rate of 50 MHz and 2 reflections on the thin-disk per round-trip. The radii of curvature of the focusing mirrors F1, F2 with 300 mm were chosen relatively short in expectation of low output power in the mode-locked regime. In CW single-mode up to 28 W output power were generated at 190 W pump power and 3 % output coupler transmission. Additional losses introduced by the HD mirrors with  $-1000 \text{ fs}^2$  GDD each and also the Kerr-medium under Brewster's angle, consisting of fused silica, reduced the efficiency and output power only slightly. The polarization was selected by rotating the Brewster-plate around the beam-axis and showed little influence on the output-power, verifying the c-cut disk.

Unfortunately the Yb:CALGO disk exhibited significant thermal lensing, noticeable in runaway of the output power and switching to higher-order modes, especially when approaching the stability-edges. Although such behavior can also occur with Yb:YAG the behavior was pronounced with CALGO. Insertion of a hard-aperture with 3.7 mm diameter helped cleaning the mode and made reaching 28 W output power in the single-mode regime possible.

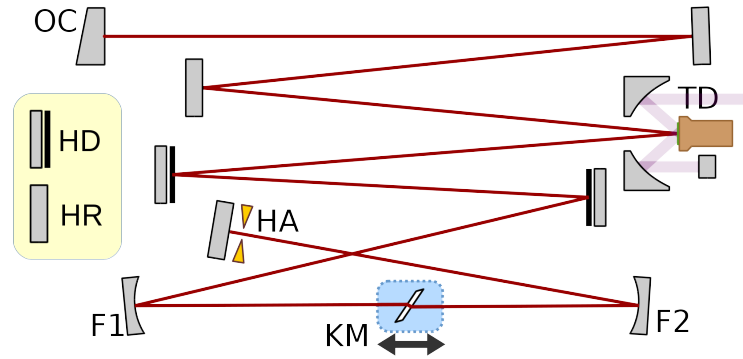


**Figure 4.4.** – 40 MHz Yb:CALGO oscillator setup. OC: output-coupler, HD: highly-dispersive mirror, HR: highly reflective mirror, HA: hard aperture, KM: Kerr-medium, TD: thin-disk, F1,F2: spherical focusing mirrors.

#### 4.1.2. Mode-locking starting issues

Attempts to start mode-locking in the usual manner proved unfruitful. Pushing the cavity-mirrors induced measurable noise, however, the perturbations were not sufficient to initiate pulse-buildup. Changing the intra-cavity GDD ( $-20,000 \text{ fs}^2$  to  $-6000 \text{ fs}^2$ ) or the Kerr-medium thickness also did not allow pulse-buildup which is in stark contrast to the Yb:YAG TD-oscillators that can be mode-locked fairly easily even at strongly differing GDD levels or with a wide range of KM-thicknesses.

A possible cause for the mode-locking starting problems might lie in the inhomogeneous broadening in Yb:CALGO as opposed to the homogeneous broadening in Yb:YAG. This was identified a limiting factor in [148, 149] where mode-locking of Nd:glass oscillators was considered. There the much quicker decay of modes in the oscillator with inhomogeneously broadened gain prohibited self-starting or even mode-locking altogether. The inhomogeneously broadened laser could be mode-locked when the bandwidth was artificially reduced with an etalon. The built Yb:CALGO oscillator was possibly suffering from the same issue, however, an artificial shrinking of the gain-bandwidth to enable pulse-formation would reduce the broadband mode-locking-efforts to absurdity.

In order to accelerate the pulse-buildup-rate it was tried to increase the pulse-modulation-strength. Seeing as an Yb:CALGO oscillator had been mode-locked already using SESAM, the speed of pulse-buildup was thought to improve by additionally implementing SESAM into the oscillator. However, a weak SESAM (grown by BATOP GmbH) with modulation-depth of 0.1 % did not show any effect on the buildup-process. SESAM with higher modulation depth of 0.5 - 1.0 % and 0.5 - 1.0 % non-saturable losses respectively, were damaged and any further attempts involving SESAM were ceased.

After increasing the Kerr-medium thickness from 1 mm to 6.4 mm fused silica and decreasing the ROC of mirrors F1, F2 to 150 mm the photo-diode signal of a pulse-train was visible on the oscilloscope. However, the pulses did never reach steady state and died off quickly after perturbing the oscillator manually. The optical

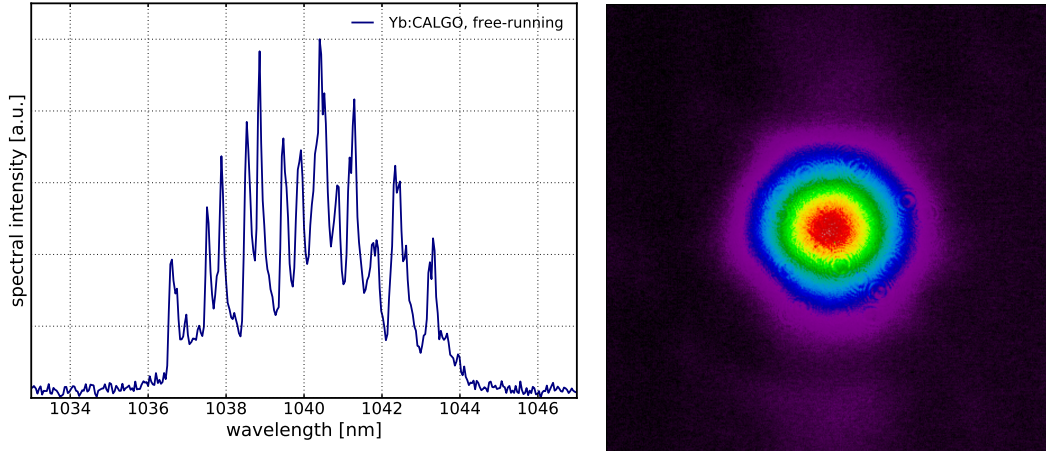


**Figure 4.5.** – (left) Broad output-spectrum of the free-running Yb:CALGO oscillator during mode-locking attempts. The spectrum is averaged over 0.5 s and catches the many, simultaneously fluctuating modes. (right) Single-mode CW output beam-profile with 28 W average power.

spectrum recorded during these mode-locking attempts was highly dynamic, showing not a single, stable line but many, fluctuating simultaneously as shown in figure 4.5.

It is currently unclear why KLM in the thin-disk geometry was not possible. It may be partially attributed to insufficient crystal quality paired with the low gain of the crystal. The inhomogeneous broadening currently appears as an obstacle, however, seeing as KLM-operation has been realized in a bulk-oscillator [147], this property can not pose an intrinsic problem but should serve as a challenge for further studies. The experiments are not conclusive but should be continued with enhanced gain from multiple beam-folding over the thin-disk to enable quicker pulse-buildup.

## 4.2. Distributed Kerr-lens mode-locking

The often cited escape route from sub-optimal pulse durations in SESAM mode-locked oscillators is the call for more broadband gain-media [134, 40, 150, 137], however, the bandwidth of mode-locked pulses is not limited to the FWHM amplification bandwidth of the gain medium but can exceed it<sup>3</sup>. The strong SPM due to the Kerr nonlinearity in Ti:Sa KLM oscillators allowed record pulse durations with sub-2 optical cycles, approaching the gain bandwidth e.g. in [151, 152, 153]. A concept named *distributed Kerr-lens mode-locking* (DKLM) was explored within the author’s research-group that allowed stabilization of 49 fs short soliton-pulses in spite of high nonlinear phase-shifts with an Yb:YAG thin-disk oscillator [30]. DKLM relies on the placement of additional Kerr-media inside the oscillator (see figure 4.6) such that the SAM is increased to support larger SPM and thus a strongly increased spectral bandwidth and shorter pulses. A drawback of this technique is the partly

<sup>3</sup>The FWHM is not always a suitable measure for specifying the total bandwidth of a material. For very short pulses the spectral structure can become quite complex.

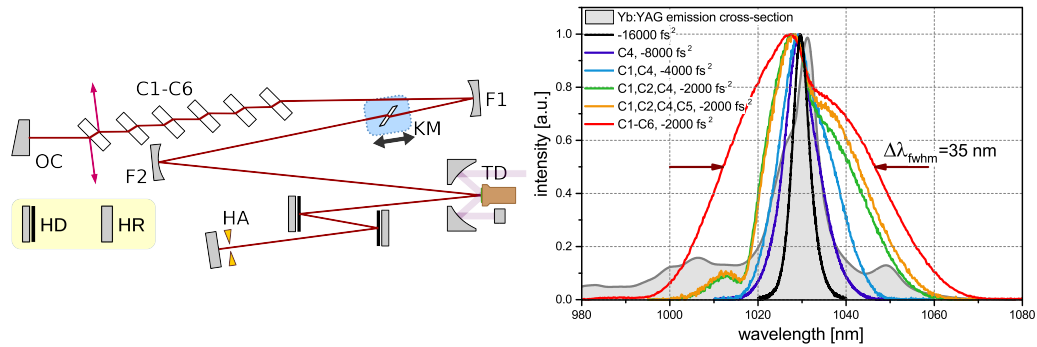


**Figure 4.6.** – (left): Sketch of the DKLM oscillator with the additional crystals C1-C6 placed in the beam-path. The arrows originating from one of the crystals illustrate the additional cavity loss under Brewster's angle due to depolarization. OC: output-coupler, HD: highly-dispersive mirror, HR: highly reflective mirror, HA: hard aperture, KM: Kerr-medium, TD: thin-disk, F1,F2: spherical focusing mirrors. (right): Spectral bandwidth of the output-pulses for different crystals and values of the intra-cavity GDD. The broadest spectrum exceeds the FWHM emission bandwidth of the utilized gain material Yb:YAG (grey background).

unavoidable decrease in opt.-opt. efficiency with values approaching 3.5 % for the shortest pulses. However, in comparison a SESAM-mode-locked 62-fs-oscillator<sup>4</sup> using the much more broadband Yb:CALGO [136] (see figure 4.2) did not offer a significant advantage in opt.-opt. efficiency or average power output (62 fs, 7 %, 5.1\_W) over the DKLM laser using Yb:YAG (49 fs, 3.5 %, 3.5 W).

### 4.3. Summary

The data and results presented in this chapter make a point in showing the difficulty of ultrashort-pulse, high-power oscillator development. Many materials that appear promising for short pulse generation either exhibit low gain or fall short of the strict requirements for thin-disk manufacturing. The failure to mode-lock an Yb:CALGO TD-oscillator with the KLM technique is rather puzzling and symptomatic of thin-disk oscillator development with new and unknown materials.

Instead of struggling with the poor crystal quality from hard to develop materials the current state of the art in KLM thin-disk lasers already allows for reaching close to 100 fs pulses from Yb:YAG. In combination with power-scalable, easy to handle and efficient nonlinear spectral broadening techniques as explored in chapter 5 the few-cycle regime may be accessed regardless, however, at much higher peak-power than is currently imaginable with Yb:CALGO or any other of the broadband but low gain materials. Additionally the DKLM-approach makes Yb:YAG highly competitive with regard to direct, sub-100-fs oscillator output and may allow better power-scalability due to demonstrated superior power-handling in Yb:YAG. Of course contentment is the stop of progress and further efforts in the development of new

<sup>4</sup>To the best of my knowledge the shortest-pulse SESAM mode-locked thin-disk oscillator.

laser-materials are crucial for pushing towards new applications, however, the stakes have been set high by Yb:YAG and it may take considerable effort to finding and developing a material that supersedes it for high-power short-pulse generation.

## 5. Scalable pulse-compression techniques

Even if previously mentioned broadband gain materials were available in sufficient quality for high-power laser operation, the obtainable pulse durations would still remain well above the few-cycle regime<sup>1</sup>. This calls for extra-cavity pulse compression to widen the scope of possible applications for the developed laser source. The ideal compression technique should exhibit

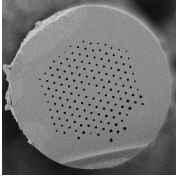
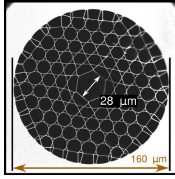
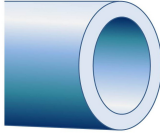
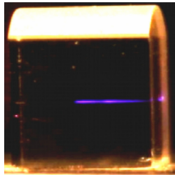
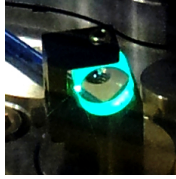
- **power scalability.** An intrinsic limitation to pulse propagation in nonlinear media is given by the critical power for self-focusing  $P_{crit}$ . An optical pulse with instantaneous power greater than  $P_{crit}$  is bound to experience beam-collapse, leading to damage in the medium. This is even independent of the input intensity. Another aspect is the average power scalability. While a certain method might work well with highly energetic pulses and low repetition rates the picture can change when high repetition rates and high average power are involved.
- **high throughput efficiency.**
- **low noise.** Spectral broadening due to self-phase modulation is a third order effect of the electric field and intensity-noise in the input-field is therefore enhanced. This requires a stable light source to begin with in order to keep the resulting intensity fluctuations as well as spectral breathing under control.
- **insensitivity to alignment.** If the desired target parameters can only be reached by compression in several stages, insensitivity to alignment becomes a key feature. Even in systems of low complexity robustness in alignment is welcome.
- **low complexity.** While a specific method can combine most of the favorable attributes mentioned before, it's implementation might be hindered by a steep growth of system complexity and footprint.
- **low cost.**

Pulse compression techniques essentially rely on spectral broadening in a nonlinear medium and consecutive temporal compression with a dispersive element<sup>2</sup>. These typically include prisms, gratings, chirped mirrors or bulk material. Whenever

---

<sup>1</sup>At 1  $\mu\text{m}$  central wavelength a single oscillation lasts only 3.3 fs.

<sup>2</sup>Pulse shortening can also be obtained by some type of temporal filtering as e.g. in XPW (cross-polarized wave generation, [154, 155]) which, however, is extremely lossy. It is mainly used to enhance the temporal contrast in high energy amplifier systems [156].

solid core (PCF)	hollow core PCF	capillaries	bulk filamentation	bulk
				
$P_{pk} < P_{cr}$ (4 MW)	$1 \text{ MW} < P_{pk} < X \text{ GW}$	$P_{pk} > 1 \text{ GW}$	$P_{pk} > X \text{ MW}$	$1 \text{ MW} < P_{pk}$
limited stability for high avg. power	limited by ionization		low avg. power	upper limit given by lab-size

**Table 5.1.** – Spectral broadening techniques and corresponding typical peak-power ranges. Image sources: soli-core (PCF): [157], hollow-core PCF: [158], bulk filamentation: [159].

possible, preference should be given to chirped mirrors due to their flexible design, compactness, tolerance to thermal effects and high throughput efficiency.

A quick overview of the typical peak-power ranges for several spectral-broadening schemes is given in table 5.1.

The confinement of the laser-field to a small area in solid- or hollow-core photonic crystal fibers (PCF) yields strong broadening via self-phase-modulation. In some cases a tailored fiber dispersion can result in self-compression, to some degree making even the temporal post-compression step unnecessary [160, 161, 162]. The relatively low system-complexity has therefore given fiber based compression techniques their dominant position in the field. However, the glass in solid-core fibers puts an approximate upper limit to the input peak-power of the pulses with  $P_{crit}$  being near 4 MW. This limit can be extended slightly by the use of circularly polarized light but not much beyond [163]. Chirped pulse compression, analogous to chirped pulse amplification can be used to circumvent this peak-power limit [164, 165]. Large average power compression with 250 W output and fiber-input peak-powers just below the damage threshold has been reported in [51]. Yet, average power scaling in solid-core PCF has proven problematic. For example the LMA (large-mode-area) PCF in the setup of [22] had to be replaced frequently due to degradation. The high sensitivity to alignment of the fiber-coupling is then especially time-consuming and renders this technique unattractive for daily operation.

Unlike in solid-core PCF, the nonlinear medium in hollow-core PCF (e.g. Kagomé, table 5.1) is a gas [166, 167]. Unless the ionization-threshold is reached a highly intense laser pulse can propagate without causing detrimental beam-collapse. The approach is therefor peak-power scalable up to several gigawatt input power<sup>3</sup>. The nonlinearity of the utilized noble-gases is typically 3 orders of magnitude lower than in solids. Therefore, depending on the input power and energy, the fibers need to be relatively long and the gas pressure has to be adjusted typically within the range of

<sup>3</sup>Noble-gas tunnel-ionization sets in around  $10^{14} \text{ W/cm}^2$  intensity.

a few to few tens of bar to achieve the desired broadening. Using static gas pressure the input-profile becomes intensity-dependent and complicates efficient coupling into the fiber [168]. For high average power thermally induced gas-pressure fluctuations can additionally reduce coupling efficiency [158]. A solution is differential pumping with vacuum at the input facet and an increasing pressure gradient towards the output side of the fiber. Sub 10 fs pulses with 18 W average power were generated in a 2 step compression with a KLM Yb:YAG thin-disk oscillator [169]. However, the approach still remains highly sensitive to alignment and the output noise is increased drastically compared to the initial oscillator noise [169, 170]. Prolonged exposure to high average power input also showed structural damage of the Kagomé fiber, further degrading the noise-performance [158]. Degradation was not reported in a setup with larger core-diameter and higher average power [171]. Even though the intensities are kept below the single-shot ionization-threshold for the used gases there are indicators of possible plasma-buildup due to the high repetition-rate [158, 170].

Spectral broadening in gas-filled hollow capillaries (table 5.1) is practiced for pulses from amplifier systems [52, 172, 53] and was recently reported to be scaled up to several hundred of watt [53]. These capillaries have a very large inner diameter and a very lossy mode more akin to total internal reflection rather than a guided single-mode. The limited peak-power from oscillators demands a small interaction area with the weakly nonlinear (pressurized) gas to achieve mentionable spectral broadening, however, for relatively small core diameters  $<100\ \mu\text{m}$  in these capillaries the losses become very large [158, 173]. Therefore this approach is limited to pulses with typically  $>1\ \text{GW}$  peak-power. Generation of self-guided filaments in gas can also be used for spectral broadening, yet the requirement on the initial peak-power are even more strict [174, 175]. White light generation via filamentation in bulk can yield super-broadband spectra [176, 159], however, the approach is not average power scalable and limited to the few Watt level (table 5.1).

Already in 1988 substantial spectral broadening by focusing into bulk material was reported on in [177]. Critical self-focusing could be avoided by choosing the material length and input beam parameters such that the self-focusing length was longer than the material thickness. Due to the relatively low efficiency from beam inhomogeneity the approach was not much pursued. A recent demonstration of highly efficient supercontinuum generation in a thin fused silica plate assembly seems to have rekindled interest in this type of spectral broadening [178] for a larger number of research-groups. Within the author's research-group 6 W, 7.7 fs pulses near 15 MW peak-power could be generated in a combined fiber and bulk compressor seeded by a TD KLM oscillator [22]. The main advantages of using bulk materials over hollow waveguides are the insensitivity to beam-pointing and potentially uncritical alignment which leads to low maintenance requirements. The possibly compact setup along with the ready availability of these common optical elements and therefore cheap price are further advantages that should be considered. Unlike in hollow-core fiber based spectral broadening [179, 169] the noise performance of the laser seems to be unaffected by the broadening in bulk [170].

Other than the method demonstrated by [178] different approaches to retaining homogeneous beam-profiles have been devised such as a specially shaped nonlinear

broadening lens [180] or a nonlinear multi-pass cell with high throughput efficiency of  $\sim 90\%$  [181]. The upper peak-power limit for which spectral broadening in bulk is applicable is mainly set by the constraints of the laboratory-size since high pulse-fluences and intensities need to be balanced by growing beam-sizes and correspondingly longer propagation-lengths. For input peak-power lower than 1 MW the use of bulk materials is quite cumbersome since strong focusing is required to observe spectral broadening.

Apart from regular SPM from a material's cubic ( $\chi^{(3)}$ ) susceptibility, nonlinear phase-shifts can also be impressed on a pulse via cascaded, quadratic ( $\chi^{(2)}$ ) interactions, e.g. during phase mismatched second harmonic generation (SHG). By proper choice of phase-(mis)matching angles the strength and sign of the resulting phase-shift can be varied, resulting in enhanced self-focusing or self-defocusing and spectral broadening [182, 56]. This gives new opportunities to avoiding self-focusing damage and even temporal self-compression in normally dispersive bulk material [183].

Other means of generating short, high-power pulses is the use of parametric amplification schemes such as non-collinear optical parametric amplification (NOPA). There a low-power but broadband seed is generated (e.g. by fiber-broadening, filamentation or the direct output from a broadband oscillator) and subsequently amplified via the parametric process by drawing power from a high-energy but longer pump-pulse. Using these techniques, energetic few-cycle pulses can be generated [184, 185, 186, 187], however, at the expense of optical to optical efficiency.

It is clear that bulk broadening shows great potential with respect to average power scalability as well as robustness and noise performance. This chapter explores the utility and efficiency of different bulk spectral broadening schemes with the goal of reaching the few-cycle regime with the relatively high average- as well as peak-power obtained from the previously developed oscillators.

In part 5.1 of this chapter pulse-compression experiments using  $\chi^{(3)}$  materials are described. Part 5.2 is dedicated to broadening aided by cascading  $\chi^{(2)}$  processes.

## 5.1. Spectral broadening in bulk $\chi^{(3)}$ material

As mentioned, the propagation of an intense electromagnetic pulse in a material with cubic nonlinearity<sup>4</sup> gives rise to the optical Kerr-effect. The temporal intensity distribution of the pulse modulates the temporal phase and generates new frequencies at the pulse's leading and falling edge which can afterward be compressed temporally via dispersive optical elements. The energy of the initial pulse at the fundamental carrier frequency is conserved when excluding the usually negligible third harmonic generation. The initially Gaussian spatial intensity profile, however leads to differing temporal intensity-slopes at different positions of the beam. Therefore the part of highest intensity will have experienced the strongest phase-shifts and thus carry a broader spectrum than the surrounding parts. The spatial distribution of the spectral content is inhomogeneous and subsequent compression will result in both spatially and temporally varying widths and is generally undesirable. To obtain a well defined

---

<sup>4</sup>Basically any material.

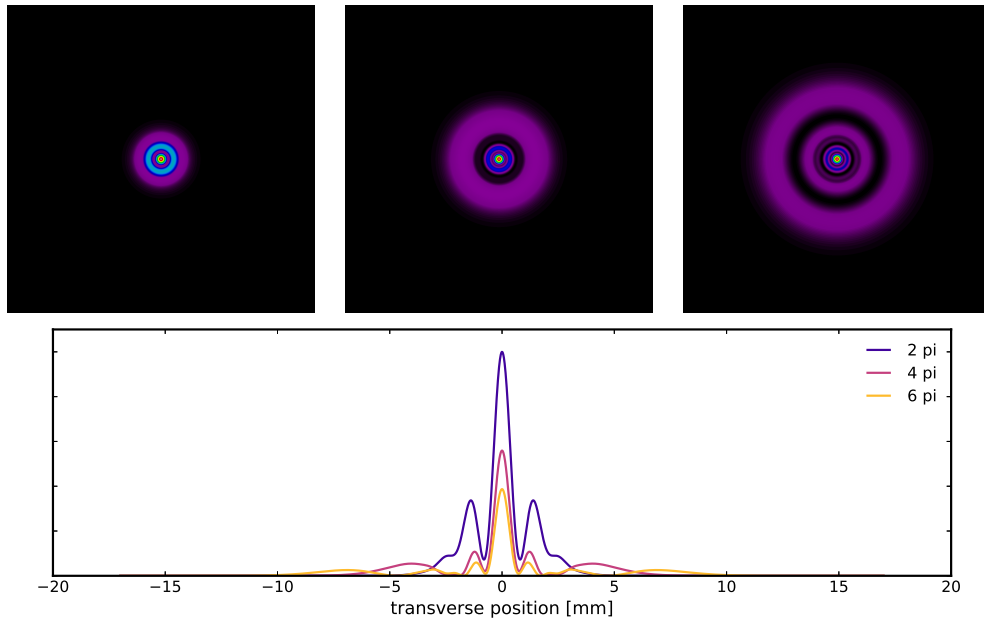


**Figure 5.1.** – Calculated CW diffraction rings resulting from self-focusing with peak nonlinear phase-shifts of  $2\pi$ ,  $4\pi$  and  $6\pi$ . The self-focusing action was due to a thin phase-sheet located one Rayleigh-length apart from the beam-waist ( $w_0=100\ \mu\text{m}$ ) in the direction of the diverging arm. The displayed profiles have propagated for 350 mm. The beams were propagated by solving the Rayleigh-Sommerfeld integral [188] numerically.

pulse it would have to be filtered spatially, resulting in large transmission losses (see [177, 170]). This adverse effect will generally also happen in fiber-based spectral broadening. There, however, the fiber's mode-guiding property ensures a spatial mixing of the spectral content upon propagation and the output is usually spatially quite homogeneous. An approach to overcome this limitation of unguided spectral broadening could be the use of shaped materials such as a concave, defocusing lens. In this case the lower intensity parts of the beam-profile can compensate for the decreased SPM by traveling through the thicker part of the material [180]. However, this approach seems only practical for amplified systems so far, since the lower peak-power from oscillators calls for smaller beam-diameters in the nonlinear medium to achieve efficient spectral broadening ( $\sim 100\ \mu\text{m}$ ) and correspondingly very small structures for compensation.

Independent from the spatially inhomogeneous spectra, self-focusing adds additional aberrations to the beam-profile in the case of strong nonlinear phase-shifts as required for spectral broadening. The source is the shape of the self-imposed spatial phase-profile, which ideally should be parabolic (e.g. as assumed in the thin-lens approximation) but in reality mirrors the Gaussian intensity profile of the pulse. The effect is a distortion of the spatial intensity and the appearance of a number of diffraction-rings. The power radiated/lost into these rings depends on the peak nonlinear phase-shift and can be substantial, leading to a strong reduction in peak-intensity. We will refer to this effect as self-diffraction.

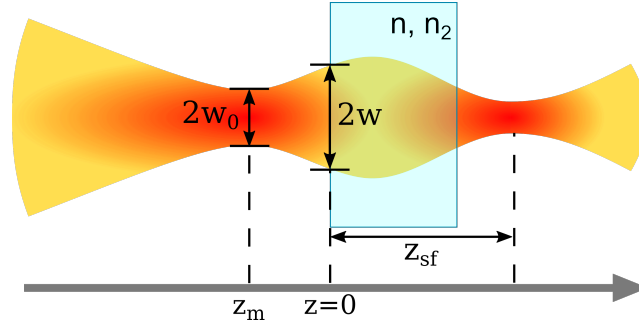


**Figure 5.2.** – Self-focusing geometry.

Figure 5.1 shows the calculated intensity-profiles of an initially Gaussian beam after propagation through a thin medium that introduces a nonlinear phase-shift and consequent self-focusing. It is apparent that the lost power grows quickly with the amount of nonlinear phase introduced.

### 5.1.1. Self-focusing geometry

The distance from input plane to the self-focusing point  $z_{sf}$  is roughly estimated in [189, 63]

$$z_{sf} = \frac{kw^2}{2} \frac{1}{\sqrt{\frac{P}{P_{cr}} - 1 + 2\frac{z_m}{kw_0^2}}} \quad (5.1)$$

where  $P$  is the pulse's peak power,  $P_{cr}$  is the material dependent critical self-focusing power,  $k$  is the wavenumber in the material,  $w$  is the beam-radius at the input plane,  $w_0$  the beam-radius in the focus before the medium and  $z_m$  the distance of the input plane to the initial beam-waist (see figure 5.2). Alternatively the formula can also be cast into the form

$$z_{sf} = \frac{kw^2}{2} \frac{1}{\sqrt{\frac{P}{P_{cr}} - 1 - \Theta}} \quad (5.2)$$

with the initial beam-divergence  $\Theta$ . As intuition suggests,  $z_{sf}$  increases when the bulk medium is placed after the focus (negative value of  $z_m$ ) and stronger divergence of the input beam that has to be overcome by the nonlinear lensing before focusing can occur. Therefore, by selecting the right focusing geometry, catastrophic beam-collapse within the medium should be suppressible and allow better power scalability than fibers

### 5.1.2. Materials for high power spectral broadening

Materials that qualify for spectral broadening need to be available in good optical quality and exhibit low intrinsic absorption. Table 5.2 lists some of the materials

material	broadening	damage threshold	comments
SiO <sub>2</sub> (glass)	o	o	
SiO <sub>2</sub> (cryst.)	o	+ +	Birefringent
SF10	+	-	Thermal lens
CaF <sub>2</sub>	-	+	
ZnS	+	- -	Degrades quickly
Al <sub>2</sub> O <sub>3</sub>	o	+	Explodes on damage. Birefringent
TGG	+ +	o	Strong dispersion. Thermal lens
YAG	o	o	

**Table 5.2.** – Subjective rating of material properties with respect to high power spectral broadening.

used in the further described single focus experiments and a subjective rating of their respective suitability for pulse-compression.

It appears that a high thermal conductivity is also important to avoid damage under high average power irradiation. This is particularly obvious for the case of SiO<sub>2</sub> both in crystalline (quartz) and in glass form (fused silica). When focusing high power into fused silica plates, damage was observed usually with an up to few seconds delay after the final power was set. When exchanging with a quartz plate the damage threshold was increased and in the case of damage it occurred near instantly. Since both materials are quite similar, except for the birefringence and thermal conductivity, one could deduce that an important damage mechanism is of thermal nature and should be less pronounced in high thermal-conductivity materials. On the other hand, sapphire, with its high thermal conductivity performing well as Kerr-medium in the oscillator, proved problematic when optically induced damage occurred. While e.g. glass plates could be reused in a different spot after being damaged (just by rotating the plate) the damaged spots in sapphire started to strongly absorb leading to large scale ablation, spraying of debris and multiple fracturing of the entire crystal within seconds after the initial damage occurred<sup>5</sup>.

Other materials, including TGG (used in Faraday rotators), ZnS or flint glasses like SF10 started exhibiting strong thermal lenses in addition to the nonlinear distortion, making the output fairly unusable. The materials found most suitable for the task were sapphire and crystalline quartz.

### 5.1.3. Single window broadening

First attempts to broaden the oscillator spectrum were made using a single sapphire crystal under relatively tight focusing conditions. At the time these experiments took place the oscillator was configured to deliver 230 fs pulses with up to 160 W average power and 8  $\mu$ J pulse energy. The output beam was focused to an approximately 10  $\mu$ m waist-radius by use of a spherical lens with 30 mm focal length. A 10 mm thick, uncoated sapphire plate was carefully translated towards the focus for differing

<sup>5</sup>Looked like sparkler fireworks. Extremely disruptive for further experiments since all optics nearby needed to be cleaned or sometimes exchanged after such an event.

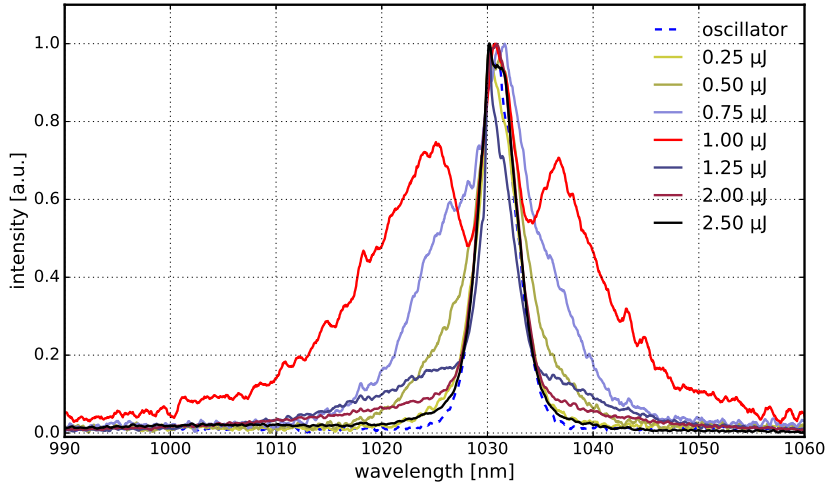


**Figure 5.3.** – Integrated output spectra for different pulse energies focused into a 10 mm thick sapphire crystal. The red side is attenuated and the spectra appear asymmetric due to the nonlinear response of the spectrometer close to the spectral detection limit.

input power levels (see figure 5.2). At each input power the sapphire position was changed for the strongest spectral broadening just before damage set in. The spatially integrated spectra were recorded by measuring the scattered light from the beam-dump and are plotted in figure 5.3.

It quickly becomes obvious that varying the peak power requires an optimization of the focusing geometry. In the above setup pulses carrying energy below 1  $\mu\text{J}$  were not able to produce damage to the crystal at any position along the beam caustic but also SPM was weak. Near 1  $\mu\text{J}$  energy, self-focusing became noticeable and the obtained bandwidth strongly increased, similar to [170]. Close to the focus the crystal was damaged. Pulse energies beyond 1  $\mu\text{J}$  resulted in lower bandwidth due to damage occurring at the surface of the crystal before significant broadening set in.

In order to avoid this surface damage and keep the intensity high over a longer distance inside the crystal the straightforward solution is to increase the size of the beam-waist by choice of a lens with longer focal length. Changing the focal length to 75 mm ( $\sim 25 \mu\text{m}$  waist radius) allowed sending the whole output of the oscillator through the crystal without damage but yielding a spectrum broadened by a factor of  $\sim 2$ . Longer focal lengths did not significantly improve the measured spectral bandwidth. Since the sapphire crystal was uncoated and placed under normal incidence, reflection losses of about 14 % reduced the transmitted power to 135 W. After temporal compression with 8 reflections on dispersive mirrors with nominal -900  $\text{fs}^2$  GDD, 126 fs long pulses were measured in an intensity autocorrelator, assuming a *sech*<sup>2</sup> envelope (see figure 5.4). A slight pedestal indicates some uncompensated phase leading to a reduction of the resulting peak-power. An estimation of the peak-power reduction would require a complete reconstruction of the pulse’s phase, which can be done with a FROG measurement but was not carried out.

The other obvious source of power loss in the described first broadening stage

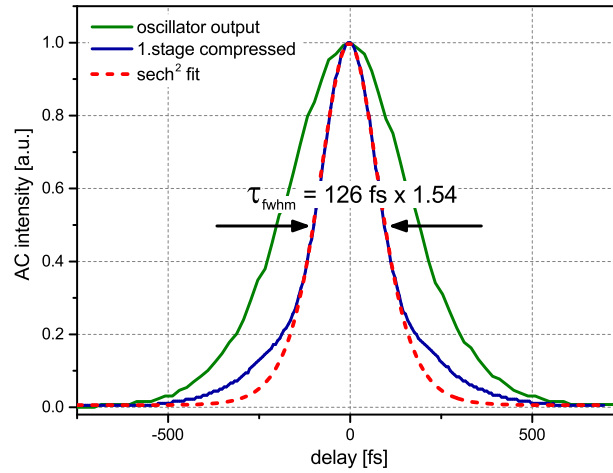


**Figure 5.4.** – Intensity autocorrelator measurement of the pulses before and after the first compression stage. Assuming a  $\text{sech}^2$  pulse envelope the pulse duration is 126 fs long.

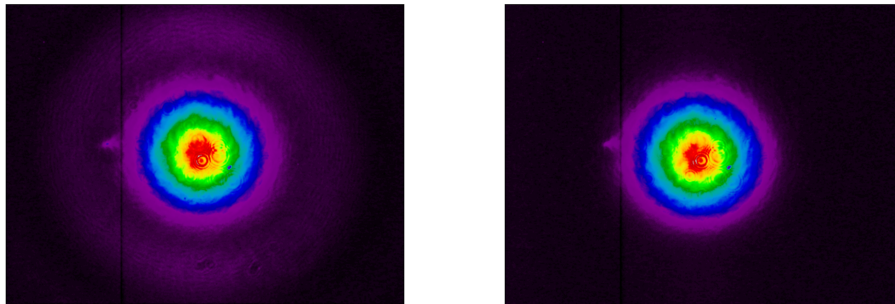


**Figure 5.5.** – Beam-profile of the spectrally broadened pulses (left) before and (right) after spatial filtering.

was clearly visible self-diffraction. A very pronounced ring appeared around the central intensity peak of the beam-profile. The losses due to this self-diffraction were estimated to be around 18 % by spatially filtering the attenuated beam with an iris and comparing the filtered and unfiltered power content (see figure 5.5).

Further spectral broadening could be achieved in a second focusing stage, involving another 10 mm thick sapphire crystal. Assuming a peak-power increase by a factor 2 after the first compression stage the second focusing section was realized with 150 mm focal length where optical surface damage to the uncoated, 10 mm thick sapphire window proved a limiting factor before significant broadening set in. After decreasing the divergence by a factor of 2 with a lens of 300 mm focal length significantly stronger broadening could be observed owing to the self-focusing inside the sapphire (see figure 5.6). The Fourier transform limit (FTL) of said spectrum was estimated to be roughly 70 fs. The strong self-focusing however, produced a larger number of diffraction rings, increasing the self-diffraction losses. Spatial filtering gave an upper bound to the actually usable power-fraction, being at best 60 %. The average power

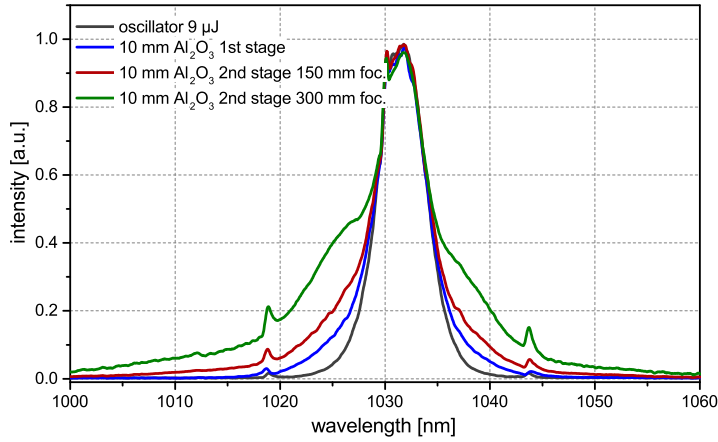


**Figure 5.6.** – Scattered output spectra of the two stage, single crystal pulse compressor. Temporal compression after a first spectral broadening stage yields  $\sim 126$  fs long pulses. Subsequent spectral broadening in another 10 mm thick sapphire crystal is strongest with lower divergence of the input beam. Kelly-sidebands are clearly visible.

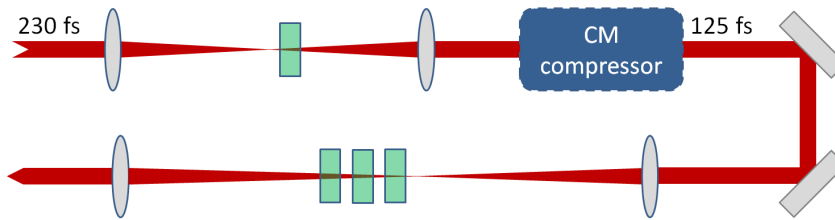


**Figure 5.7.** – Spectral broadening in a sequence of windows. The first stage compresses the oscillator output to 125 fs. The crystals in the second stage are sapphire, quartz and TGG.

transmission through both stages was nearly 71 %, measuring 114 W with the loss again originating from the uncoated crystal surfaces.

The single-window, spectral broadening results are summarized in table 5.3.

### Sequence of windows

Increased spectral bandwidth from a single focusing stage can also be achieved by inserting more bulk windows in sequence. However, maximization of the spectral bandwidth, more particularly, the positioning of each window for strongest, non-destructive self-focusing results also in a corresponding increase of self-diffraction. On the contrary, by distributing the accumulation of nonlinear phase to several, closely spaced windows and avoiding strong self-focusing, one can slightly reduce the influence of self-diffraction. This becomes evident in the following experiment.

After compressing the pulses in a first stage to 125 fs, the output was sent through 10 mm sapphire and additionally a 15 mm quartz crystal and an 18 mm long TGG

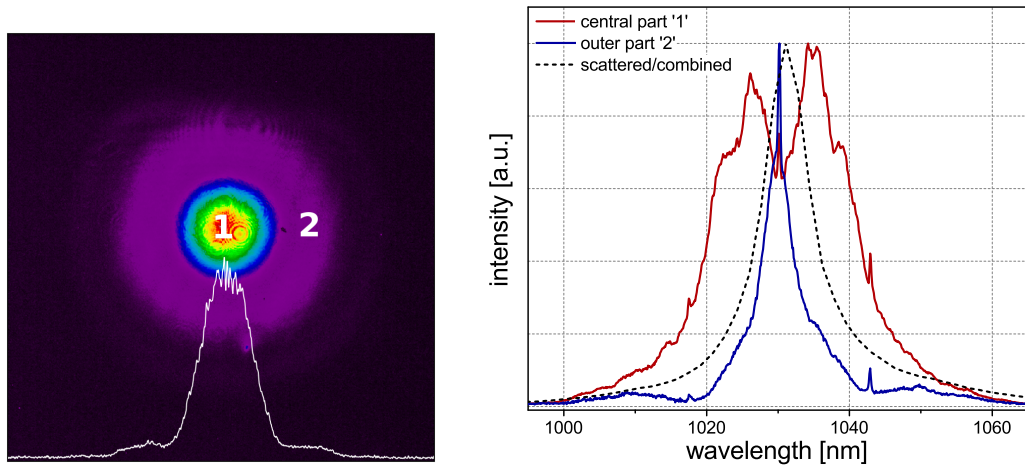


**Figure 5.8.** – Spectral broadening with several windows in a single focus. The output beam-profile (left) is distorted with two clearly visible diffraction-rings. The broadened spectrum (right) is measured in the center -1- and in the outer part -2- of the beam-profile. The spatially integrated spectrum was measured with a different, lower resolution spectrometer.

crystal<sup>6</sup> in that order, after focusing with a lens of 300 mm focal length. Positioning the windows sequentially ensured moderate broadening per crystal while avoiding a strong self-focus. The output spectrum and beam-profile can be seen in figure 5.8. The beam profile exhibits clearly visible self-diffraction rings that were measured by spatial filtering to carry 40 % of the total power. The resulting spectrum was broad enough to support 60 fs pulses. Figure 5.8 also demonstrates the strong differences in spectral content of different parts of the beam-profile. The 'red' spectrum was measured on-axis (with a fiber), while the 'blue' spectrum marks the spectral content of the first diffraction-ring. The spatially integrated, 'dashed' spectrum is of course a superposition. From all 3 spectra nearly the same Fourier transform limit of  $\sim 60$  fs can be computed. In the case of perfect compression with  $\text{sech}^2$  profile and taking into account the losses (Fresnel: 32 %, self-diffraction: 40 %) the upper bound for the peak-power is estimated to be 47 MW. This figure is only 54 % above the initial peak-power from the oscillator and can be strongly increased by applying AR-coatings to the windows, provided they withstand the high peak intensities in the small focal spots. The single-window, spectral broadening results are summarized in table 5.3.

In the case of strong self-focusing the air gap in between the windows allows the beam to diverge before entering the next window, avoiding critical self-focusing and beam-collapse. Inspired by Lu et al. [178] who claimed high throughput efficiency for a sequence of thin glass plates in the weak focus of an amplifier system, Seidel et al. [170] suggested the construction of a nonlinear waveguide, consisting of thin

<sup>6</sup>The AR-coated TGG crystal originated from a decommissioned Faraday rotator due to a large defect in the center. TGG has a quite large nonlinear refractive index of  $n_2 \approx 1.7 \cdot 10^{-19} \text{ m}^2/\text{W}$  and exhibits strong dispersion at 1  $\mu\text{m}$  wavelength.

material	in:	out:	$f_{broad}$	self-diffr. loss	total efficiency	$P_{pk}$
	$\Delta\tau_{fwhm}$	$\Delta\tau_{fwhm}$				
1 <sup>st</sup> stage: 10 mm Al <sub>2</sub> O <sub>3</sub>	230 fs	126 fs	1.8	-	-	-
2 <sup>nd</sup> stage: 10 mm Al <sub>2</sub> O <sub>3</sub>	126 fs	70 fs*	1.8	40 %	43 %	43 MW*
2 <sup>nd</sup> stage: 10 mm Al <sub>2</sub> O <sub>3</sub> +15 mm SiO <sub>2</sub> +18 mm TGG	125 fs	60 fs*	2.1	40 %	40 %	47 MW*

**Table 5.3.** – Single-window compression results.  $f_{broad}$  is the spectral broadening factor deduced from the FTL. (\*) pulse-width estimated from FTL.

windows, separated by small air-gaps. The initial divergence, air-gaps and window thicknesses were chosen such that the beam approximately retained its diameter and thus intensity from window to window. Simulations showed the possibility of spatial-spectral homogenization of the output beam and therefore better overall efficiency of the broadening setup as compared to broadening in a single bulk window. For the available peak-power from the oscillator such a stacked-window waveguide, however, requires extremely thin windows with very precise alignment of the gaps due to the required small focal spot-size and Rayleigh length. Said path was not pursued in this work<sup>7</sup>.

### Back-reflections

High back-reflected power to the oscillator proves somewhat problematic for the laser stability. If the power is strong enough, the back-coupled pulses to the oscillator will interfere with the intracavity pulse and eventually force it into CW operation. Unfortunately, Faraday isolators are a poor choice for high average power laser beams as they are usually subject to not insignificant thermal lensing with very bad consequences for the transmitted wavefront of the beam. Under the full average power load of the oscillator output,  $\sim 200$  W, a Faraday rotator with an 18 mm long TGG crystal visibly distorted the beam-profile and was consequently removed from the setup. In order to prevent the oscillator from dropping out of mode-lock the crystal surfaces therefore had to be tilted away from normal incidence of the optical axis. Thus the reflected beam could be sufficiently separated from the incoming to preserve stable operation. Additionally to eliminating the transmission losses through the broadening stages, an AR-coating applied to the bulk windows would thus also benefit the oscillator reliability.

<sup>7</sup>Initial experiments on thin (several 100  $\mu\text{m}$  thick) glass-windows to reproduce the efficiencies claimed in [178] were hindered by thermal destruction of the plates.

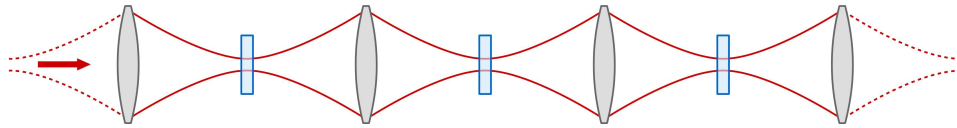


**Figure 5.9.** – Sketch of a lens- or waveguide for nonlinear spectral broadening. The blue blocks represent material-windows.

#### 5.1.4. Nonlinear quasi-waveguide broadening

The field-confinement in fibers not only suppresses the self-diffraction due to self-focusing but the spatially distributed spectral components are mixed to produce homogeneous output [64, ch. 6]. To overcome the problems experienced in single crystal broadening it seems reasonable to attempt and emulate such a wave-guiding behavior for bulk materials. This can be accomplished by periodically propagating a pulse through a nonlinear material and a stretch of free-space in which the mode is shaped via diffractive elements such as lenses or curved mirrors (see 5.9). This type of nonlinear lens- or quasi waveguide is referred to as 'waveguide' in this thesis.

Use of such waveguides has been made in the past to spectrally broaden the pulses in regenerative amplifiers [190]<sup>8</sup>. Also Milosevic et al. [191] in 2000 suggested the use of multiple stages of focusing into long pieces of bulk material with low nonlinear phase-shifts and low peak-power to retain good beam-quality. However, their analysis relying on coupled mode-theory obviously led to the wrong conclusion for pulses with high peak-power and short bulk-windows. In order to retain a Gaussian intensity-profile and avoid losses to self-diffraction the nonlinear phase-shift accumulated each propagation-step needs to stay much lower than in the single-crystal diffraction experiments. Reference [192] suggests an even stricter guideline in which the effect of self-focusing in the waveguide is to be avoided altogether and the peak nonlinear phase-shifts stay  $\leq \pi/10$ . Such a waveguide has been realized as Herriott-type multi-pass cell implementing 38 passes through the mirror-substrates that served as nonlinear medium [181]. The 850 fs long pulses traveled through 1 m of fused silica, leaving nearly no impression on the  $M^2$  beam-quality factor, and could then be compressed to 170 fs. This approach of maximizing the number of waveguide-passes therefore seems well suited for relatively narrow-band pulses, where dispersion is negligible and coatings can be produced with very high transmission or reflectivity over the whole bandwidth<sup>9</sup>.

For pulses shorter than 30 fs the effect of second- or higher-order dispersion from the bulk material becomes more pronounced and greater care must be taken in coating design. Therefore it might be advantageous to increase the accumulated peak nonlinear phase per waveguide-pass to retain good temporal compressibility without the need for specially tailored dispersive mirrors to compensate irregularities of the

<sup>8</sup>A *waveguide* in the sense of a mode propagating inside the stable amplifier-cavity for the time the optical switch was on/off

<sup>9</sup>Coating transmission/reflectivity is critical for such large number of passes and values  $\geq 99.9\%$  should to be achieved in order to retain small losses.

temporal phase. Naturally this involves waveguide-design that takes self-focusing into account.

#### 5.1.4.1. Waveguide design principles

To design such a waveguide the desired peak nonlinear phase dictates the mode-size in the nonlinear material. This fundamental cavity-mode size can be reached for a variety of configurations that are characterized by the Gouy-phase  $\phi_G$  over their stability-region. In a stable cavity the nonlinear phase-profile can be seen as a perturbation of the fundamental mode, coupling power to modes of higher order [193]. If the cavity phase-shift is resonant with a higher-order mode then the coupling is enhanced, which is to be avoided. The condition for resonant coupling to higher order  $\text{TEM}_{m,n}$  modes is met when  $(m+n)\phi_G = k2\pi$  where  $k$ ,  $m$  and  $n$  are integers. If the mode travels only a very limited number of times through the cavity then it is arguable that resonances with large  $k$  also can not contribute significantly to the beam-deterioration. To avoid these most obvious resonances, cavity-configurations with  $\phi_G$  equaling small-integer fractions of  $\pi$  such as  $0$ ,  $1/4$ ,  $1/3$ ,  $1/2$ ,  $2/3$ ,  $3/4$  or  $1$  should be avoided. These especially include the edge of the stability region ( $\phi_G = \pi$ ) where all modes are degenerate and the beam quickly deteriorates. The guideline as worked out in [192] suggests an optimal  $\phi_G$  of  $0.9\pi$  for low nonlinear phases.

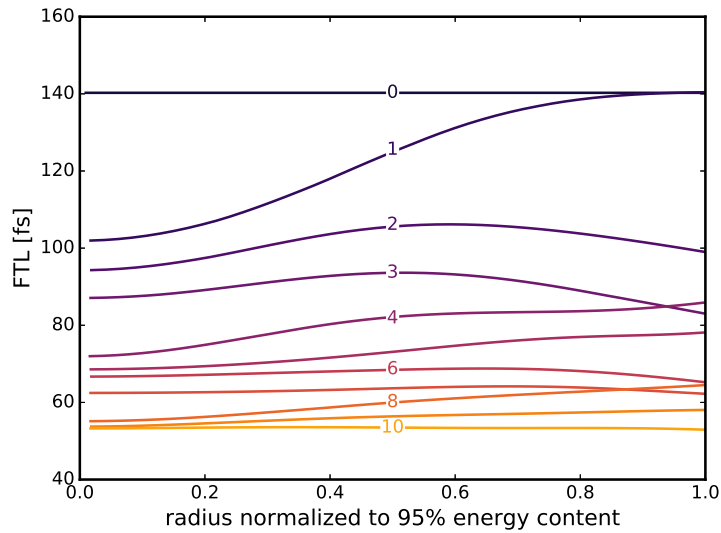
To avoid the bandwidth limitations of AR-coatings<sup>10</sup> on the bulk material windows used for spectral broadening, a n obvious option is to tilt these windows to Brewster's angle. However, self-focusing under Brewster's angle leads to an asymmetric spatial phase-profile since the beam is widened upon refraction in the tilt-plane while traversing the nonlinear window and experiences less self-focusing than in the sagittal plane. The result is an increasing astigmatism and asymmetry in the spatial-spectral distribution.

#### 5.1.4.2. Simulation of the spatial-spectral homogenization

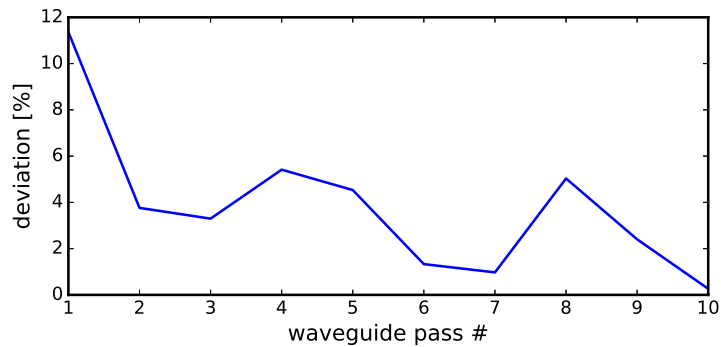
Quick estimates for a pulse's spatial-spectral homogeneity after the waveguide can be obtained by propagating the laser-field computationally. Assuming circular symmetry in space and the only important nonlinear effects are SPM and self-focusing, these simulations can be carried out quite efficiently on a modern PC. Under the slowly evolving wave approximation the nonlinear envelope-equation (NEE, [194]) is solved for a scalar, 2+1D paraxial field in a split-step scheme in space and time (see section §A.3).

An initially 140 fs long pulse with 9  $\mu\text{J}$  energy is propagated through the nonlinear waveguide with parameters described in section 5.1.4.3. By extracting the spectrum a Fourier-transform-limited pulse-width can be computed at each radial coordinate of the pulse. The rms deviation over the radial coordinate relative to the mean transform-limit after each waveguide-pass serves as a measure for spectral homogeneity. The radial coordinates are normalized to a circle, containing 95 % of the pulse's energy.

<sup>10</sup>... as well as the cost of a coating run.



(a) Radially resolved Fourier limits. The radial coordinate is normalized to contain 95 % of the total pulse-energy. The data are collected after each pass through the waveguide, indicated by an incremental color-change and labeled accordingly. The Fourier-limits for up to 10 passes are displayed.



(b) rms deviation of the Fourier limit calculated from figure 5.10a relative to the mean.

**Figure 5.10.** – Results of simulated 2+1D pulse propagation through the nonlinear waveguide described in section 5.1.4.3. The pulse passes 10 times through a 6 mm thick fused silica window.

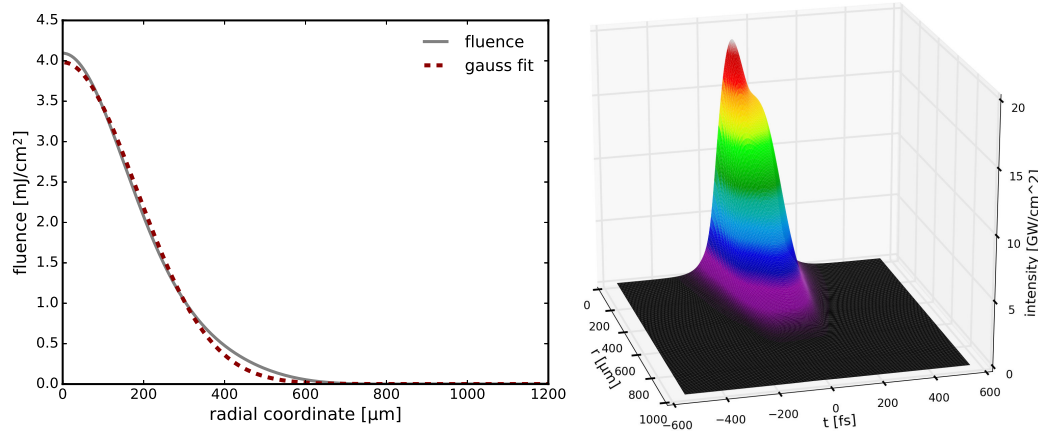


**Figure 5.11.** – Simulated (left) fluence and (right) intensity profiles of the pulse at the output plane after 10 passes.

In figure 5.10 the simulation results for each broadening pass up to 10 passes are summarized. On the first pass through the waveguide the pulse is distorted with more than 10 % rms deviation of the FTL. The consecutive passes, however, significantly improve the homogeneity and after the final 10<sup>th</sup> pass the rms deviation has shrunk to <1 %. The homogenization is not monotonically improving but the trend is toward less deviations with increasing number of passes. In this ideal situation the resulting Fourier-limited pulse-duration can be 55 fs after only 10 waveguide passes.

The predicted fluence at the output plane is shown in figure 5.11. A perfect gaussian shape can not be retained, however, no self-diffraction rings are generated, potentially leading to a substantial improvement of the obtainable peak-intensities. The simulated intensity-profile is also shown. The asymmetry in the temporal dimension is caused by space-time focusing in the NEE which does not appear if only the basic nonlinear Schrödinger equation is solved. For the narrow-band pulses obtained in the first compression-stages this effect does not play a crucial role yet and nonlinear Schrödinger as well as NEE solutions are similar. However, it is known that space-time focusing in dispersive media can lead to temporal splitting of very short pulses [195, 196] and might become a more influential factor once sub-30 fs are targeted.

The stability of the 2-mirror waveguide, defined by the Gouy-phase  $\phi_G$  has a distinct influence on the homogeneity of the broadened pulse. From the simulation results one can predict an optimal tradeoff between sensitivity to mode-matching errors, spatial-spectral homogenization and deterioration of the beam-profile. Values of  $\phi_G$  close to  $\pi$  result in a waveguide that is very insensitive to mode-matching errors in the presence of a Kerr-lens, i.e. the mode-size does not easily run away for many passes. This is in stark contrast to the center of stability,  $\phi_G = 1/2\pi$ , where the mode is unstable with respect to the Kerr-lens and quickly runs away after only a few passes. The simulation results of the waveguide for different  $\phi_G = [0.6, 0.7, 0.8, 0.9, 0.95] \pi$  are depicted in figure 5.12. The total accumulated nonlinear phase  $\phi_{NL} = 2\pi$  was kept fixed by adjusting the broadening-window thickness.

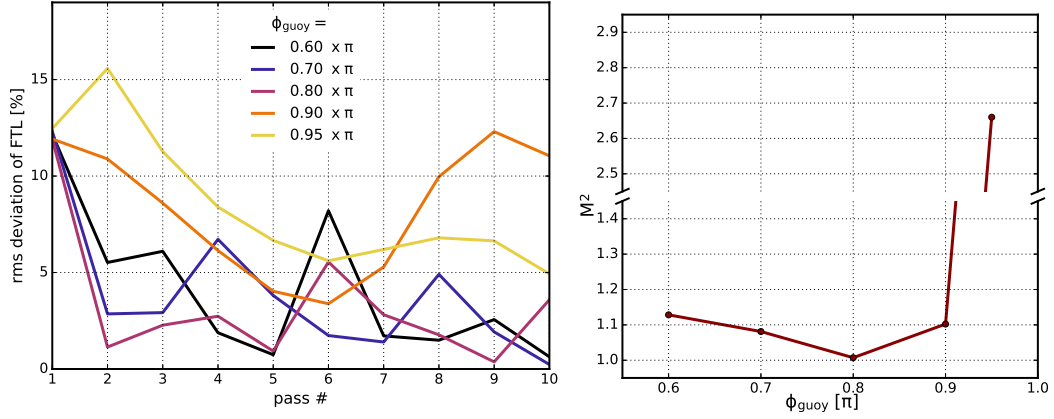


**Figure 5.12.** – Simulations for varying  $\phi_G$  and fixed total  $\phi_{NL} = 2\pi$ . (left) Spectral-spatial homogeneity with relative rms deviations of the radially resolved Fourier-transform limits. (right)  $M^2$  beam-quality factor after the waveguide.

As expected, the beam-quality quickly deteriorates at the stability edge ( $\phi_G = 0.95\pi$ ). The spatial-spectral distribution also does not improve as desired after the first broadening pass. The waveguide with  $\phi_G = 0.9\pi$  exhibits the worst spatial-spectral homogeneity, despite an improved  $M^2$  value. Homogenization becomes drastically better when  $\phi_G < 0.9\pi$ . Configurations with  $\phi_G < 0.5\pi$  were not considered practical using reflective optics due to the short mirror-separation and resulting problem of astigmatism.

Strong nonlinear phase-shifts in the waveguide can also be realized while retaining reasonable beam-quality and spectrally homogeneous beam-profiles. Figure 5.13 shows simulation results for different  $\phi_{NL}$  per waveguide pass with a fixed  $\phi_G \approx 0.7$ .

#### 5.1.4.3. Compression in a first stage

The laser-source used in the following experiments was the oscillator described in section 3.5, delivering 140 fs long pulses with 9  $\mu\text{J}$  pulse energy. Compression was planned in two stages where each stage should consist of a nonlinear waveguide as described above with a small number of passes and a subsequent chirped-mirror compressor. The target nonlinear phase for each stage was  $\sim 2\pi$ , corresponding to a broadening/compression-factor of 2 - 3.

A nonlinear waveguide was constructed according to the simulation-results in section 5.1.4.2 (see figure 5.14). Up to 9 passes through 6.3 mm thick, AR-coated fused silica windows were realized with spherical mirrors having a 300 mm radius of curvature (beam-path up to point '1'). The mirrors were separated by 480 mm and the broadening windows placed in the center, corresponding to the configuration with  $\phi_G = 0.7$ . Two lenses match the oscillator beam to the waveguide mode. The expected nonlinear phase per pass was  $\approx 0.2\pi$  which already introduces a noticeable Kerr-lens. The computed mode-size distribution in the waveguide is shown in figure 5.15 with and without a Kerr-lens in the center.

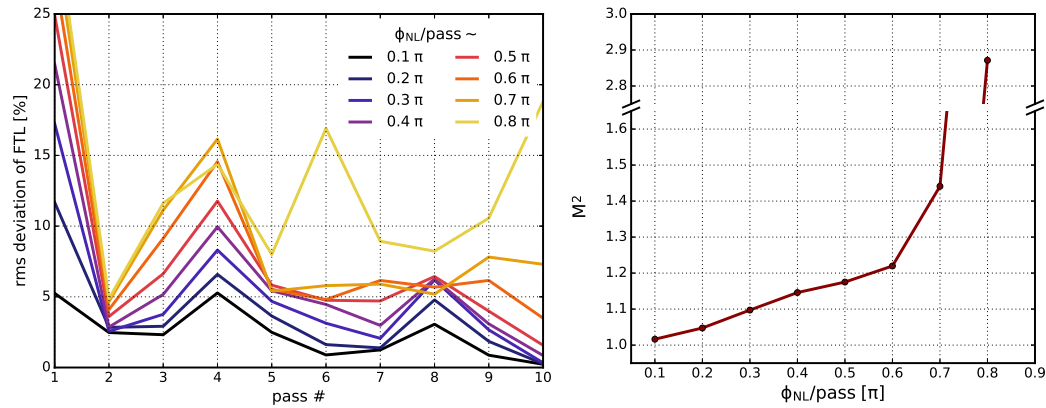


**Figure 5.13.** – Simulations for varying  $\phi_{NL}$  up to 10 passes. (left) Spatial-spectral homogeneity with the rms deviation of the radially resolved Fourier-transform limits. (right)  $M^2$  beam-quality factor after the waveguide.

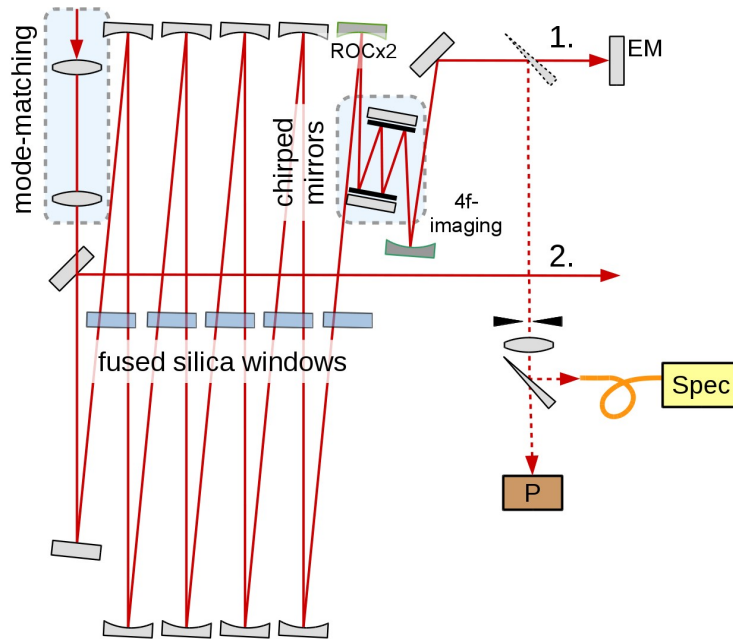


**Figure 5.14.** – Sketch of waveguide compression stage. The input beam is mode-matched to the waveguide via two lenses and propagates 9 times through the 6 mm thick, AR-coated fused silica plates. The last mirror of the waveguide has  $2 \cdot ROC_{waveguide}$  and sends the beam to the chirped-mirror compressor inbetween a 4-f imaging telescope. At position 1. the beam was optionally picked off for spatial-spectral characterization (dashed wedge). The end-mirror EM returned the beam toward the waveguide (including a second pass through the CM-compressor), keeping the mode nearly matched by the second reflection on the curved mirror with  $2 \cdot ROC_{waveguide}$ . After propagation 9 times more through the fused silica windows the beam was finally picked off towards '2.'. This was due to a slight misalignment of the beam-path on the return-trip. P: power-meter; Spec: fiber-coupled spectrometer.

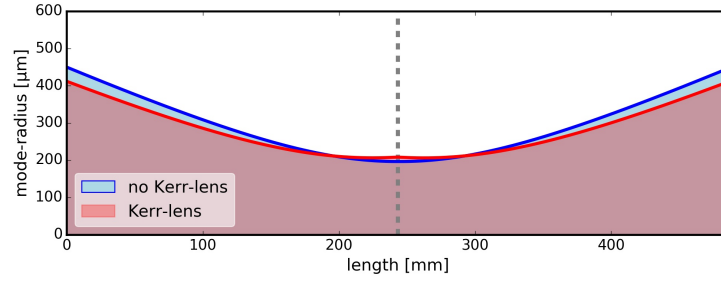


**Figure 5.15.** – Calculated mode-size distribution in the utilized waveguide with and without Kerr-lens.

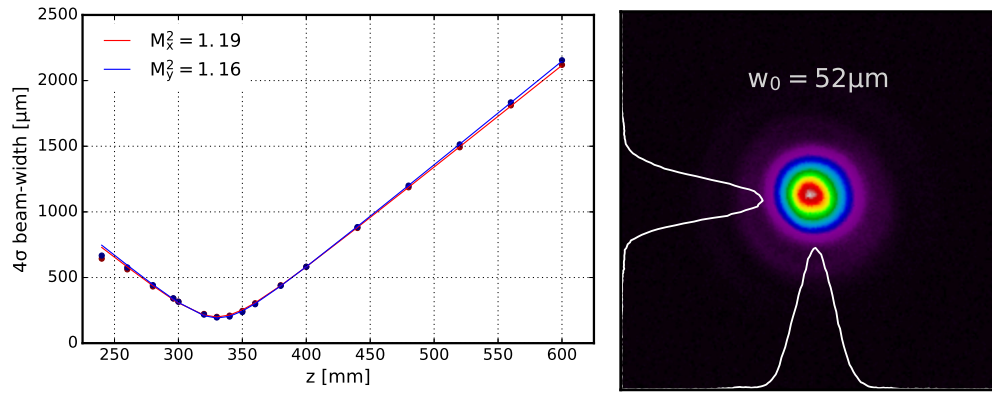


**Figure 5.16.** – (left)  $M^2$  beam-quality measurement of the spectrally broadened laser after the first waveguide-pass. (right) Beam-profile in the focal plane.

145 W average power from the oscillator were sent through the setup and the spectrum recorded. In an attempt at characterizing the spatial-spectral homogeneity the attenuated beam was centered and sent through an iris and both transmitted power and spectrum were recorded for different iris openings. The deviation of the recorded spectra were very small. The beam-profile was characterized by measuring the  $M^2$  factor, yielding  $<1.2$  for both beam-axes (see figure 5.16).

The pulses were compressed to  $\sim 60$  fs duration using a total GDD of  $-4000$  fs<sup>2</sup> with chirped mirrors. The corresponding intensity-autocorrelation trace is shown in figure 5.17.

#### 5.1.4.4. Compression in a second stage

After compression to 60 fs pulse-duration the second stage was realized by reflecting the beam once more through the waveguide with a slight angular offset. The input mode was kept the same by imaging the beam back onto the last curved mirror with a curvature radius of 600 mm instead of 300 mm by virtue of a 4-f telescope (500 mm ROC). As the simulations indicate, the higher nonlinear phase-shift per nonlinear step does not pose a problem for the beam-quality and spectral homogeneity yet. The compressor mirrors were situated inside the telescope and consequently could make

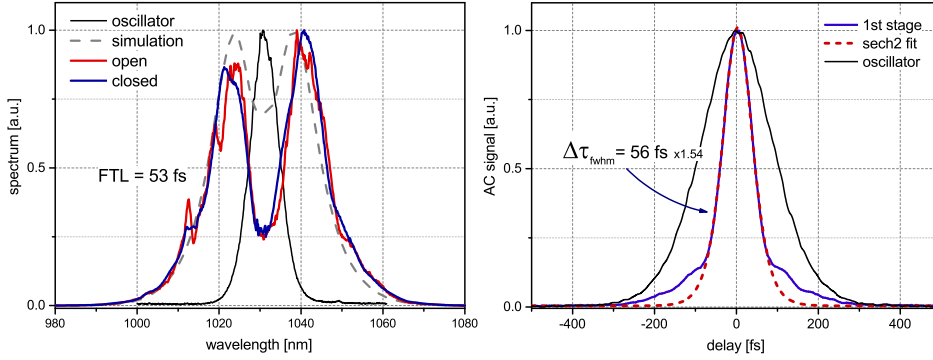


**Figure 5.17.** – (left) Simulated and measured spectrum after the waveguide. ‘open’ and ‘closed’ refer to the configuration of the aperture and demonstrate the spatial homogeneity of the spectrum. The Kelly-sidebands of the oscillator are clearly visible in the red spectrum. (right) Intensity-autocorrelation of the compressed pulses.

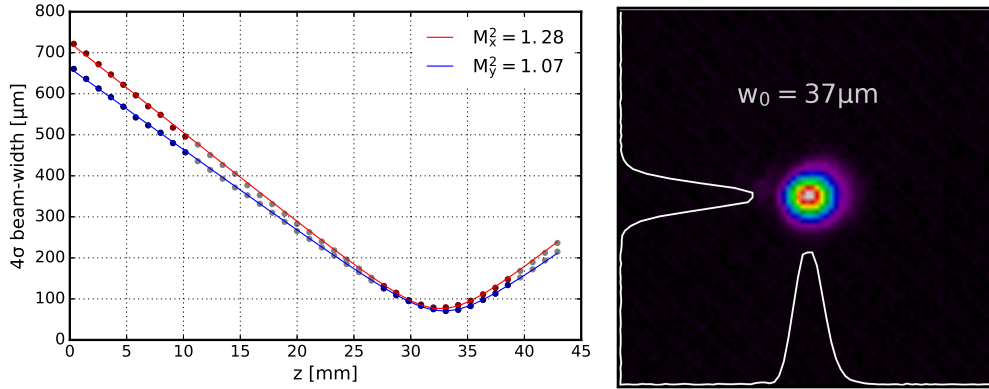


**Figure 5.18.** – (left)  $M^2$  beam-quality measurement of the spectrally broadened laser after the second waveguide-pass. (right) Beam-profile in the focal plane.

do with only two chirped mirrors due to the additional return pass. The returning beam (‘2’) was picked off with a  $45^\circ$  mirror before the mode-matching lenses. The  $M^2$  value stayed below 1.3 (see figure 5.18) with a good beam-profile in the focus. The returning beam was slightly clipped on the pick-off mirror due to very tight space-constraint and consequently a small structure is visible in the tangential (x-) plane. As in the first stage the spectrum did not change when closing an aperture and showed a Fourier transform limit of 27 fs. Although one might expect the spectral bandwidth to have increased quite a bit more due to the larger peak-power in the second stage, the pulse runs apart increasingly fast due to dispersion as the bandwidth grows. Another important aspect was that the coatings on some of the utilized mirrors in the waveguide were rather narrow-band and exhibited higher losses for the broadened spectral wings.

Compression was realized with chirped mirrors having  $-500 \text{ fs}^2$  GDD. After four reflections the pulse was compressed to 30 fs as seen on the intensity autocorrelator

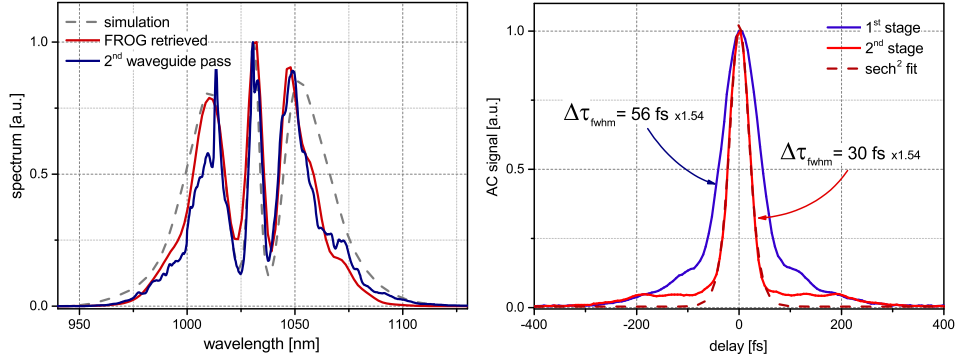


**Figure 5.19.** – (left) Measured -blue- and FROG-retrieved -red- spectra after the second broadening stage. (right) Intensity autocorrelation trace of the compressed output pulse. It has a FWHM of 30 fs if a  $\text{sech}^2$  pulse-shape is assumed.

(figure 5.19). The exact pulse-shape was retrieved from a second-harmonic FROG (SH-FROG) measurement, showing a 32 fs pulse (figure 5.20) that justifies the use of the  $\text{sech}^2$  fit on the autocorrelation trace. The good agreement between measured and retrieved spectrum is an additional indicator of spatial-spectral homogeneity since the SH-FROG also acts as a spatial filter. The total transmitted average power through both waveguides, including the compressors was 136 W.

**Discussion** The nonlinear waveguide approach to SPM-induced spectral broadening shows exceptionally high throughput efficiency of 95 %, while retaining good beam-shape as well as spatial-spectral homogeneity as predicted in simulation (see section 5.1.4.2). After compression to 32 fs the peak-power of the pulses is estimated to be 230 MW, including the power-loss to the small side-structures in the pulse. This is a value that is already interesting for high-harmonic generation in a single-pass setup [197].

The compression-factor of 4.4 in such a compact setup is not yet on par with the performance of fiber-broadening where usually a factor of 8-10 is achieved, however, the setup is insensitive to beam-pointing fluctuation and beam-drift. The intensity-noise before and after the compression setup was recorded with a RF spectrum-analyzer and is depicted in figure 5.21. Noise is added mainly in the acoustic region between 100 Hz and 10 kHz and is caused by air-fluctuations, resulting in an increased beam-pointing cone on the photo-diode. This noise can be reduced by either covering the 12 m long beam-path or placing the setup in an air-tight housing, preferably evacuated. The broadened spectrum was long-term stable and did not breathe or fluctuate.

Compression to below 30 fs requires an increased number of passes through the nonlinear waveguide, however, as simulations show, the material dispersion hampers rapid broadening to below 15 fs. While stronger focusing into thinner windows can also help to reduce the effects of dispersion, this also means working much closer to the stability-edge of the waveguide where the beam-quality suffers more. Therefore, in order to reaching the few-cycle regime <10 fs, proper dispersion-compensation

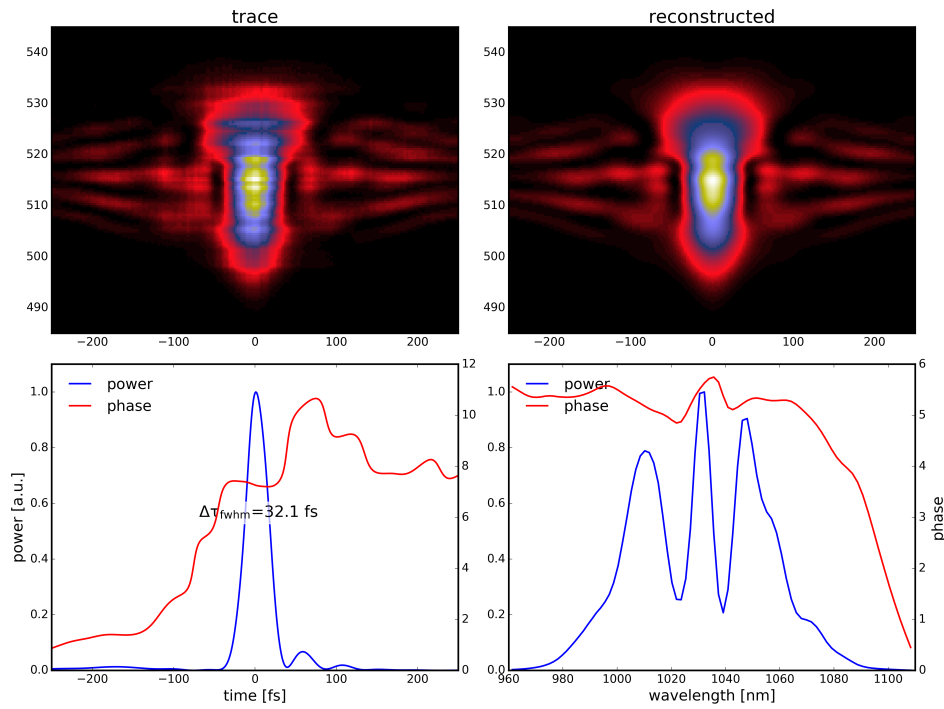


**Figure 5.20.** – Measured and retrieved FROG traces after the second pass through the waveguide including the pulse-compressor. The FROG-error was 0.33 %.

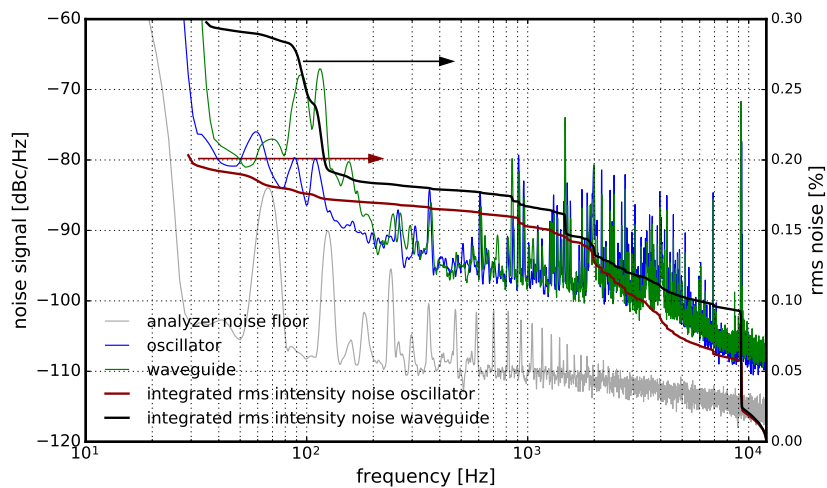


**Figure 5.21.** – Intensity-noise recorded with a RF spectrum-analyzer before and after the waveguide. Noise below 25 Hz was not considered due to limitations of the analyzer.

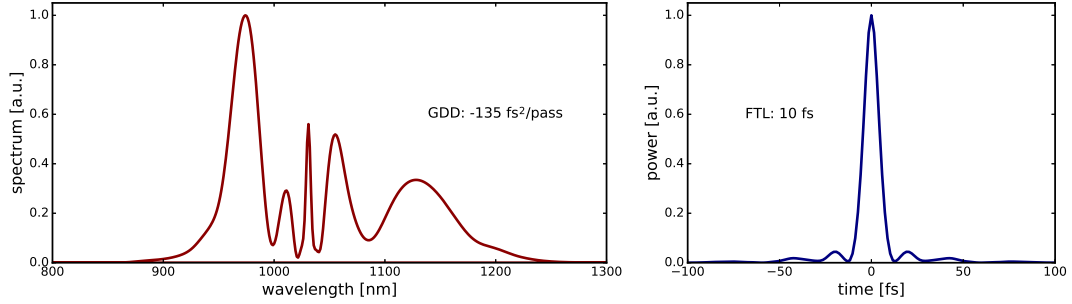


**Figure 5.22.** – (left) Spectrum and (right) Fourier-limited shape of the simulated pulse passing 30 times through the nonlinear waveguide-sections. 10 fs duration are estimated with a dispersion-compensation of  $-135 \text{ fs}^2$  per pass.

material	in: $\Delta\tau_{fwhm}$	out: $\Delta\tau_{fwhm}$	$f_{broad}$	self-diffr. loss	total efficiency	$P_{pk}$
18 passes through 6 mm fused silica + intermediate compression	140 fs	32 fs	4.6	$\sim 0 \%$ $M^2 < 1.3$	95 %	230 MW

**Table 5.4.** – Waveguide compression results.  $f_{broad}$  is the spectral broadening factor.

is required. The dispersion of the waveguide can easily be tailored by applying dispersive-coatings to the curved cavity mirrors. Provided the right management of dispersion even self-compressing pulses can be realized. However, this is not advisable for retaining high throughput efficiency since the peak power and therefore nonlinear phase-shift per pass would blow up, quickly degrading the pulse-quality. Nearly exact matching of the GDD from the fused silica plates thus yields best results. A total number of 30 passes in the same waveguide as in the experiments, yet with  $-130 \text{ fs}^2$  GDD coated, curved mirrors allows the generation of 10 fs pulses in the simulations (figure 5.22). The computations also predict an  $M^2$  beam-quality factor below 1.4 and a spatial-spectral rms deviation of  $< 10 \%$ . The high number of passes can efficiently be realized in a multi-pass arrangement such as a Herriott-cell [198] as has been demonstrated already in [181]. The peak-power of 0.5 GW should thus be reached without amplification of the oscillator output.

**Peak-power scalability** The simultaneous peak- and average power scaling with this approach is not unproblematic. The nonlinear phase-shift per pass needs to stay  $< 0.6\pi$  in order to retain a reasonable compressibility and beam-profile. For narrow bandwidth pulses  $\phi_{NL}/pass$  should be even smaller since the total nonlinear phase required to reaching the few-cycle regime is larger. This can be reached e.g. by reducing the material-thickness. However the high average power of  $> 100 \text{ W}$  obtained from today's thin-disk oscillators (and possibly kW in the future) puts an additional constraint on the window thickness since thermally induced stress can easily result in fracture of the material. The material thickness should therefore not

be reduced below the mm scale. The other option to reducing  $\phi_{NL}/pass$  is increasing the mode-sizes in the waveguide which in turn implies longer propagation distances. This is owed to the fact that the mode-area in a cavity or waveguide increases linearly with it's length  $L$  [100] and therefore  $P_{pk} \propto L$ .

Let us assume a minimal window thickness of 1 mm and a KLM oscillator that can deliver 1 GW peak-power. The nonlinear phase-shift should stay constant as in the above experiment and therefore the single-path length needs to be increased by a factor of nearly 3 to 1.3 m. The same estimation for 10 GW<sup>11</sup> would lead to a waveguide length of 13 m. At such lengths the contribution of air to the nonlinear phase-shift is much larger than the thin material placed in the beam path and should be seen as the way forward. Even in the case of 1 GW the atmospheric contribution is dominant and it might be beneficial to work in a reduced pressure environment to control the influence of atmospheric noise and beam-pointing fluctuations.

## 5.2. Cascaded $\chi^{(2)}$ nonlinearities

The quadratic nonlinearity of birefringent crystals is most prominently used in three-wave-mixing frequency-conversion processes. However, it was also realized that the second order nonlinear susceptibility,  $\chi^{(2)}$ , which can be much larger than typical  $\chi^{(3)}$  nonlinearities, are suitable for spectral broadening and compression applications [55]. The simplest case is considered in type-I phase-matched second harmonic generation with monochromatic plane wave fields. There a field  $A_1$  at the fundamental oscillating frequency  $\omega$  and ordinary polarization is converted to the second harmonic field  $A_3$  at frequency  $2\omega$ , being phase-matched in the extraordinary polarization with a phase-mismatch  $\Delta k = k_{2\omega}^{(e)} - 2k_{\omega}^{(o)}$ .

$$\frac{dA_1}{dz} = -i \frac{\omega}{4cn_{\omega}} \chi^{(2)}(\omega; 2\omega, -\omega) A_3 A_1^* e^{-i\Delta k z} \quad (5.3)$$

$$\frac{dA_3}{dz} = -i \frac{\omega}{2cn_{2\omega}} \chi^{(2)}(2\omega; \omega, \omega) A_1 A_1 e^{i\Delta k z} \quad (5.4)$$

At  $\Delta k = 0$  the fundamental wave (FW)  $A_1$  efficiently transfers energy into the second harmonic (SH) wave  $A_3$  and quickly depletes  $A_1$  upon propagation. A phase-mismatch  $\Delta k \neq 0$  leads to interference between  $A_1$  and  $A_3$  and cycles of back-conversion from the SH to the FW, with reduced overall SH conversion efficiency. The larger the phase-mismatch  $|\Delta k|$ , the shorter these conversion-periods as illustrated in figure 5.23(left). Due to a phase-velocity difference between the SH and FW the FW accumulates a nonlinear phase-shift  $\Phi_{nl}$  upon each back-conversion cycle. Under the assumptions of negligible FW-depletion as well as large  $|\Delta k|$  the cascaded  $\chi^{(2)}$  process can be treated as an approximate Kerr-nonlinearity such as in  $\chi^{(3)}$  interaction with an effective nonlinear refractive index

$$n_{2,eff}^{shg} = \frac{-2\omega d_{eff}^2}{c^2 \epsilon_0 n_{\omega}^2 n_{2\omega} \Delta k}. \quad (5.5)$$

<sup>11</sup>A peak-power that is unlikely to be achievable with direct oscillator output in the near future.

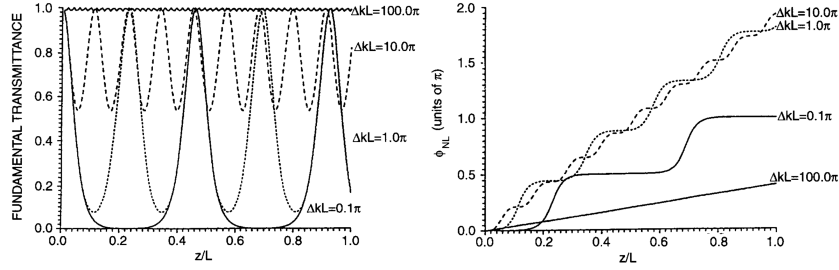


**Figure 5.23.** – (left) FW transmission through type-I SHG crystal for varying phase-mismatch. (right) Evolution of nonlinear phase-shift along crystal length. Adapted from [56]

The effective quadratic nonlinear coefficient is  $d_{eff}^2 = |\chi^{(2)}(2\omega; \omega, \omega)|/2$ . The total cubic nonlinear refractive index is then constituted of  $n_{2,eff} = n_{2,eff}^{shg} + n_2^{kerr}$ . Due to the choice of sign of  $\Delta k$ , e.g. via the tuning angle  $\theta$ , the sign of  $n_{2,eff}$  can be adjusted freely. As a consequence the resulting nonlinear phase can either enhance the materials (self-focusing) Kerr-nonlinearity with positive sign of  $n_{2,eff}$  or produce a self-defocusing nonlinearity. Speaking in terms of pulse compression, a self-focusing nonlinearity produces a positively chirped spectrum which has to be compensated by anomalous dispersion while the self-defocusing case produces a negative chirp, compressible via normally dispersive elements. Apart from the aspect of spectral broadening the potential applications of these cascading  $\chi^{(2)}$  nonlinearities lie in the suppression of self-focusing in amplifiers [199] or in the self-compression of ultrashort pulses [183]. A recent experiment in our group incorporates cascaded, defocusing  $\chi^{(2)}$  interaction in type-I mismatched BBO to reach 30 fs short pulses from a 190 fs, 90 W oscillator in 3 stages [57]. The throughput efficiency was  $>75\%$  due to losses into the SH and resulted in a peak-power of 60 MW from an initial 19 MW.

It has to be pointed out that for larger nonlinear phase-shifts ( $> \pi$ ) the assumption of weak pump-depletion does not hold anymore and the second-order nature of the nonlinearity becomes apparent. In particular the phase-shift is then no longer (approximately) linear with the FW input-intensity but displays a saturation behavior except for at very large phase-mismatch (see figure 5.24 and reference [200]). The saturation with intensity is interesting inasmuch it might provide a reduction of the self-diffraction losses that are inherent to all bulk spectral-broadening approaches and improve the spatial compressibility of the whole beam.

### 5.2.1. Spectral broadening with type-I SHG in BBO

With  $\sim 2$  pm/V the birefringent crystal beta-barium-borate ( $\text{BaB}_2\text{O}_4$ , BBO) has a very high quadratic nonlinear coefficient and can be type-I phase-matched at 1030 nm with the second harmonic at 515 nm. Thus, the intrinsic Kerr-nonlinearity  $n_2^{kerr} \approx 4 \cdot 10^{-20} \text{ m}^2/\text{W}$  can easily be overcome by detuning the phase-matching angle away from  $\theta=23.4^\circ$  [201]<sup>12</sup>. Further beneficial properties of BBO are its

<sup>12</sup>According to equation (5.5)  $n_{2,eff}^{shg}$  is of the order  $-1 \cdot 10^{-19} \text{ m}^2/\text{W}$ .

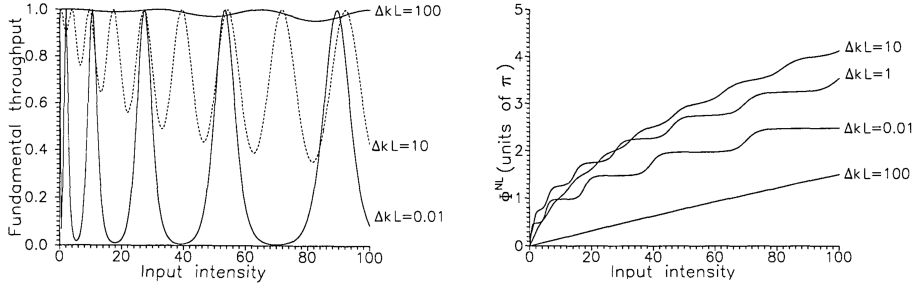


**Figure 5.24.** – (left) FW depletion with irradiance. (right) Saturation of the nonlinear phase-shift with FW input irradiance. Adapted from [200]

ready availability due to widespread use in diverse applications<sup>13</sup> owing to the broad transparency- and phase-matching range as well as high damage-threshold. The phase-matching in BBO is also quite insensitive to temperature-variation (no non-critical phase-matching).

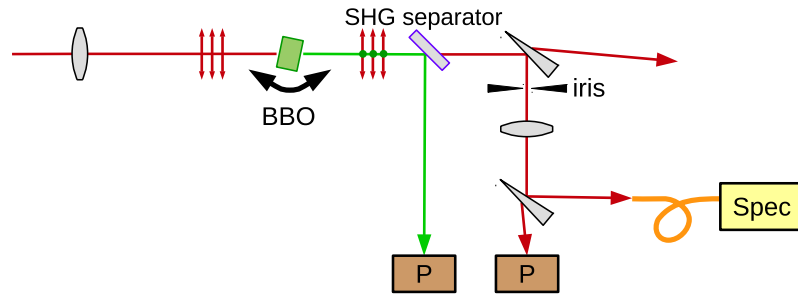
For the experiment an AR-coated, 4.4 mm thick BBO, cut for type-I SHG was used to spectrally broaden the output of the 140 fs oscillator described in section 3.5. The crystal was placed within the Rayleigh-range after a focal spot of  $\sim 200$   $\mu\text{m}$  diameter. The resulting peak irradiance incident on the BBO was therefore  $\leq 400$   $\text{GW}/\text{cm}^2$ . In order to determine the phase-matching angle relative to the incidence angle a tuning-curve of the SHG power was recorded while rotating the BBO in the plane parallel to the table against the p-polarized input beam (see figure 5.26,right). To quickly check the sign of the phase-mismatch one can inspect the shrinking or expanding of the beam-profile while increasing the incident power. A further indicator for defocusing, negative nonlinear phase-shift is an asymmetric deformation of the fundamental spectrum as described in reference [202]. A negative phase-mismatch  $\Delta k$ , leading to a focusing nonlinearity, is reached for detuning-angles  $> 0$ .

In order to characterize the losses due to spatio-spectral inhomogeneity the beam-profile was apertured with a variable iris (see figure 5.25). The transmitted spectrum was measured for several values of the power-transmission through the iris, namely 100, 80, 60, 40 and 20 %. Of course this type of characterization has to be taken with a grain of salt since changes in the spatially integrated spectrum carry much more weight when the aperture is nearly closed than when it is almost open. However, the procedure is easily repeatable.

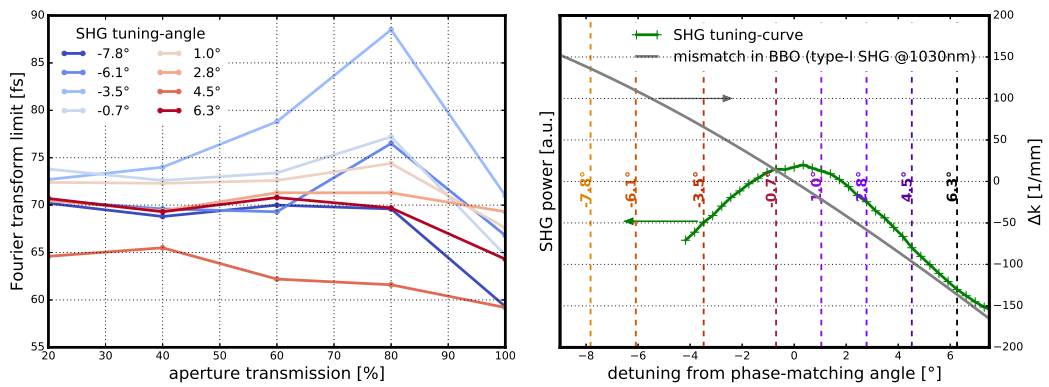
The spectral inhomogeneity of the beam-profiles is shown in figure 5.26(left) for SHG tuning angles from  $-7.8^\circ$  to  $6.3^\circ$ . The Fourier-transform-limits of the apertured spectra are plotted for each measured tuning angle. A perfectly homogeneous beam should result in a horizontal line. The broadest spectrum measured at  $\theta = 4.5^\circ$  in the central part of the beam-profile has an FTL of 65 fs.

The main loss-channels are a) power transferred to the second harmonic and b) deterioration of the beam-profile. Under 150 W average power incident on the BBO, the SH average power generated is displayed in table 5.5.

<sup>13</sup>e.g. electro-optical crystal in Pockel's cells, SHG, THG, FHG



**Figure 5.25.** – Measurement setup for spectral homogeneity after focusing into BBO. Spec: spectrometer, P: power-meter



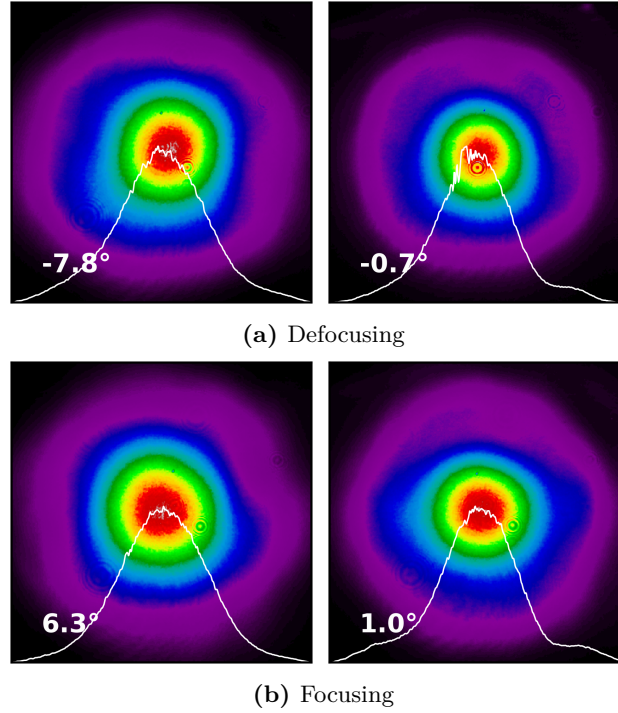


**Figure 5.27.** – Far-field beam-profiles after spectral broadening in BBO. Detuned type-I SHG for effectively self-focusing and self-defocusing nonlinearity.

angle [°]	-7.8	-6.1	-3.5	-0.7	1.0	2.8	4.5	6.3
SH power [W]	5.1	8.0	>10	>10	>10	7.8	4.7	3.3

**Table 5.5.** – Second harmonic power generated for changing tuning-angle. Measurements >10 W were not taken due to the detector-limit.

Closer to phase-matching the SH power began to rocket and measurement was aborted<sup>14</sup>. The beam-profiles of the FW are displayed in figure 5.27 and roughly resemble the far-field distribution.

**Discussion** Far away from phase-matching ( $-7.8^\circ$ ,  $6.3^\circ$ ) the spectra look very similar and the FTL are distributed equally (see figure 5.26, left). The  $\chi^{(3)}$  nonlinearity seems to dominate. The beam-profiles (figure 5.26) with focusing phase-shifts (positive tuning-angles) appear more homogeneous than the defocusing ones and might hint at a saturation-effect as pointed out above [200]. As the beam was chosen diverging at the crystal input surface, the defocusing nonlinearity resulted in an even quicker diminishing of the intensity inside the crystal and the overall spectral broadening was reduced as compared to the self-focusing side. This is also supported by the stronger spectral deviations in the beam-profiles where saturation would not have set in to flatten out the distribution. The broadest spectrum was measured at an

<sup>14</sup>Also out of fear to damage the crystal.

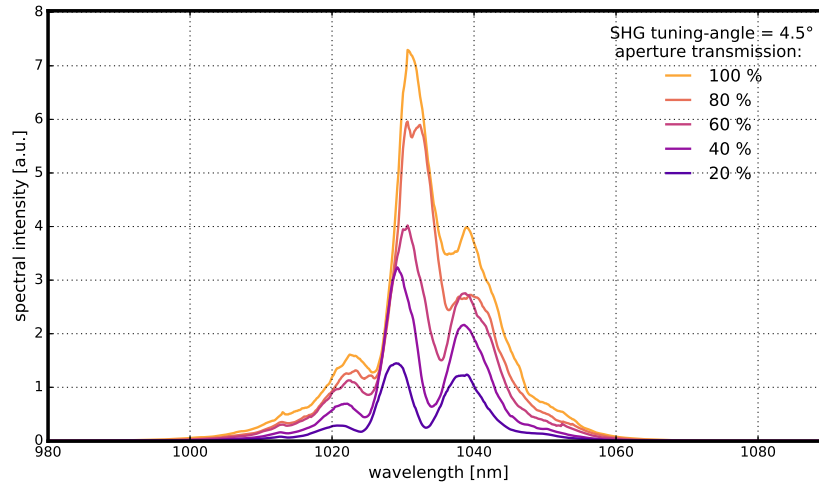


**Figure 5.28.** – Spectrum measured after spectral broadening in BBO with self-focusing phase-mismatch ( $4.5^\circ$  detuning). The spectrum is measured behind an iris. The spatial-spectral homogeneity is determined by gradually closing the aperture for transmission-values of 20 - 100 % and comparing the spectral distribution.

angle of  $4.5^\circ$  on the self-focusing side and is depicted in figure 5.28 for varying iris transmission. The corresponding FTL was 65 fs which marks a growth-factor of 2 in spectral bandwidth as compared to the 140 fs input.

While the SHG losses with only 3 % of the total power are tolerable, the deterioration of the beam-profile started showing (see figure 5.27). Interestingly, however, the deformation of the Gaussian profile was not as severe as previously observed in the purely  $\chi^{(3)}$  processes with the same factor of 2 in spectral broadening (compare e.g. figures 5.5 and 5.8). The self-diffraction losses are estimated to be  $\sim 20\%$  by spatial filtering.

### 5.2.2. 2-stage compression with $\chi^{(3)}$ and cascading $\chi^{(2)}$ processes

Somewhat unintuitive results were obtained when applying the same technique with shorter pulses. The 155 W, 10  $\mu$ J, 140 fs pulses from the oscillator were compressed in a two-step setup depicted in figure 5.29. In the first stage a 3 mm thick quartz plate with uncoated surfaces served to spectrally broaden the oscillator output, exploiting only SPM from the  $\chi^{(3)}$  nonlinearity. After introduction of  $-2000$  fs<sup>2</sup> GDD with dispersive mirrors the pulses were compressed to 66 fs, having been confirmed with an intensity-autocorrelator (figure 5.32). The losses caused by self-diffraction ( $\sim 40\%$ ), as well as reflection from the quartz ( $\sim 7\%$ ) amounted to an estimated usable 92 W of average and  $<78$  MW of peak-power.

These pulses served as input to the second compression-stage. Here, type-I phase-mismatched SHG with BBO was employed for spectral broadening as described in section 5.2.1. The here 6 mm thick BBO crystal was cut at  $\theta=23.4^\circ$  and AR-coated for the fundamental as well as for the second harmonic wavelengths. The peak-irradiance on the crystal surface near the focus was estimated to be  $\leq 400$  GW/cm<sup>2</sup>. A

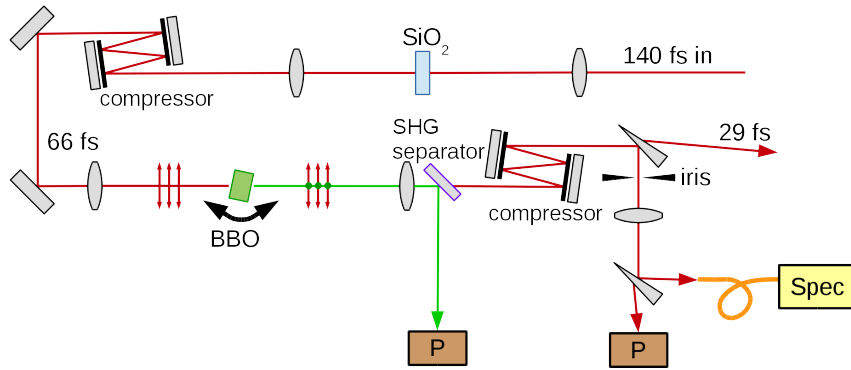


**Figure 5.29.** – Two stage compression setup. First stage:  $\chi^{(3)}$  broadening in 3 mm quartz ( $\text{SiO}_2$ ). The pulses show 66 fs duration after chirped-mirror compressor. Second stage: Phase-mismatched type-I SHG in BBO by detuning the phase-matching angle for positive, self-focusing phase-shift. The FW is separated from the generated SH and compressed in a second CM-compressor. Part of the beam is used to characterize the spatial-spectral homogeneity: An iris is used to transmit in steps 10 - 100 % of the incoming power. The spectrum is collected and measured with the spectrometer. P: power-meter; Spec: fiber-coupled spectrometer.

maximum in spectral bandwidth was measured for detuning the BBO-angle towards enhanced positive nonlinear phase-shifts (self-focusing). The spectrum is displayed in figure 5.32. In this setting the second-harmonic power measured 3 W. An additional 13 W were lost to depolarization.

Astonishingly the beam-profile did not show any directly visible, additional diffraction patterns after sending the full power through the second stage. Spatial-spectral characterization showed a very even spectral distribution when measured for different aperture transmissions (see figure 5.30). The Fourier-transform limits, calculated from the spectra matched within 2 % over the whole beam. A further check of the beam-profile was carried out using band-pass filters at central wavelengths of 970, 1010, 1050, 1064 and 1070 nm each with a  $\sim 10$  nm FWHM passband. The filtered beam-profiles are shown stacked in figure 5.31. A gaussian fit revealed nearly equal beam-widths for each utilized filter. A 1030 nm bandpass filter was unavailable at the time of measurement.

Attempts at compressing the pulses were quite successful. Introducing  $-1000 \text{ fs}^2$  GDD via dispersive mirrors slightly over-compensated the phase but an additional 7 mm thick fused-silica plate could remove the residual chirp. With intensity-autocorrelation the pulse-width was measured to be 29 fs long (see figure 5.32). The trace shows an exceptionally good agreement with the  $\text{sech}^2$  pulse-shape and only very minor side-lobes are visible. In conjunction with  $\sim 75$  W spatially filtered, usable average power the pulse's peak-power can be estimated to be  $\leq 145$  MW. Systematic  $M^2$  beam-quality measurements were not carried out for reasons discussed below. However, the beam was focused down to 60/90  $\mu\text{m}$  FWHM diameter to search for distortions in the profile (figure 5.31,right).

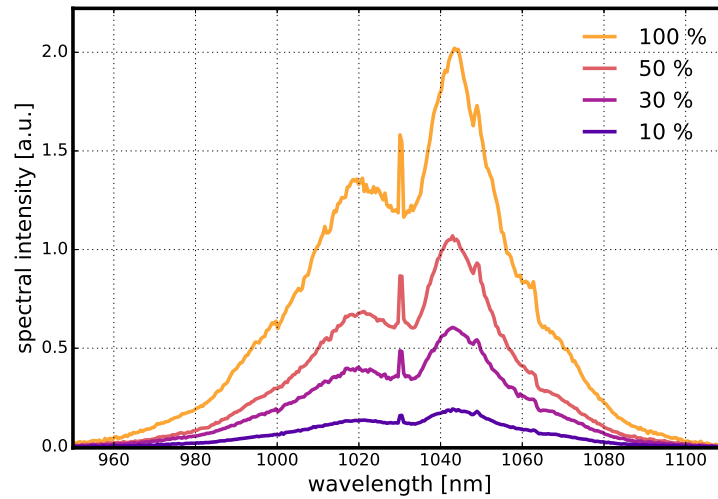


**Figure 5.30.** – Broadened spectrum after the 2<sup>nd</sup> stage (BBO) for varying aperture transmission. The spike in the center is a negligible CW-background from the oscillator.

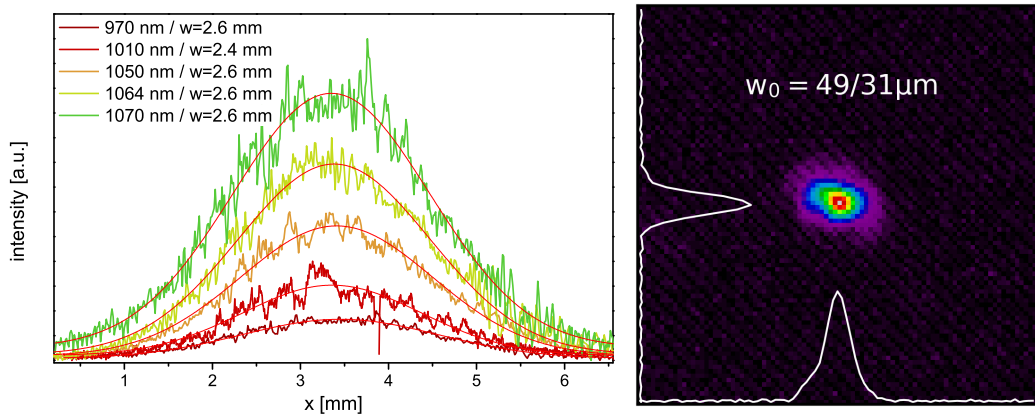


**Figure 5.31.** – (left) Bandpass-filtered beam-profiles after 2<sup>nd</sup> stage compression with cascaded  $\chi^{(2)}$  process in BBO. (right) Intensity distribution in the focus after compression.

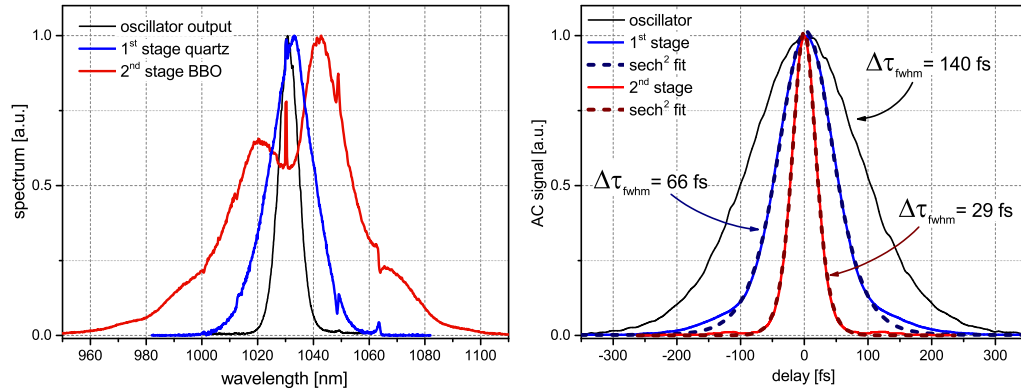


**Figure 5.32.** – (left) Broadened spectrum and (right) intensity autocorrelation traces (i) at the oscillator output, (ii) after the first compression stage (quartz), (iii) after the second compression stage (BBO). The spectrum has a residual CW background from the oscillator it is visible as distinct spike near 1030 nm. Also clearly visible are features originating from the Kelly-sidebands of the oscillator.

**Discussion** The spectral broadening in BBO in a second compression-stage showed a vastly improved homogeneity of the beam-profile over direct first-stage experiments described in section 5.2.1. Combined with a lack of additional diffraction-rings this hints at a saturation-effect. However, it has been recognized in [203] that strong saturation can lead to a distortion of the pulse’s temporal phase. However, the near perfect compression as shown in figure 5.32 is contradictory and does not seem to support an explanation based on saturation alone. The high level of homogeneity in this second broadening stage might also be a product of the same spatial mixing as seen in the case of the nonlinear waveguide, figure 5.13. There a second nonlinear step (refocusing into the broadening-window) always reduced the spatial-spectral deviations.

As seen in figure 5.31,(right) the focused beam is slightly asymmetric. This might have been caused by birefringent beam-walk-off during the critical SHG process. At phase-matching the BBO walk-off-angle between SH and FW is about 54 mrad and usually limits the usable crystal-length or peak-irradiance in SHG applications. For cascading  $\chi^{(2)}$  processes far away from phase-matching the walk-off plays only an insignificant role since the SH-beam is back-converted before it can lose overlap with the fundamental beam.

While BBO is a well understood crystal that can be grown and processed to have high damage threshold, the use for spectral broadening requires extra care<sup>15</sup>. During the above experiments the crystals had to be replaced repeatedly due to fracture-damage. This type of damage happened mostly when close to phase-matching and was caused by thermally induced stress from excessive heat-generation/absorption inside the crystal. The heating of the crystal was always accompanied by the appearance of new spectral components, (red, yellow and turquoise) with larger emission cone

<sup>15</sup>... given the not insignificant cost of thick BBO-crystals, both financially as well as in time to delivery.

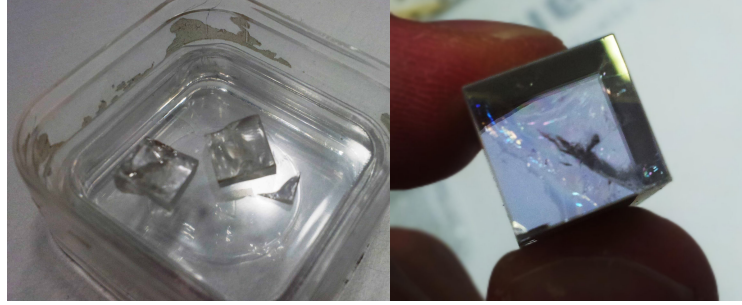


**Figure 5.33.** – Fractured parts of two different BBO crystals. Both crystals started heating up strongly close to phase-matching and fractured due to mechanical stress.

material	in: $\Delta\tau_{fwhm}$	out: $\Delta\tau_{fwhm}$	$f_{broad}$	self-diffr. loss	total efficiency	$P_{pk}$
1. stage: 4.4 mm BBO, $\theta = 23.4^\circ$ , $\varphi = 90^\circ$ , self-focusing	140 fs	70 fs*	2	20 %	77 %	93 MW*
1. stage: 3 mm SiO <sub>2</sub> 2. stage: 6 mm BBO, $\theta = 23.4^\circ$ , $\varphi = 90^\circ$ , self-focusing	140 fs	29 fs	2.3	40 %	48 %	$\leq 145$ MW

**Table 5.6.** – BBO compression results.  $f_{broad}$  is the spectral broadening factor deduced from the FTL. (\*) pulse-width estimated from FTL.

that can be attributed to a strong parametric gain. A possible explanation of the strong heating could be two-photon absorption in crystal defects, in which case Lithium-Triborate (LBO) might be a better option for future experiments. However, LBO has a significantly lower  $d_{eff}$  of only  $0.8 \text{ pm/V}$  and should require longer crystals in order to reach similar performance.

As stated, the 6 mm thick BBO was destroyed during a careless moment before more rigorous characterization like FROG or  $M^2$  measurements could be made. A rapid continuation of the experiments was hindered by the very long delivery time for new BBO-crystals of the same thickness. A more quickly available, 4.4 mm thick BBO-crystal did not produce the desired results with only  $>40$  fs long pulses at the output.

The very recent investigation by M. Seidel [57]<sup>16</sup> revealed that high beam-quality can be retained in the defocusing regime. It requires the crystal to be placed within a narrow range in the converging part of the focus as well as exact alignment of the incidence angle on the BBO. The high intensities and resulting strong defocusing allowed the propagation with high intensity over a longer distance in the crystal without danger of catastrophic damage. This allowed for large spectral broadening factors per BBO-crystal. The good beam-quality and good overall compressibility

<sup>16</sup>After the arrival of new, long BBO-crystals.

of output raise hopes for very compact, high-power compression-setups with hybrid chirped-mirror and material self-compression. In order to explore the potential of cascading, quadratic nonlinearities for high-power pulse-compression conclusively, future experiments need to investigate the effect of saturation on the beam-profile, presumably with longer crystals and also using the direct oscillator output. Reducing the repetition rate to lower the average power load on the BBO (or using LBO) might prove crucial in ensuring safe operation close to phase-matching.

### 5.3. Summary

The results in this chapter clearly indicate the utility of bulk solids in spectral broadening. Even though self-phase-modulation in single pieces of material can lead to broad spectra with broadening factors  $>2$ , the pulses become strongly distorted spatially and perfect compression impossible. The use of multiple-focus geometries mitigates this effect. Incorporating a nonlinear quasi-waveguide with up to 18 passes through fused silica windows and a subsequent chirped-mirror compressor the pulses from the thin-disk oscillator could be shortened by more than a factor 4 to 32 fs. By virtue of the high throughput efficiency of this setup of nearly 95 % the resulting peak power reached 230 MW. Under the condition of dispersion-compensation inside the waveguide with chirped-mirror technology, reaching sub-10 fs pulse-duration appears feasible.

The spectral broadening in cascaded  $\chi^{(2)}$  interactions does provide additional degrees of freedom in the choice of either focusing or defocusing effective nonlinearity. Single-stage spectral broadening in type-I phase-mismatched SHG in BBO both in the focusing and defocusing regime yielded similar results to single-stage broadening in purely cubic nonlinear media. However, for the similar broadening factor of  $\sim 2$  the spatial profile displays less features and also the spatially resolved spectra appear more uniform. Using a two-stage compression scheme, relying on  $\chi^{(3)}$  in a first and focusing cascaded  $\chi^{(2)}$  interaction in a second focusing stage, the spectrum of the seeding oscillator could be broadened by a factor of  $>4$  yielding a peak-power  $\lesssim 145$  MW. The high throughput of the second BBO-stage was accompanied by a strongly uniform spatial-spectral distribution as well as a lack of additional spatial feature in the beam-profile. It is assumed that the saturation of the nonlinear phase-shift combined with the homogenizing action observed in multistage focusing are responsible for the good overall compressibility.

Based on the experimental findings it is expected that these tools for pulse-compression are power scalable at least within the range of foreseeable oscillator peak-power output ( $10 \text{ MW} > P_{pk} > 1 \text{ GW}$ ). The necessary adjustments for waveguide- and cascaded  $\chi^{(2)}$  spectral broadening revolve around increasing the beam-sizes as well as a reduction of the nonlinear material length. Due to the high throughput-efficiency of the waveguide-approach it might remain the preferred method. On the other hand, efficiency can be traded for valuable laboratory-space by relying on cascaded  $\chi^{(2)}$  processes with few, short stages.

## 6. Summary and conclusion

The first aim of this thesis was the demonstration of power-scalability of the thin-disk KLM laser. It was shown in chapter 3 that, similar to average power-scaling with the thin-disk geometry, the peak-power can be increased by enlarging the mode-area in the Kerr-medium. Compared to SESAM mode-locking, the KLM-oscillator can sustain pulses with much higher nonlinear phase-shifts. About 330 fs long pulses with 14  $\mu\text{J}$  pulse-energy and 40 MW peak-power were generated at 270 W average power extra- and 1.3 kW intra-cavity, even operating in a normal air atmosphere. The peak-power inside another KLM-oscillator in low pressure environment could be increased to nearly half a gigawatt while fully utilizing the available gain-bandwidth with 140 fs pulses. The coupled out pulses had a pulse energy of up to 10  $\mu\text{J}$  and 64 MW peak-power. Average power extra- and intra-cavity were measured to be as high as 160 W and nearly 1.1 kW respectively with a good intensity-noise figure of  $<0.5\%$  rms (1 Hz - 1 MHz). The premature assertions by some ([122]) with regard to KLM-scalability stand in contrast to the actually achieved high intra-cavity average- as well as peak-power levels. No fundamental limitations could be identified that would prevent a further power-scaling of thin-disk oscillators via Kerr-lens mode-locking. A push toward 1 GW intra- and more than 100 MW extra-cavity peak-power is realistic and seemingly straightforward when extrapolating experimental results (see figure 3.34 on page 46).

An attempt at improving the efficiency of sub-100-fs generation by switching to the more broadband Yb:CALGO was unsuccessful so far. The reason is not entirely clear and might be the combination of low emission-cross section (and therefore low gain), bad crystal quality and the inhomogeneous broadening of the laser material. The excellent power-handling of Yb:YAG thin-disks in combination with spectral broadening techniques should give an advantage over more broadband yet undeveloped gain-materials that exhibit a much lower emission cross-section, worse crystal quality and heat-removal.

The second aim of this thesis was the identification of an efficient, all-bulk approach to spectral broadening. The pursuit of this goal is described in chapter 5. By implementing a multi-pass, nonlinear quasi-waveguide the output of the oscillator could be compressed to near 30 fs duration and the peak power boosted by almost a factor 4 to 230 MW. The whole compression setup had an overall power-throughput of 95 % as well as good spatial homogeneity. The highly robust, virtually alignment free setup is insensitive to beam-pointing or beam-drift which enables low-noise and long-term stable operation. In combination with the cheap price and ready availability of the utilized optical material this poses a very interesting option to fiber-based compression, where small changes to the seed laser's beam path can lead to tedious and time-consuming realignment of the fiber-coupling. Although the

use of bulk material in a nonlinear waveguide may not be a one-fits all solution it appears ideally suited for the high average- yet moderate peak-powers obtained from thin-disk oscillators. Simulations show the feasibility of efficient pulse-compression to the few-cycle regime.

An alternative to single-pass spectral broadening in media with purely cubic nonlinearity might be found in the use of cascading quadratic nonlinearities. The spatial-spectral homogeneity appears superior to spectral broadening in single media with purely cubic nonlinearity, however, additional losses due to SHG have to be taken into account.

In conclusion, the here developed light sources reach a combination of peak- and average power that were previously only obtained from amplified systems. They can offer a significant simplification for many existing laser systems and will help to enable new experiments in diverse fields.

## A. Appendix

### A.1. Ray transfer matrices for cavity analysis with a Kerr-lens

The use of the so called ABCD or ray-transfer matrix-formalism is wide-spread in optical resonator design and analysis and gives reliable results for fundamental mode, Gaussian beam propagation<sup>1</sup>. An arbitrary linear (CW) cavity is described by the round-trip propagation matrix  $M$

$$M = M_2 \cdot \dots \cdot M_{n-1} \cdot M_n \cdot M_{n-1} \cdot \dots \cdot M_1 \quad (\text{A.1})$$

consisting of  $n$  optical elements (mirrors, interfaces, propagation-distances ...). The condition for cavity-stability is then specified via the complex Gaussian beam-parameter  $\frac{1}{q} = \frac{1}{R} - \frac{i\lambda}{\pi n w^2}$  ( $R$ : phase-front curvature,  $\lambda$ : wavelength,  $n$ : refractive index,  $w$ : beam-radius). The  $q$  parameter is transformed by the matrix  $M$  and it's elements  $A$ ,  $B$ ,  $C$  and  $D$

$$q' = \frac{Aq + B}{Cq + D} \quad (\text{A.2})$$

while a stable mode has to fulfill the condition  $q' = q$ . For a Kerr-lens (equation (2.1)) inside the cavity there is no simple analytic solution since  $M = M(P_{pk}, w_k)$  requires knowledge of the mode-size  $w_k$  inside the Kerr-medium. A solution can be found iteratively by reusing previous mode-solutions  $w_{k,i+1} = f(M(P_{pk}, w_{k,i}))$  until a desired relative error becomes small  $|w_{k,i} - w_{k,i+1}| < \epsilon \cdot w_{k,i}$ . This type of solution usually converges very quickly, however, not so if very close to the stability edge. Alternatively an initial  $q$ -parameter with sensibly chosen initial mode-size  $w_i$  and the fixed curvature  $R$  of the first cavity-mirror can be traced repeatedly through the optical system. On each iteration  $w_i$  is adjusted so that  $w_{i+1} = (w_i + w'_i)/2$  with  $w'_i$  being the mode-size after each round-trip. A solution is again found when  $|w_i - w_{i+1}| < \epsilon \cdot w_i$ .

Some important ABCD matrices are listed in table A.1.

---

<sup>1</sup>A useful book on the subject is [204]

Matrix	Description
$\begin{pmatrix} 1 & d \\ 0 & 1 \end{pmatrix}$	Propagation over distance $d$
$\begin{pmatrix} 1 & 0 \\ -\frac{\kappa}{f} & 1 \end{pmatrix}$	Lens with focal length $f$ or mirror with curvature $R = 2f$ . For tilt with angle $\theta$ in tangential plane: $\kappa = 1/\cos(\theta)$ ; sagittal plane: $\kappa = \cos(\theta)$
$\begin{pmatrix} 1 & 0 \\ 0 & \frac{n}{n'} \end{pmatrix}$	Refraction at plane interface from material with refractive index $n$ into material with $n'$ .
$\begin{pmatrix} 1 & 0 \\ -\frac{1}{f_{kerr}} & 1 \end{pmatrix}$	Kerr-lens of focal length $f_{kerr} = \frac{\pi w^4}{4n_2 P_{pk} L}$ with ( $w$ : beam-radius, $n_2$ : nonlinear refractive index, $P_{pk}$ : peak-power, $L$ : medium thickness)

Table A.1. – Important ray-transfer matrices.

## A.2. Numerical mode-calculations with hard-aperture diffraction

Cavity-mode calculations including aperture-diffraction (and possibly gain-overlap) require the use of numerical procedures such as the algorithm by Fox and Li [205, 100]. It is assumed that the laser-mode is monochromatic. A scalar, complex field  $A(x, y)$  is propagated from  $z_0$  to  $z_1$  through the cavity by solving the diffraction integrals, e.g. Fresnel, Fraunhofer or Rayleigh-Sommerfeld [188, 206].

$$A(x, y, z_1) = \iint K(x, x', y, y') A(x', y', z_0) dx' dy' \quad (\text{A.3})$$

This can be done on a computer most efficiently via the Fourier-transform for non-symmetric or the Hankel-transform for radially symmetric resonators (e.g. paraxial angular spectrum of plane waves). The complete round-trip through the resonator is described by some operator  $\hat{H}$  such that

$$A(x, y, z_0) = \alpha \hat{H} A(x, y, z_0) \quad (\text{A.4})$$

The field  $A$  is a mode of the resonator if it reproduces after one round-trip except some scale-factor  $\alpha$  which describe the transmission  $T = |\alpha|^2$ . The Fox-Li algorithm relies on the assumption that, provided an aperture or amplifying medium is present in the resonator, only the modes of the optical system are transmitted/amplified and all others are strongly attenuated. The arbitrarily chosen initial field  $A_0$  is propagated through the resonator via

$$A_{k+1}(x, y, z_0) = \alpha_k \hat{H} A_k(x, y, z_0) \quad (\text{A.5})$$

and renormalized each time via  $\alpha_k$ . If  $k \rightarrow n$  is large enough,  $|A_n - A_{n-1}| < A_n \epsilon$ , then the field will converge to the resonator-mode.

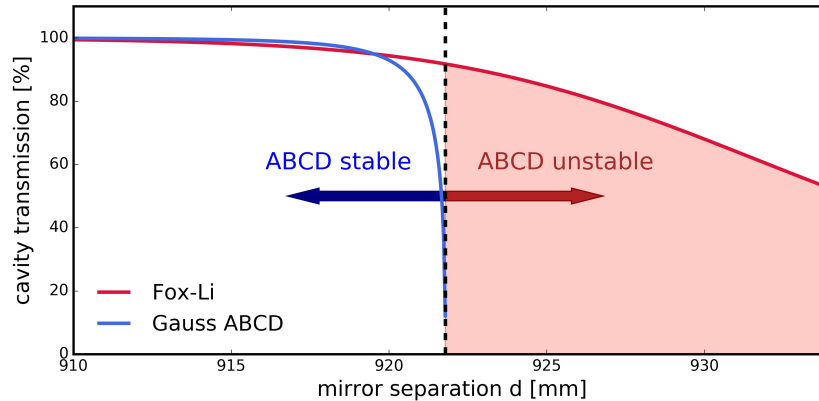


**Figure A.1.** – CW power transmission through a KLM resonator near the stability edge. Estimated both with the ray-transfer-matrix formalism and numerically with Fourier optics and the Fox-Li method. The resonator is unstable in the colored area.

Figure A.1 displays two power transmission curves for the same resonator close to the stability-edge. The power is low and no Kerr-lens is included. One curve gives the results calculated via the ray-transfer matrix formalism for a Gaussian  $TEM_{00}$  mode that is transmitted through an aperture. There can be no solution outside the stable region and the losses rapidly approach 100 %. The red curve is calculated by solving the radially symmetric Rayleigh-Sommerfeld integral and the stable solution obtained via the Fox-Li algorithm. One can see that a solution can still be found outside the expected stability region which exhibits strongly differing losses from the transfer-matrix solution directly at the stability-edge. Experimentally this means that there is no sharp cutoff at the expected stability edge and the mode can still oscillate given enough gain is introduced into the system. However, the gain has to be substantial and the mode is not pure  $TEM_{00}$ .

### A.3. Solution of the nonlinear wave equation

The complicated temporal and spatial structures occurring during spectral broadening can only be revealed by solving the propagation equations for light. Although Maxwell's equations can be solved directly for pulse propagation problems, e.g. with a finite difference scheme, the computational effort is immense. A very useful approximation is to separate the pulse  $E(t)$  into a slowly varying envelope and a fast oscillating term  $E(t) = A(t) \exp(-i\omega_0 t)$  leading to the slowly varying envelop approximation. The simple nonlinear, paraxial Schrödinger equation relies on this approximation which can be applied until a few optical cycles are involved and leads to much reduced computational effort. A nonlinear envelope approximation was derived by Brabec and Krausz [194] that describes well the propagation of pulses even down to the single-optical cycle regime under the slowly evolving wave approximation (SEWA). For paraxial propagation in a transparent medium it reads in the time-domain with  $A = A(x, y, t)$

$$\partial_\xi A = i\hat{D}A + \frac{i}{2k_0} \left(1 + \frac{i}{\omega_0} \partial_t\right)^{-1} \nabla_\perp^2 A + i \frac{2\pi k_0}{n_0^2} \left(1 + \frac{i}{\omega_0} \partial_t\right) P_{nl} \quad (\text{A.6})$$

with the dispersion operator  $\hat{D} = \sum_{m=2}^{\infty} D_m/m! (i\partial_t)^m$ , the transverse laplacian  $\nabla_\perp^2 = \partial_x^2 + \partial_y^2$ ,  $k_0 = k(\omega_0)$  and the nonlinear medium polarization  $P_{nl}$ . The assumption of the SEWA is that both the phase and the field vary slowly along the direction of propagation  $\xi$  such that  $|\partial_\xi E| \ll \frac{n_0\omega_0}{c} |E|$ . For the treated spectral broadening problems in this thesis (quasi-waveguide broadening, section 5.1.4) the Kerr-nonlinearity was assumed to be instantaneous and no delayed Raman response was taken into account such that  $P_{nl} = n_0 n_2 |A|^2 A / 2\pi$ . Effects of space-time focusing as well as self-steepening are automatically included via the time-derivatives in the diffractive as well as nonlinear terms.

**Numerical propagation** The simulations in chapter 5 were carried out by solving equation (A.6) computationally in a split-step fashion in which the linear and nonlinear operators in equation A.6 are applied in an alternating way over small steps in  $\xi$ . In the frequency-domain  $\tilde{A}(x, y, \Omega) = \mathcal{F}_t(A(x, y, t))^2$  the time-derivatives turn into simple multiplications just as the diffraction is best described in the spatial-frequency domain  $\tilde{A}(k_x, k_y, t) = \mathcal{F}_{x,y}(A(x, y, t))$ . Due to the self-steepening term and resulting large exponents the nonlinear step that includes the action of  $P_{nl}$  is applied via an integration step as hinted at in [207]. A large reduction in computation-time is given by the exploitation of radial symmetry in the spatial coordinate and  $\mathcal{F}_{x,y}(A(x, y, t))$  becomes the Hankel-transform  $\mathcal{H}_r(A(r, t))$ . A fast realization of the Hankel-transform, relying only on matrix multiplications was implemented from [208]<sup>3</sup>. Most of the numerical procedures were motivated from [207].

For a small propagation-step  $\Delta\xi$  in a medium the linear operator is applied and the field updated.

$$\tilde{A}(\xi_{i+1/2}, k_r, \Omega) = \tilde{A}(\xi_i, k_r, \Omega) \cdot \hat{O}_{lin} \quad (\text{A.7})$$

where the linear dispersion- and diffraction-operator  $\hat{O}_{lin}$  is defined in the  $k_r, \Omega$ -space as

$$\hat{O}_{disp} = \exp\left(\Delta\xi i 2\pi \left[\frac{n\omega}{c\pi} - \frac{n_0\omega_0}{c2\pi} - \frac{\omega}{2\pi v_g}\right] - \Delta\xi i 2\pi^2 \frac{ck_r^2}{n\omega}\right) \quad (\text{A.8})$$

Here  $n = n(\omega)$ ,  $n_0 = n(\omega_0)$ ,  $v_g = (dk/d\omega|_{\omega_0})^{-1}$  and  $\Omega = \omega - \omega_0$ . After that the nonlinear polarization  $P_{nl}(r, t) = n_0 n_2 |A(\xi_{i+1/2}, r, t)|^2 A(\xi_{i+1/2}, r, t) / 2\pi$  is acquired in the real  $r, t$  space and transferred to  $k_r, \Omega$  space via  $\mathcal{H}_r$  and  $\mathcal{F}_t$  where it is used to integrate the nonlinear part of the propagation equation.

<sup>2</sup> $\mathcal{F}_t$  is the Fourier-transform with respect to the time-variable.  $\Omega = \omega - \omega_0$

<sup>3</sup>The grid in the radial coordinate is not uniform any longer but needs to be sampled according to the roots of the (zero-order) Bessel function.

$A_i$	0.6961663	0.4079426	0.8974794
$B_i$ [ $\mu\text{m}$ ]	0.0684043	0.1162414	9.896161

**Table A.2.** – Sellmeier coefficients for fused silica [210].

$$\tilde{A}(\xi_{i+1}, k_r, \Omega) = \tilde{A}(\xi_{i+1/2}, k_r, \Omega) + \Delta\xi \frac{i\pi\omega}{cn_0} \tilde{P}_{nl}(k_r, \Omega) \quad (\text{A.9})$$

The operation in A.9 can be made more accurate by implementation of an explicit predictor-corrector integration, which requires multiple evaluations of  $\tilde{P}_{nl}(k_r, \Omega)$  [209]. Also it is of advantage for accuracy to do  $\Delta\xi/2$ -steps of the linear operation before and after the nonlinear integration-step.

The linear propagation in vacuum or air can be taken in a single computation step, while the nonlinear propagation in fused silica required usually 30-40 steps until the solution converged.

The refractive index  $n$  as well as the dispersion-coefficients were calculated from the well known Sellmeier equation

$$n^2 = 1 + \sum_i \frac{A_i \lambda^2}{\lambda^2 - B_i^2} \quad (\text{A.10})$$

The Sellmeier coefficients used were taken from [210] and are listed in table A.2. The nonlinear refractive index  $n_2$  was assumed to be  $2.5 \cdot 10^{-20} \text{ W/m}^2$  [123].

The program was written in python and C. Simulation of a waveguide with 20 passes and  $2^{10}$  grid-points in both radial and temporal direction usually took around 10 minutes total computation time on a PC.

## A.4. Long-arm autocorrelator

The setup of the long-arm autocorrelator that was used to check single-pulse operation over a long range is depicted in figure A.2. The 30 cm travel of the stage with a retro-reflector allowed scanning up to 2 ns delay.

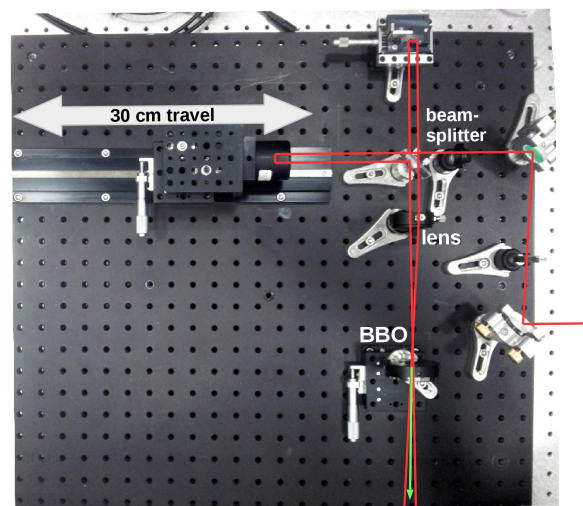


**Figure A.2.** – Setup and beam-path of the long-arm autocorrelator used to verify single-pulse operation

## Bibliography

- [1] L. E. Hargrove, R. L. Fork, and M. A. Pollack. Locking of He-Ne Laser Modes Induced by Synchronous Intracavity Modulation. *Applied Physics Letters*, 5:4–5, July 1964.
- [2] Th. Udem, R. Holzwarth, and T. W. Hänsch. Optical frequency metrology. *Nature*, 416(6877):233–237, March 2002.
- [3] Ahmed H. Zewail. Femtochemistry: Atomic-Scale Dynamics of the Chemical Bond. *The Journal of Physical Chemistry A*, 104(24):5660–5694, June 2000.
- [4] W. H. Knox. Ultrafast technology in telecommunications. *IEEE Journal of Selected Topics in Quantum Electronics*, 6(6):1273–1278, November 2000.
- [5] W. Denk, J. H. Strickler, and W. W. Webb. Two-photon laser scanning fluorescence microscopy. *Science*, 248(4951):73–76, April 1990.
- [6] Ji-Xin Cheng and X. Sunney Xie. Coherent Anti-Stokes Raman Scattering Microscopy: Instrumentation, Theory, and Applications. *The Journal of Physical Chemistry B*, 108(3):827–840, January 2004.
- [7] Antonis Aristeidou, Elise V. Taniguchi, Michael Tsatsos, Rodrigo Muller, Colm McAlinden, Roberto Pineda, and Eleftherios I. Paschalis. The evolution of corneal and refractive surgery with the femtosecond laser. *Eye and Vision*, 2:12, 2015.
- [8] Ferenc Krausz and Misha Ivanov. Attosecond physics. *Reviews of Modern Physics*, 81(1):163–234, February 2009.
- [9] Albert Schliesser, Nathalie Picqué, and Theodor W. Hänsch. Mid-infrared frequency combs. *Nature Photonics*, 6(7):440–449, July 2012.
- [10] Ioachim Pupeza, Daniel Sanchez, Oleg Pronin, Jinwei Zhang, Nikolai Lilienfein, Marcus Seidel, Irina Znakovskaya, Vladimir Pervak, Zhiyi Wei, Ferenc Krausz, Alexander Apolonski, and Jens Biegert. Compact 0.1-W Source of Octave-Spanning Mid-Infrared Femtosecond Pulses Centered at 10  $\mu\text{m}$ . In *CLEO: 2014 Postdeadline Paper Digest*, OSA Technical Digest (online), page STh5C.7. Optical Society of America, June 2014.
- [11] M. Seidel, O. Pronin, and F. Krausz. 1.3 W femtosecond mid-IR source at 8.5  $\mu\text{m}$  wavelength. In *2016 41st International Conference on Infrared, Millimeter, and Terahertz waves (IRMMW-THz)*, pages 1–2, September 2016.

- [12] D. E. Spence, P. N. Kean, and W. Sibbett. 60-fsec pulse generation from a self-mode-locked Ti:sapphire laser. *Optics Letters*, 16(1):42–44, January 1991.
- [13] Cesar Jauregui, Jens Limpert, and Andreas Tünnermann. High-power fibre lasers. *Nature Photonics*, 7(11):861–867, November 2013.
- [14] Peter Russbueldt, Dieter Hoffmann, Marco Hofer, Jens Lohring, Jorg Luttmann, Ansgar Meissner, Johannes Weitenberg, Martin Traub, Thomas Sartorius, Dominik Esser, Rolf Wester, Peter Loosen, and Reinhart Poprawe. Innoslab Amplifiers. *IEEE Journal of Selected Topics in Quantum Electronics*, 21(1):447–463, January 2015.
- [15] Jan-Philipp Negel, André Loescher, Andreas Voss, Dominik Bauer, Dirk Sutter, Alexander Killi, Marwan Abdou Ahmed, and Thomas Graf. Ultrafast thin-disk multipass laser amplifier delivering 1.4 kW (47 mJ, 1030 nm) average power converted to 820 W at 515 nm and 234 W at 343 nm. *Optics Express*, 23(16):21064, August 2015.
- [16] J. Aus der Au, G. J. Spühler, T. Südmeyer, R. Paschotta, R. Hövel, M. Moser, S. Erhard, M. Karszewski, A. Giesen, and U. Keller. 16.2-W average power from a diode-pumped femtosecond Yb:YAG thin disk laser. *Optics Letters*, 25(11):859–861, June 2000.
- [17] U. Keller, K. J Weingarten, F. X Kartner, D. Kopf, B. Braun, I. D Jung, R. Fluck, C. Honninger, N. Matuschek, and J. Aus der Au. Semiconductor saturable absorber mirrors (SESAM's) for femtosecond to nanosecond pulse generation in solid-state lasers. *IEEE Journal of Selected Topics in Quantum Electronics*, 2(3):435–453, September 1996.
- [18] Joerg Neuhaus, Dominik Bauer, Jing Zhang, Alexander Killi, Jochen Kleinbauer, Malte Kumkar, Sascha Weiler, Mircea Guina, Dirk H. Sutter, and Thomas Dekorsy. Subpicosecond thin-disk laser oscillator with pulse energies of up to 25.9 microjoules by use of an active multipass geometry. *Optics Express*, 16(25):20530–20539, December 2008.
- [19] Dominik Bauer, Ivo Zawischa, Dirk H. Sutter, Alexander Killi, and Thomas Dekorsy. Mode-locked Yb:YAG thin-disk oscillator with 41  $\mu$ J pulse energy at 145 W average infrared power and high power frequency conversion. *Optics Express*, 20(9):9698–9704, April 2012.
- [20] Clara J. Saraceno, Florian Emaury, Cinia Schriber, Martin Hoffmann, Matthias Golling, Thomas Südmeyer, and Ursula Keller. Ultrafast thin-disk laser with 80  $\mu$ J pulse energy and 242 W of average power. *Optics Letters*, 39(1):9–12, January 2014.
- [21] Oleg Pronin, Jonathan Brons, Christian Grasse, Vladimir Pervak, Gerhard Boehm, Markus-Christian Amann, Vladimir L. Kalashnikov, Alexander Apolonski, and Ferenc Krausz. High-power 200 fs Kerr-lens mode-locked Yb:YAG thin-disk oscillator. *Optics Letters*, 36(24):4746–4748, December 2011.

- [22] O. Pronin, M. Seidel, F. Lücking, J. Brons, E. Fedulova, M. Trubetskov, V. Pervak, A. Apolonski, Th Udem, and F. Krausz. High-power multi-megahertz source of waveform-stabilized few-cycle light. *Nature Communications*, 6, May 2015.
- [23] E. Innerhofer, T. Südmeyer, F. Brunner, R. Häring, A. Aschwanden, R. Paschotta, C. Hönninger, M. Kumkar, and U. Keller. 60-W average power in 810-fs pulses from a thin-disk Yb: YAG laser. *Optics letters*, 28(5):367–369, 2003.
- [24] Felix Brunner, Edith Innerhofer, Sergio V. Marchese, Thomas Südmeyer, Rüdiger Paschotta, Takeshi Usami, Hiromasa Ito, Sunao Kurimura, Kenji Kitamura, Gunnar Arisholm, and others. Powerful red-green-blue laser source pumped with a mode-locked thin disk laser. *Optics letters*, 29(16):1921–1923, 2004.
- [25] Sergio V. Marchese, Thomas Südmeyer, Matthias Golling, Rachel Grange, and Ursula Keller. Pulse energy scaling to 5  $\mu$ J from a femtosecond thin disk laser. *Optics Letters*, 31(18):2728–2730, September 2006.
- [26] S. V. Marchese, C. R. Baer, A. G. Engqvist, S. Hashimoto, D. J. Maas, M. Golling, T. Südmeyer, and U. Keller. Femtosecond thin disk laser oscillator with pulse energy beyond the 10-microjoule level. *Optics Express*, 16(9):6397–6407, April 2008.
- [27] Clara J. Saraceno, Florian Emaury, Oliver H. Heckl, Cyrill R. E. Baer, Martin Hoffmann, Cinia Schriber, Matthias Golling, Thomas Südmeyer, and Ursula Keller. 275 W average output power from a femtosecond thin disk oscillator operated in a vacuum environment. *Optics Express*, 20(21):23535–23541, October 2012.
- [28] Jonathan Brons, Vladimir Pervak, Elena Fedulova, Dominik Bauer, Dirk Sutter, Vladimir Kalashnikov, Alexander Apolonskiy, Oleg Pronin, and Ferenc Krausz. Energy scaling of Kerr-lens mode-locked thin-disk oscillators. *Optics Letters*, 39(22):6442–6445, November 2014.
- [29] A. Amani Eilanlou, Yasuo Nabekawa, Makoto Kuwata-Gonokami, and Katsumi Midorikawa. Femtosecond laser pulses in a Kerr lens mode-locked thin-disk ring oscillator with an intra-cavity peak power beyond 100 MW. *Japanese Journal of Applied Physics*, 53(8):082701, August 2014.
- [30] Jinwei Zhang, Jonathan Brons, Marcus Seidel, Vladimir Pervak, Vladimir Kalashnikov, Zhiyi Wei, Alexander Apolonski, Ferenc Krausz, and Oleg Pronin. 49-fs Yb:YAG thin-disk oscillator with distributed Kerr-lens mode-locking. *postdeadline paper, CLEO Europe*, 2015.
- [31] Jinwei Zhang, Jonathan Brons, Nikolai Lilienfein, Elena Fedulova, Vladimir Pervak, Dominik Bauer, Dirk Sutter, Zhiyi Wei, Alexander Apolonski, Oleg

- Pronin, and Ferenc Krausz. 260-megahertz, megawatt-level thin-disk oscillator. *Optics Letters*, 40(8):1627, April 2015.
- [32] Jonathan Brons, Vladimir Pervak, Dominik Bauer, Dirk Sutter, Oleg Pronin, and Ferenc Krausz. Powerful 100-fs-scale Kerr-lens mode-locked thin-disk oscillator. *Optics Letters*, 41(15):3567, August 2016.
- [33] C. R. E. Baer, C. Kränkel, C. J. Saraceno, O. H. Heckl, M. Golling, T. Südmeyer, R. Peters, K. Petermann, G. Huber, and U. Keller. Femtosecond Yb:Lu<sub>2</sub>O<sub>3</sub> thin disk laser with 63 W of average power. *Optics Letters*, 34(18):2823–2825, 2009.
- [34] Cyrill Roman Emmanuel Baer, Christian Kränkel, Clara Jody Saraceno, Oliver Hubert Heckl, Matthias Golling, Rigo Peters, Klaus Petermann, Thomas Südmeyer, Günter Huber, and Ursula Keller. Femtosecond thin-disk laser with 141 W of average power. *Optics Letters*, 35(13):2302–2304, July 2010.
- [35] Bernhard Kreipe, José Andrade, Bastian Deppe, Christian Kränkel, and Uwe Morgner. Kerr-lens mode-locked Yb<sup>3+</sup>:Lu<sub>2</sub>O<sub>3</sub> thin-disk laser. page SM1I.4. OSA, 2016.
- [36] F. Brunner, Thomas Südmeyer, E. Innerhofer, F. Morier-Genoud, R. Paschotta, V. E. Kisel, V. G. Shcherbitsky, N. V. Kuleshov, J. Gao, K. Contag, A. Giesen, and U. Keller. 240-fs pulses with 22-W average power from a mode-locked thin-disk Yb:KY(WO<sub>4</sub>)<sub>2</sub> laser. *Optics Letters*, 27(13):1162–1164, July 2002.
- [37] A.-L. Calendron, K. S. Wentsch, and M. J. Lederer. High power cw and mode-locked oscillators based on Yb:KYW multi-crystal resonators. *Optics Express*, 16(23):18838, November 2008.
- [38] Guido Palmer, Marcel Schultze, Moritz Emons, Anna Lena Lindemann, Matthias Pospiech, Daniel Steingrube, Max Lederer, and Uwe Morgner. 12 MW peak power from a two-crystal Yb:KYW chirped-pulse oscillator with cavity-dumping. *Optics Express*, 18(18):19095–19100, August 2010.
- [39] Clara J. Saraceno, Oliver H. Heckl, Cyrill R. E. Baer, Matthias Golling, Thomas Südmeyer, Kolja Beil, Christian Kränkel, Klaus Petermann, Günter Huber, and Ursula Keller. SESAMs for high-power femtosecond modelocking: power scaling of an Yb:LuScO<sub>3</sub> thin disk laser to 23 W and 235 fs. *Optics Express*, 19(21):20288–20300, October 2011.
- [40] C. Saraceno, O. Heckl, C. Baer, C. Schriber, M. Golling, K. Beil, C. Kränkel, T. Südmeyer, G. Huber, and U. Keller. Sub-100 femtosecond pulses from a SESAM modelocked thin disk laser. *Applied Physics B: Lasers and Optics*, 106(3):559–562, March 2012.
- [41] Guido Palmer, Marcel Schultze, Martin Siegel, Moritz Emons, Udo Bünting, and Uwe Morgner. Passively mode-locked Yb:KLu(WO<sub>4</sub>)<sub>2</sub> thin-disk oscillator operated in the positive and negative dispersion regime. *Optics Letters*, 33(14):1608–1610, July 2008.

- [42] Katrin Sarah Wentsch, Lihe Zheng, Jun Xu, Marwan Abdou Ahmed, and Thomas Graf. Passively mode-locked Yb<sup>3+</sup>:Sc<sub>2</sub>SiO<sub>5</sub> thin-disk laser. *Optics Letters*, 37(22):4750–4752, November 2012.
- [43] Sandrine Ricaud, Anael Jaffres, Katrin Wentsch, Akiko Suganuma, Bruno Viana, P. Loiseau, Birgit Weichelt, Marwan Abdou-Ahmed, Andreas Voss, Thommas Graf, and others. Femtosecond Yb: CaGdAlO<sub>4</sub> thin-disk oscillator. *Optics letters*, 37(19):3984–3986, 2012.
- [44] Alessandro Greborio, Annalisa Guandalini, and Juerg Aus der Au. Sub-100 fs pulses with 12.5-W from Yb:CALGO based oscillators. In *Proc. SPIE*, volume 8235, San Francisco, California, USA, February 2012. International Society for Optics and Photonics.
- [45] Andreas Diebold, Florian Emaury, Cinia Schriber, Matthias Golling, Clara J. Saraceno, Thomas Südmeyer, and Ursula Keller. SESAM mode-locked Yb:CaGdAlO<sub>4</sub> thin disk laser with 62 fs pulse generation. *Optics Letters*, 38(19):3842–3845, October 2013.
- [46] Sujith Manjooran and Arkady Major. Generation of Sub-50 fs Pulses With > 1.5 MW of Peak Power From a Diode-Pumped Yb:CALGO Laser Oscillator. In *OSA Technical Digest (2016)*, page JTU5A.82. OSA, 2016.
- [47] Benjamin Dannecker, Marwan Abdou Ahmed, and Thomas Graf. SESAM-modelocked Yb:CaF<sub>2</sub> thin-disk-laser generating 285 fs pulses with 1.78 μJ of pulse energy. *Laser Physics Letters*, 13(5):055801, April 2016.
- [48] S Naumov, A Fernandez, R Graf, P Dombi, F Krausz, and A Apolonski. Approaching the microjoule frontier with femtosecond laser oscillators. *New Journal of Physics*, 7:216–216, October 2005.
- [49] S. Dewald, T. Lang, C. D. Schröter, R. Moshhammer, J. Ullrich, M. Siegel, and U. Morgner. Ionization of noble gases with pulses directly from a laser oscillator. *Optics Letters*, 31(13):2072–2074, July 2006.
- [50] L. Xu, G. Tempea, Ch. Spielmann, F. Krausz, A. Stingl, K. Ferencz, and S. Takano. Continuous-wave mode-locked Ti:sapphire laser focusable to  $5 \times 10^{13}$  W/cm<sup>2</sup>. *Optics Letters*, 23(10):789–791, May 1998.
- [51] Christoph Jocher, Tino Eidam, Steffen Hädrich, Jens Limpert, and Andreas Tünnermann. Sub 25 fs pulses from solid-core nonlinear compression stage at 250 W of average power. *Optics Letters*, 37(21):4407–4409, November 2012.
- [52] M. Nisoli, S. De Silvestri, and O. Svelto. Generation of high energy 10 fs pulses by a new pulse compression technique. *Applied Physics Letters*, 68(20):2793–2795, May 1996.
- [53] Steffen Hädrich, Marco Kienel, Michael Müller, Arno Klenke, Jan Rothhardt, Robert Klas, Thomas Gottschall, Tino Eidam, András Drozdy, Péter Jójárt,

- Zoltán Várallyay, Eric Cormier, Károly Osvay, Andreas Tünnermann, and Jens Limpert. Energetic sub-2-cycle laser with 216 W average power. *Optics Letters*, 41(18):4332, September 2016.
- [54] Peng He, Yangyang Liu, Kun Zhao, Hao Teng, Xinkui He, Pei Huang, Hangdong Huang, Shiyang Zhong, Yujiao Jiang, Shaobo Fang, Xun Hou, and Zhiyi Wei. High-efficiency supercontinuum generation in solid thin plates at 01 TW level. *Optics Letters*, 42(3):474, February 2017.
- [55] H. J. Bakker, P. C. M. Planken, L. Kuipers, and A. Lagendijk. Phase modulation in second-order nonlinear-optical processes. *Physical Review A*, 42(7):4085–4101, October 1990.
- [56] G. I. Stegeman, D. J. Hagan, and L. Torner.  $\chi(2)$  cascading phenomena and their applications to all-optical signal processing, mode-locking, pulse compression and solitons. *Optical and Quantum Electronics*, 28(12):1691–1740, December 1996.
- [57] M. Seidel, J. Brons, G. Arisholm, K. Fritsch, V. Pervak, and O. Pronin. Efficient High-Power Ultrashort Pulse Compression in Self-Defocusing Bulk Media. *submitted for publication*, 2017.
- [58] U. Keller. Ultrafast all-solid-state laser technology. *Applied Physics B*, 58(5):347–363, May 1994.
- [59] M. Piché, N. McCarthy, and F. Salin. Pulse narrowing in mode-locked lasers through polarization and transverse effects. 1990.
- [60] Francois Salin, Michel Piché, and Jeff Squier. Mode locking of Ti: Al<sub>2</sub>O<sub>3</sub> lasers and self-focusing: a Gaussian approximation. *Optics letters*, 16(21):1674–1676, 1991.
- [61] Michel Piché. Beam reshaping and self-mode-locking in nonlinear laser resonators. *Optics Communications*, 86(2):156–160, November 1991.
- [62] Jean-Claude Diels and Wolfgang Rudolph. *Ultrashort Laser Pulse Phenomena*. Academic Press, September 2006.
- [63] Robert W. Boyd. *Nonlinear Optics, Third Edition*. Academic Press, 3 edition, April 2008.
- [64] Andrew Weiner. *Ultrafast Optics*. Pure and Applied Optics. Wiley, 1 edition, June 2009.
- [65] Govind P. Agrawal. *Nonlinear Fiber Optics*. Academic Press, 5 edition, 2013.
- [66] Vladimir L. Kalashnikov. Chirped-Pulse Oscillators: Route to the Energy-Scalable Femtosecond Pulses. In *Solid State Laser*, pages 146 – 184. InTech, February 2012.

- [67] R. H. Stolen and Chinlon Lin. Self-phase-modulation in silica optical fibers. *Physical Review A*, 17(4):1448–1453, April 1978.
- [68] S. A. Planas, N. L. Pires Mansur, C. H. Brito Cruz, and H. L. Fragnito. Spectral narrowing in the propagation of chirped pulses in single-mode fibers. *Optics Letters*, 18(9):699–701, May 1993.
- [69] Jörg Neuhaus. *Passively mode-locked Yb:YAG thin-disk laser with active multipass geometry*. PhD thesis, 2009.
- [70] Hermann A Haus. Theory of mode locking with a fast saturable absorber. *Journal of Applied Physics*, 46(7):3049–3058, July 1975.
- [71] H.A. Haus. Mode-locking of lasers. *IEEE Journal of Selected Topics in Quantum Electronics*, 6(6):1173–1185, December 2000.
- [72] Ferenc Krausz, M. E. Fermann, Thomas Brabec, Peter F. Curley, M. Hofer, M. H. Ober, Christian Spielmann, E. Wintner, and A. J. Schmidt. Femtosecond solid-state lasers. *Journal of Quantum Electronics*, 28(10):2097–2122, 1992.
- [73] C. Hönniger, R. Paschotta, F. Morier-Genoud, M. Moser, and U. Keller. Q-switching stability limits of continuous-wave passive mode locking. *Journal of the Optical Society of America B*, 16(1):46–56, January 1999.
- [74] H. A. Haus, J. G. Fujimoto, and E. P. Ippen. Structures for additive pulse mode locking. *Journal of the Optical Society of America B*, 8(10):2068–2076, October 1991.
- [75] F. X Kärtner, J. Aus der Au, and U. Keller. Mode-locking with slow and fast saturable absorbers-what’s the difference? *IEEE Journal of Selected Topics in Quantum Electronics*, 4(2):159–168, April 1998.
- [76] V. L. Kalashnikov, E. Podivilov, A. Chernykh, and A. Apolonski. Chirped-pulse oscillators: theory and experiment. *Applied Physics B*, 83(4):503–510, June 2006.
- [77] Bob Proctor, Erik Westwig, and Frank Wise. Characterization of a Kerr-lens mode-locked Ti:sapphire laser with positive group-velocity dispersion. *Optics Letters*, 18(19):1654, October 1993.
- [78] F. Ö. Ilday, J. R. Buckley, W. G. Clark, and F. W. Wise. Self-Similar Evolution of Parabolic Pulses in a Laser. *Physical Review Letters*, 92(21):213902, May 2004.
- [79] V L Kalashnikov, E Podivilov, A Chernykh, S Naumov, A Fernandez, R Graf, and A Apolonski. Approaching the microjoule frontier with femtosecond laser oscillators: theory and comparison with experiment. *New Journal of Physics*, 7:217–217, October 2005.

- [80] S. H. Cho, F. X. Kärtner, U. Morgner, E. P. Ippen, J. G. Fujimoto, J.E. Cunningham, and W. H. Knox. Generation of 90-nJ pulses with a 4-MHz repetition-rate Kerr-lens mode-locked Ti:Al<sub>2</sub>O<sub>3</sub> laser operating with net positive and negative intracavity dispersion. *Optics Letters*, 26(8):560–562, April 2001.
- [81] Guido Palmer, Moritz Emons, Martin Siegel, Andy Steinmann, Marcel Schultze, Max Lederer, and Uwe Morgner. Passively mode-locked and cavity-dumped Yb:KY(WO<sub>4</sub>)<sub>2</sub> oscillator with positive dispersion. *Optics Express*, 15(24):16017–16021, November 2007.
- [82] V. Pervak, O. Pronin, O. Razskazovskaya, J. Brons, I. B. Angelov, M. K. Trubetskov, A. V. Tikhonravov, and F. Krausz. High-dispersive mirrors for high power applications. *Optics Express*, 20(4):4503–4508, February 2012.
- [83] Elena Fedulova, Kilian Fritsch, Jonathan Brons, Oleg Pronin, Tatiana Amotchkina, Michael Trubetskov, Ferenc Krausz, and Vladimir Pervak. Highly-dispersive mirrors reach new levels of dispersion. *Optics Express*, 23(11):13788, June 2015.
- [84] Oleg Pronin, Jonathan Brons, C. Grasse, Vladimir Pervak, G. Boehm, M.-C. Amann, Alexander Apolonski, Vladimir L. Kalashnikov, and F. Krausz. High-power Kerr-lens mode-locked Yb:YAG thin-disk oscillator in the positive dispersion regime. *Optics Letters*, 37(17):3543–3545, September 2012.
- [85] A. Diebold, T. Zengerle, C. G. E. Alfieri, C. Schriber, F. Emaury, M. Mangold, M. Hoffmann, C. J. Saraceno, M. Golling, D. Follman, G. D. Cole, M. Aspelmeyer, T. Südmeyer, and U. Keller. Optimized SESAMs for kilowatt-level ultrafast lasers. *Optics Express*, 24(10):10512, May 2016.
- [86] Clara Jody Saraceno. *Cutting-edge high-power ultrafast oscillators*. PhD thesis, Diss., Eidgenössische Technische Hochschule ETH Zürich, Nr. 20917, 2012, 2012.
- [87] W.H. Renninger and F.W. Wise. Fundamental Limits to Mode-Locked Lasers: Toward Terawatt Peak Powers. *IEEE Journal of Selected Topics in Quantum Electronics*, 21(1):1–8, January 2015.
- [88] Walter Koechner. Thermal lensing in a Nd: YAG laser rod. *Applied optics*, 9(11):2548–2553, 1970.
- [89] Walter Koechner. *Solid-State Laser Engineering*. Springer, 7 edition, 2006.
- [90] H. J. Eichler, A. Haase, R. Menzel, and A. Siemoneit. Thermal lensing and depolarization in a highly pumped Nd:YAG laser amplifier. *Journal of Physics D: Applied Physics*, 26(11):1884, 1993.
- [91] A. Giesen, H. Hügel, A. Voss, K. Wittig, U. Brauch, and H. Opower. Scalable concept for diode-pumped high-power solid-state lasers. *Applied Physics B*, 58(5):365–372, May 1994.

- 
- [92] Steffen Erhard. *Pumpoptiken und Resonatoren für den Scheibenlaser*. PhD thesis, Universität Stuttgart, Stuttgart, 2002.
- [93] Mikhail Larionov. *Kontaktierung und Charakterisierung von Kristallen für Scheibenlaser*. Herbert Utz Verlag, March 2009.
- [94] Sven-Silvius Schad, Christian Stolzenburg, Knut Michel, and Dirk Sutter. Latest Advances in High Brightness Disk Lasers. *Laser Technik Journal*, 11(2):49–53, 2014.
- [95] Kolja Beil, Susanne T. Fredrich-Thornton, Friedjof Tellkamp, Rigo Peters, Christian Kränkel, Klaus Petermann, and Günter Huber. Thermal and laser properties of Yb: LuAG for kW thin disk lasers. *Optics express*, 18(20):20712–20722, 2010.
- [96] K. Petermann, D. Fagundes-Peters, J. Johannsen, M. Mond, V. Peters, J.J. Romero, S. Kutovoi, J. Speiser, and A. Giesen. Highly Yb-doped oxides for thin-disc lasers. *Journal of Crystal Growth*, 275(1-2):135–140, February 2005.
- [97] R. Paschotta, J. Aus der Au, G.J. Spühler, S. Erhard, A. Giesen, and U. Keller. Passive mode locking of thin-disk lasers: effects of spatial hole burning. *Applied Physics B: Lasers and Optics*, 72(3):267–278, 2001.
- [98] Thomas Brabec, Stephen M. J. Kelly, and Ferenc Krausz. Passive modelocking in solid state lasers. In *Compact Sources of Ultrashort Pulses*, pages 57 – 92. Cambridge University Press, 1995.
- [99] K. Tamura, J. Jacobson, E. P. Ippen, H. A. Haus, and J. G. Fujimoto. Unidirectional ring resonators for self-starting passively mode-locked lasers. *Optics letters*, 18(3):220–222, 1993.
- [100] Norman Hodgson and Horst Weber. *Laser Resonators and Beam Propagation*, volume 108 of *Springer Series in Optical Sciences*. Springer-Verlag, New York, 2005.
- [101] D. C. Hanna, C. G. Sawyers, and M. A. Yuratich. Telescopic resonators for large-volume TEM00-mode operation. *Optical and Quantum Electronics*, 13(6):493–507, November 1981.
- [102] Vittorio Magni. Multielement stable resonators containing a variable lens. *Journal of the Optical Society of America A*, 4(10):1962–1969, October 1987.
- [103] E Ding, S Lefrancois, J N Kutz, and F W Wise. Scaling Fiber Lasers to Large Mode Area: An Investigation of Passive Mode-Locking Using a Multi-Mode Fiber. *IEEE Journal of Quantum Electronics*, 47(5):597–606, May 2011.
- [104] D. Georgiev, J. Herrmann, and U. Stamm. Cavity design for optimum nonlinear absorption in Kerr-lens mode-locked solid-state lasers. *Optics Communications*, 92(4–6):368–375, September 1992.

- 
- [105] T. Brabec, P. F. Curley, Ch. Spielmann, E. Wintner, and A. J. Schmidt. Hard-aperture Kerr-lens mode locking. *Journal of the Optical Society of America B*, 10(6):1029–1034, June 1993.
- [106] Vittorio Magni, Giulio Cerullo, and Sandro De Silvestri. ABCD matrix analysis of propagation of gaussian beams through Kerr media. *Optics Communications*, 96(4–6):348–355, February 1993.
- [107] T. Brabec, Ch. Spielmann, P. F. Curley, and F. Krausz. Kerr lens mode locking. *Optics Letters*, 17(18):1292–1294, September 1992.
- [108] Joachim Herrmann. Theory of Kerr-lens mode locking: role of self-focusing and radially varying gain. *Journal of the Optical Society of America B*, 11(3):498–512, March 1994.
- [109] S. Gatz and J. Herrmann. Astigmatism and gain guiding in Kerr-lens mode-locked lasers. *Optics Letters*, 20(8):825, April 1995.
- [110] A. Penzkofer, M. Wittmann, M. Lorenz, E. Siegert, and S. Macnamara. Kerr lens effects in a folded-cavity four-mirror linear resonator. *Optical and Quantum Electronics*, 28(4):423–442, April 1996.
- [111] S. Magne, Y. Ouerdane, M. Druetta, J. P. Goure, P. Ferdinand, and G. Monnom. Cooperative luminescence in an ytterbium-doped silica fibre. *Optics Communications*, 111(3–4):310–316, October 1994.
- [112] Dominik Bauer. *Modengekoppelte Scheibenoszillatoren für Materialbearbeitung*. PhD thesis, Universität Konstanz, 2012.
- [113] Franz X. Kärtner. *Few-Cycle Laser Pulse Generation and Its Applications*. Number 95 in Topics in Applied Physics. Springer, Berlin ; New York, 2004 edition, September 2004.
- [114] M. Becker, D. Kuizenga, and A. Siegman. Harmonic mode locking of the Nd:YAG laser. *IEEE Journal of Quantum Electronics*, 8(8):687–693, August 1972.
- [115] Joerg Neuhaus, Dominik Bauer, Jochen Kleinbauer, Alexander Killi, Dirk H. Sutter, and Thomas Dekorsy. Numerical analysis of a sub-picosecond thin-disk laser oscillator with active multipass geometry showing a variation of pulse duration within one round trip. *Journal of the Optical Society of America B*, 27(1):65–71, January 2010.
- [116] Joerg Neuhaus, Jochen Kleinbauer, Alexander Killi, Sascha Weiler, Dirk Sutter, and Thomas Dekorsy. Passively mode-locked Yb:YAG thin-disk laser with pulse energies exceeding 13  $\mu\text{J}$  by use of an active multipass geometry. *Optics Letters*, 33(7):726–728, April 2008.

- [117] Shiva Kumar, A. Selvarajan, and G. V. Anand. Nonlinear copropagation of two optical pulses of different frequencies in birefringent fibers. *Journal of the Optical Society of America B*, 11(5):810, May 1994.
- [118] Ling Yun, Xueming Liu, and Dongdong Han. Observation of vector- and scalar-pulse in a nanotube-mode-locked fiber laser. *Optics Express*, 22(5):5442, March 2014.
- [119] Y. Wang, S. Wang, J. Luo, Y. Ge, L. Li, D. Tang, D. Shen, S. Zhang, F. W. Wise, and L. Zhao. Vector Soliton Generation in a Tm Fiber Laser. *IEEE Photonics Technology Letters*, 26(8):769–772, April 2014.
- [120] H. A. Haus, I. Sorokina, and E. Sorokin. Raman-induced redshift of ultrashort mode-locked laser pulses. *Journal of the Optical Society of America B*, 15(1):223–231, January 1998.
- [121] Vladimir L. Kalashnikov, Evgeni Sorokin, and Irina T. Sorokina. Mechanisms of spectral shift in ultrashort-pulse laser oscillators. *Journal of the Optical Society of America B*, 18(11):1732–1741, November 2001.
- [122] C.J. Saraceno, F. Emaury, C. Schriber, A. Diebold, M. Hoffmann, M. Golling, T. Sudmeyer, and U. Keller. Toward Millijoule-Level High-Power Ultrafast Thin-Disk Oscillators. *IEEE Journal of Selected Topics in Quantum Electronics*, 21(1):1–18, January 2015.
- [123] Robert Adair, L. L. Chase, and Stephen A. Payne. Nonlinear refractive index of optical crystals. *Physical Review B*, 39(5):3337–3350, February 1989.
- [124] Arkady Major, Fumiyo Yoshino, Irkalis Nikolakakos, J. Stewart Aitchison, and Peter WE Smith. Dispersion of the nonlinear refractive index in sapphire. *Optics letters*, 29(6):602–604, 2004.
- [125] Marvin J. Weber. *Handbook of Optical Materials*. CRC Press, September 2002.
- [126] John Robertson. Band offsets of wide-band-gap oxides and implications for future electronic devices. *Journal of Vacuum Science & Technology B: Microelectronics and Nanometer Structures*, 18(3):1785, 2000.
- [127] Yong-Nian Xu and W. Y. Ching. Electronic structure of yttrium aluminum garnet  $Y_3Al_5O_{12}$ . *Physical Review B*, 59(16):10530–10535, April 1999.
- [128] Douglas B. Leviton, Bradley J. Frey, and Timothy J. Madison. Temperature-dependent refractive index of CaF<sub>2</sub> and Infrasil 301. *arXiv:0805.0096 [physics]*, May 2008. arXiv: 0805.0096.
- [129] Michael E Thomas, Stefan K Andersson, Raymond M Sova, and Richard I Joseph. Frequency and temperature dependence of the refractive index of sapphire. *Infrared Physics & Technology*, 39(4):235–249, June 1998.

- [130] Irving H. Malitson. Refraction and Dispersion of Synthetic Sapphire. *JOSA*, 52(12):1377–1379, December 1962.
- [131] Hanieh Fattahi, Haochuan Wang, Ayman Alismail, Gunnar Arisholm, Vladimir Pervak, Abdallah M. Azzeer, and Ferenc Krausz. Near-PHz-bandwidth, phase-stable continua generated from a Yb:YAG thin-disk amplifier. *Optics Express*, 24(21):24337, October 2016.
- [132] Hanieh Fattahi, Alexander Schwarz, Xiao Tao Geng, Sabine Keiber, Dong Eon Kim, Ferenc Krausz, and Nicholas Karpowicz. Decoupling chaotic amplification and nonlinear phase in high-energy thin-disk amplifiers for stable OPCPA pumping. *Optics Express*, 22(25):31440, December 2014.
- [133] Hanieh Fattahi, Ayman Alismail, Haochuan Wang, Jonathan Brons, Oleg Pronin, Theresa Buberl, Lénárd Vámos, Gunnar Arisholm, Abdallah M. Azzeer, and Ferenc Krausz. High-power, 1-ps, all-Yb:YAG thin-disk regenerative amplifier. *Optics Letters*, 41(6):1126, March 2016.
- [134] T. Südmeyer, C. Kränkel, C. Baer, O. Heckl, C. Saraceno, M. Golling, R. Peters, K. Petermann, G. Huber, and U. Keller. High-power ultrafast thin disk laser oscillators and their potential for sub-100-femtosecond pulse generation. *Applied Physics B: Lasers and Optics*, 97(2):281–295, October 2009.
- [135] Katrin Sarah Wentsch. *Analyse Ytterbium-dotierter Materialien für den Einsatz in ultrakurz-gepulsten Scheibenlasersystemen*. PhD thesis, Universität Stuttgart, Stuttgart, 2016.
- [136] Andreas Diebold, Florian Emaury, Clara J. Saraceno, Cinia Schriber, Matthias Golling, Thomas Südmeyer, and Ursula Keller. 62-fs Pulses from a SESAM Modelocked Yb:CALGO Thin Disk Laser. In G. and Moulton Huber, P., editor, *Advanced Solid-State Lasers Congress*, OSA Technical Digest (online), page AF3A.2. Optical Society of America, October 2013.
- [137] Kolja Beil, Clara J. Saraceno, Cinia Schriber, Florian Emaury, Oliver H. Heckl, Cyrill R. E. Baer, Matthias Golling, Thomas Südmeyer, Ursula Keller, Christian Kränkel, and Günter Huber. Yb-doped mixed sesquioxides for ultrashort pulse generation in the thin disk laser setup. *Applied Physics B*, 113(1):13–18, April 2013.
- [138] Cinia Schriber, Florian Emaury, Andreas Diebold, Sandro Link, Matthias Golling, Kolja Beil, Christian Kränkel, Clara J. Saraceno, Thomas Südmeyer, and Ursula Keller. Dual-gain SESAM modelocked thin disk laser based on Yb:Lu<sub>2</sub>O<sub>3</sub> and Yb:Sc<sub>2</sub>O<sub>3</sub>. *Optics Express*, 22(16):18979–18986, August 2014.
- [139] Masaki Tokurakawa, Akira Shirakawa, Ken-ichi Ueda, Hideki Yagi, Takagimi Yanagitani, Alexander A. Kaminskii, Kolja Beil, Christian Kränkel, and Günter Huber. Continuous wave and mode-locked Yb<sup>3+</sup>:Y<sub>2</sub>O<sub>3</sub> ceramic thin disk laser. *Optics Express*, 20(10):10847, May 2012.

- [140] O. H. Heckl, C. Kränkel, C. R. E. Baer, C. J. Saraceno, T. Südmeyer, K. Petermann, G. Huber, and U. Keller. Continuous-wave and modelocked Yb:YCOB thin disk laser: first demonstration and future prospects. *Optics Express*, 18(18):19201, August 2010.
- [141] Volker Peters. *Growth and Spectroscopy of Ytterbium-Doped Sesquioxides*. PhD thesis, Universität Hamburg, Hamburg, 2001.
- [142] Akio Ikesue and Yan Lin Aung. Ceramic laser materials. *Nature Photonics*, 2(12):721–727, December 2008.
- [143] Hiroaki Nakao, Tatsuya Inagaki, Akira Shirakawa, Ken-ichi Ueda, Hideki Yagi, Takagimi Yanagitani, Alexander A. Kaminskii, Birgit Weichelt, Katrin Wentsch, Marwan Abdou Ahmed, and Thomas Graf. Yb<sup>3+</sup>-doped ceramic thin-disk lasers of Lu-based oxides. *Optical Materials Express*, 4(10):2116, October 2014.
- [144] A. Lucca, G. Debourg, Mathieu Jacquemet, Frédéric Druon, François Balembois, Patrick Georges, Patrice Camy, Jean-Louis Doualan, and Richard Moncorgé. High-power diode-pumped Yb<sup>3+</sup>: CaF<sub>2</sub> 2 femtosecond laser. *Optics letters*, 29(23):2767–2769, 2004.
- [145] Johan Petit, Philippe Goldner, and Bruno Viana. Laser emission with low quantum defect in Yb: CaGdAlO<sub>4</sub>. *Optics letters*, 30(11):1345–1347, 2005.
- [146] Kolja Beil, Bastian Deppe, and Christian Kränkel. Yb:CaGdAlO<sub>4</sub> thin-disk laser with 70% slope efficiency and 90 nm wavelength tuning range. *Optics Letters*, 38(11):1966–1968, June 2013.
- [147] P. Sévillano, P. Georges, F. Druon, D. Descamps, and E. Cormier. 32-fs Kerr-lens mode-locked Yb:CaGdAlO<sub>4</sub> oscillator optically pumped by a bright fiber laser. *Optics Letters*, 39(20):6001–6004, October 2014.
- [148] F. Krausz, T. Brabec, and Ch. Spielmann. Self-starting passive mode locking. *Optics Letters*, 16(4):235–237, February 1991.
- [149] J. Zehetner, Ch. Spielmann, and F. Krausz. Passive mode locking of homogeneously and inhomogeneously broadened lasers. *Optics Letters*, 17(12):871–873, June 1992.
- [150] Clara Saraceno, Cinia Schriber, Florian Emaury, Oliver Heckl, Cyrill Baer, Martin Hoffmann, Kolja Beil, Christian Kränkel, Matthias Golling, Thomas Südmeyer, and Ursula Keller. Cutting-Edge High-Power Ultrafast Thin Disk Oscillators. *Applied Sciences*, 3(2):355–395, April 2013.
- [151] D. H. Sutter, G. Steinmeyer, L. Gallmann, N. Matuschek, F. Morier-Genoud, U. Keller, V. Scheuer, G. Angelow, and T. Tschudi. Semiconductor saturable-absorber mirror-assisted Kerr-lens mode-locked Ti:sapphire laser producing pulses in the two-cycle regime. *Optics Letters*, 24(9):631, May 1999.

- [152] U. Morgner, Franz X. Kärtner, S. H. Cho, Y. Chen, H. A. Haus, J. G. Fujimoto, E. P. Ippen, V. Scheuer, G. Angelow, and T. Tschudi. Sub-two-cycle pulses from a Kerr-lens mode-locked Ti:sapphire laser. *Optics Letters*, 24(6):411–413, March 1999.
- [153] R. Ell, U. Morgner, Franz X. Kärtner, J. G. Fujimoto, E. P. Ippen, V. Scheuer, G. Angelow, T. Tschudi, M. J. Lederer, A. Boiko, and B. Luther-Davies. Generation of 5-fs pulses and octave-spanning spectra directly from a Ti:sapphire laser. *Optics Letters*, 26(6):373–375, March 2001.
- [154] N. Minkovski, G. I. Petrov, S. M. Saltiel, O. Albert, and J. Etchepare. Nonlinear polarization rotation and orthogonal polarization generation experienced in a single-beam configuration. *JOSA B*, 21(9):1659–1664, September 2004.
- [155] Theresa Buberl, Ayman Alismail, Haochuan Wang, Nicholas Karpowicz, and Hanieh Fattahi. Self-compressed, spectral broadening of a Yb:YAG thin-disk amplifier. *Optics Express*, 24(10):10286, May 2016.
- [156] Aurélie Jullien, Olivier Albert, Frédéric Burgy, Guy Hamoniaux, Jean-Philippe Rousseau, Jean-Paul Chambaret, Frédérique Augé-Rochereau, Gilles Chériaux, Jean Etchepare, Nikolay Minkovski, and Solomon M. Saltiel.  $10^{-10}$  temporal contrast for femtosecond ultraintense lasers by cross-polarized wave generation. *Optics Letters*, 30(8):920, April 2005.
- [157] T. Südmeyer, F. Brunner, E. Innerhofer, R. Paschotta, K. Furusawa, J. C. Baggett, T. M. Monro, D. J. Richardson, and U. Keller. Nonlinear femtosecond pulse compression at high average power levels by use of a large-mode-area holey fiber. *Optics Letters*, 28(20):1951–1953, October 2003.
- [158] Ka Fai Mak. *Nonlinear optical effects in gas-filled hollow-core photonic-crystal fibers*. PhD thesis, Friedrich-Alexander-Universität Erlangen-Nürnberg (FAU), 2014.
- [159] Maximilian Bradler. *Bulk continuum generation: the ultimate tool for laser applications and spectroscopy*. Text.PhDThesis, Ludwig-Maximilians-Universität München, September 2014.
- [160] L. F. Mollenauer, W. J. Tomlinson, R. H. Stolen, and J. P. Gordon. Extreme picosecond pulse narrowing by means of soliton effect in single-mode optical fibers. *Optics Letters*, 8(5):289–291, May 1983.
- [161] Dimitre G. Ouzounov, Christopher J. Hensley, Alexander L. Gaeta, Natesan Venkateraman, Michael T. Gallagher, and Karl W. Koch. Soliton pulse compression in photonic band-gap fibers. *Optics Express*, 13(16):6153, 2005.
- [162] K. F. Mak, J. C. Travers, N. Y. Joly, A. Abdolvand, and P. St J. Russell. Two techniques for temporal pulse compression in gas-filled hollow-core kagomé photonic crystal fiber. *Optics Letters*, 38(18):3592–3595, September 2013.

- [163] A. V. Smith, B. T. Do, G. R. Hadley, and R. L. Farrow. Optical Damage Limits to Pulse Energy From Fibers. *IEEE Journal of Selected Topics in Quantum Electronics*, 15(1):153–158, January 2009.
- [164] T. Ganz, V. Pervak, A. Apolonski, and P. Baum. 16 fs, 350 nJ pulses at 5 MHz repetition rate delivered by chirped pulse compression in fibers. *Optics Letters*, 36(7):1107, April 2011.
- [165] Thomas Ganz. *Supercontinuum generation by chirped pulse compression for ultrafast spectroscopy and broadband near-field microscopy*. Text.PhDThesis, Ludwig-Maximilians-Universität München, October 2011.
- [166] Fetah Benabid, J. C. Knight, G. Antonopoulos, and P. St. J. Russell. Stimulated Raman Scattering in Hydrogen-Filled Hollow-Core Photonic Crystal Fiber. *Science*, 298(5592):399–402, October 2002.
- [167] F. Couny, Fetah Benabid, P. J. Roberts, P. S. Light, and M. G. Raymer. Generation and Photonic Guidance of Multi-Octave Optical-Frequency Combs. *Science*, 318(5853):1118–1121, November 2007.
- [168] Muhammad Nurhuda, Akira Suda, Katsumi Midorikawa, Masatoshi Hatayama, and Keigo Nagasaka. Propagation dynamics of femtosecond laser pulses in a hollow fiber filled with argon: constant gas pressure versus differential gas pressure. *JOSA B*, 20(9):2002–2011, September 2003.
- [169] K. F. Mak, M. Seidel, O. Pronin, M. H. Frosz, A. Abdolvand, V. Pervak, A. Apolonski, F. Krausz, J. C. Travers, and P. St. J. Russell. Compressing  $\mu\text{J}$ -level pulses from 250 fs to sub-10 fs at 38-MHz repetition rate using two gas-filled hollow-core photonic crystal fiber stages. *Optics Letters*, 40(7):1238–1241, April 2015.
- [170] Marcus Seidel, Gunnar Arisholm, Jonathan Brons, Vladimir Pervak, and Oleg Pronin. All solid-state spectral broadening: an average and peak power scalable method for compression of ultrashort pulses. *Optics Express*, 24(9):9412–9428, May 2016.
- [171] Florian Emaury, Clara J. Saraceno, Benoit Debord, Debashri Ghosh, Andreas Diebold, Frederic Gèrôme, Thomas Südmeyer, Fetah Benabid, and Ursula Keller. Efficient spectral broadening in the 100-W average power regime using gas-filled kagome HC-PCF and pulse compression. *Optics Letters*, 39(24):6843, December 2014.
- [172] Thomas Brabec and Ferenc Krausz. Intense few-cycle laser fields: Frontiers of nonlinear optics. *Reviews of Modern Physics*, 72(2):545–591, April 2000.
- [173] E. A. J. Marcatili and R. A. Schmeltzer. Hollow Metallic and Dielectric Waveguides for Long Distance Optical Transmission and Lasers. *Bell System Technical Journal*, 43:1783–1809, July 1964.

- [174] C. P. Hauri, W. Kornelis, F. W. Helbing, A. Heinrich, A. Couairon, A. Mysyrowicz, J. Biegert, and U. Keller. Generation of intense, carrier-envelope phase-locked few-cycle laser pulses through filamentation. *Applied Physics B*, 79(6):673–677, September 2004.
- [175] E. Goulielmakis, S. Koehler, B. Reiter, M. Schultze, A. J. Verhoef, E. E. Serebryannikov, A. M. Zheltikov, and F. Krausz. Ultrabroadband, coherent light source based on self-channeling of few-cycle pulses in helium. *Optics Letters*, 33(13):1407, July 2008.
- [176] F. Silva, D. R. Austin, A. Thai, M. Baudisch, M. Hemmer, D. Faccio, A. Couairon, and J. Biegert. Multi-octave supercontinuum generation from mid-infrared filamentation in a bulk crystal. *Nature Communications*, 3:807, May 2012.
- [177] Claude Rolland and P. B. Corkum. Compression of high-power optical pulses. *Journal of the Optical Society of America B*, 5(3):641–647, March 1988.
- [178] Chih-Hsuan Lu, Yu-Jung Tsou, Hong-Yu Chen, Bo-Han Chen, Yu-Chen Cheng, Shang-Da Yang, Ming-Chang Chen, Chia-Chen Hsu, and A. H. Kung. Generation of intense supercontinuum in condensed media. *Optica*, 1(6):400–406, December 2014.
- [179] Florian Emaury, Andreas Diebold, Clara J. Saraceno, and Ursula Keller. Compact extreme ultraviolet source at megahertz pulse repetition rate with a low-noise ultrafast thin-disk laser oscillator. *Optica*, 2(11):980, November 2015.
- [180] Philippe Lassonde, Sergey Mironov, Sylvain Fourmaux, Stéphane Payeur, Efim Khazanov, Alexander Sergeev, Jean-Claude Kieffer, and Gerard Mourou. High energy femtosecond pulse compression. *Laser Physics Letters*, 13(7):075401, 2016.
- [181] Jan Schulte, Thomas Sartorius, Johannes Weitenberg, Andreas Vernaleken, and Peter Russbueldt. Nonlinear pulse compression in a multi-pass cell. *Optics Letters*, 41(19):4511, October 2016.
- [182] Richard DeSalvo, H. Vanherzeele, D. J. Hagan, M. Sheik-Bahae, G. Stegeman, and E. W. Van Stryland. Self-focusing and self-defocusing by cascaded second-order effects in KTP. *Optics letters*, 17(1):28–30, 1992.
- [183] Xiang Liu, Liejia Qian, and Frank Wise. High-energy pulse compression by use of negative phase shifts produced by the cascade  $\chi(2)$ :  $\chi(2)$  nonlinearity. *Optics letters*, 24(23):1777–1779, 1999.
- [184] Andy Steinmann, Alexander Killi, Guido Palmer, Thomas Binhammer, and Uwe Morgner. Generation of few-cycle pulses directly from a MHz-NOPA. *Optics Express*, 14(22):10627, 2006.

- 
- [185] D. Herrmann, C. Homann, R. Tautz, M. Scharrer, P. St.J. Russell, F. Krausz, L. Veisz, and E. Riedle. Approaching the full octave: noncollinear optical parametric chirped pulse amplification with two-color pumping. *Optics Express*, 18(18):18752, August 2010.
- [186] Anne Harth, Marcel Schultze, Tino Lang, Thomas Binhammer, Stefan Rausch, and Uwe Morgner. Two-color pumped OPCPA system emitting spectra spanning 15 octaves from VIS to NIR. *Optics Express*, 20(3):3076, January 2012.
- [187] Marcel Schultze, Thomas Binhammer, Andy Steinmann, Guido Palmer, Moritz Emons, and Uwe Morgner. Few-cycle OPCPA system at 143 kHz with more than 1  $\mu\text{J}$  of pulse energy. *Optics Express*, 18(3):2836, February 2010.
- [188] Jack D. Gaskill. *Linear systems, Fourier transforms, and optics*. Wiley, June 1978.
- [189] Amnon Yariv. *Quantum Electronics*. Wiley, New York, 3 edition edition, January 1989.
- [190] Li Yan, Yuan-Qun Liu, and C. H. Lee. Pulse temporal and spatial chirping by a bulk Kerr medium in a regenerative amplifier. *IEEE Journal of Quantum Electronics*, 30(9):2194–2202, September 1994.
- [191] Nenad Milosevic, Gabriel Tempea, and Thomas Brabec. Optical pulse compression: bulk media versus hollow waveguides. *Optics letters*, 25(9):672–674, 2000.
- [192] Andreas Vernaleken, Peter Russbüldt, Thomas Sartorius, Jan Schulte, and Johannes Weitenberg. Verfahren und Anordnung zur spektralen Verbreiterung von Laserpulsen für die nichtlineare Pulskompression, November 2015. CIB: H01S3/10; H01S3/23.
- [193] Rüdiger Paschotta. Beam quality deterioration of lasers caused by intracavity beam distortions. *Optics express*, 14(13):6069–6074, 2006.
- [194] Thomas Brabec and Ferenc Krausz. Nonlinear Optical Pulse Propagation in the Single-Cycle Regime. *Physical Review Letters*, 78(17):3282–3285, April 1997.
- [195] Jinendra K. Ranka and Alexander L. Gaeta. Breakdown of the slowly varying envelope approximation in the self-focusing of ultrashort pulses. *Optics Letters*, 23(7):534, April 1998.
- [196] Joshua E. Rothenberg. Space–time focusing: breakdown of the slowly varying envelope approximation in the self-focusing of femtosecond pulses. *Optics Letters*, 17(19):1340, October 1992.

- [197] Steffen Hädrich, Manuel Krebs, Armin Hoffmann, Arno Klenke, Jan Rothhardt, Jens Limpert, and Andreas Tünnermann. Exploring new avenues in high repetition rate table-top coherent extreme ultraviolet sources. *Light: Science & Applications*, 4(8):e320, August 2015.
- [198] Donald R. Herriott and Harry J. Schulte. Folded Optical Delay Lines. *Applied Optics*, 4(8):883–889, August 1965.
- [199] C. Dorrer, R. G. Roides, J. Bromage, and J. D. Zuegel. Self-phase modulation compensation in a regenerative amplifier using cascaded second-order nonlinearities. *Optics Letters*, 39(15):4466–4469, August 2014.
- [200] George I. Stegeman, Mansoor Sheik-Bahae, Eric Van Stryland, and Gaetano Assanto. Large nonlinear phase shifts in second-order nonlinear-optical processes. *Optics Letters*, 18(1):13–15, January 1993.
- [201] Morten Bache, Hairun Guo, Binbin Zhou, and Xianglong Zeng. The anisotropic Kerr nonlinear refractive index of the beta-barium borate ( $\beta$ -BaB<sub>2</sub>O<sub>4</sub>) nonlinear crystal. *Optical Materials Express*, 3(3):357–382, March 2013.
- [202] Fatih Ö Ilday, Kale Beckwitt, Yi-Fan Chen, Hyungsik Lim, and Frank W. Wise. Controllable Raman-like nonlinearities from nonstationary, cascaded quadratic processes. *JOSA B*, 21(2):376–383, 2004.
- [203] Kale Beckwitt. *Stationary and non-stationary cascaded interactions in quadratic nonlinear optical media: theory and applications*. Thesis, July 2004.
- [204] A. Gerrard and J. M. Burch. *Introduction to Matrix Methods in Optics*. Dover Books on Physics, New York, revised. edition, May 1994.
- [205] A. G. Fox and Tingye Li. Resonant Modes in a Maser Interferometer. *Bell System Technical Journal*, 40(2):453–488, March 1961.
- [206] Joseph W. Goodman. *Introduction to Fourier Optics*. W. H. Freeman, Englewood, Colo, 3 edition edition, December 2004.
- [207] A. Couairon, E. Brambilla, T. Corti, D. Majus, O. de J. Ramírez-Góngora, and M. Kolesik. Practitioner’s guide to laser pulse propagation models and simulation: Numerical implementation and practical usage of modern pulse propagation models. *The European Physical Journal Special Topics*, 199(1):5–76, November 2011.
- [208] Manuel Guizar-Sicairos and Julio C. Gutiérrez-Vega. Computation of quasi-discrete Hankel transforms of integer order for propagating optical wave fields. *JOSA A*, 21(1):53–58, January 2004.
- [209] William H. Press, Saul A. Teukolsky, William T. Vetterling, and Brian P. Flannery. *Numerical Recipes 3rd Edition: The Art of Scientific Computing*. Cambridge University Press, Cambridge, UK ; New York, 3 edition, September 2007.

- [210] I. H. Malitson. Interspecimen Comparison of the Refractive Index of Fused Silica. *Journal of the Optical Society of America*, 55(10):1205, October 1965.



## List of publications

### Peer reviewed journal articles

- M. Seidel, *J. Brons*, G. Arisholm, K. Fritsch, V. Pervak, and O. Pronin, "Efficient High-Power Ultrashort Pulse Compression in Self-Defocusing Bulk Media," *submitted for publication* (2017)
- T. Nubbemeyer, M. Kaumanns, M. Ueffing, M. Gorjan, A. Alismail, H. Fattahi, *J. Brons*, O. Pronin, H. G. Barros, Z. Major, T. Metzger, D. Sutter, and F. Krausz, "All thin-disk based 1kW, 200mJ regenerative laser amplifier," *submitted for publication* (2017)
- *J. Brons*, V. Pervak, D. Bauer, D. Sutter, O. Pronin, and F. Krausz, "Powerful 100-fs-scale Kerr-lens mode-locked thin-disk oscillator," *Opt. Lett.* 41, 3567 (2016)
- M. Seidel, G. Arisholm, *J. Brons*, V. Pervak, and O. Pronin, "All solid-state spectral broadening: an average and peak power scalable method for compression of ultrashort pulses," *Opt. Express.* 24, 9412–9428 (2016)
- M. Seidel, *J. Brons*, F. Lücking, V. Pervak, A. Apolonski, T. Udem, and O. Pronin, "Carrier-envelope-phase stabilization via dual wavelength pumping," *Opt. Lett.* 41, 1853–1856 (2016)
- H. Fattahi, A. Alismail, H. Wang, *J. Brons*, O. Pronin, T. Buberl, L. Vámos, G. Arisholm, A. M. Azzeer, and F. Krausz, "High-power, 1-ps, all-Yb:YAG thin-disk regenerative amplifier," *Opt. Lett.* 41, 1126 (2016)
- E. Fedulova, K. Fritsch, *J. Brons*, O. Pronin, T. Amotchkina, M. Trubetskov, F. Krausz, and V. Pervak, "Highly-dispersive mirrors reach new levels of dispersion," *Opt. Express* 23, 13788 (2015)
- O. Pronin, M. Seidel, F. Lücking, *J. Brons*, E. Fedulova, M. Trubetskov, V. Pervak, A. Apolonski, T. Udem, and F. Krausz, "High-power multi-megahertz source of waveform-stabilized few-cycle light," *Nat. Commun.* 6, (2015)
- J. Zhang, *J. Brons*, N. Lilienfein, E. Fedulova, V. Pervak, D. Bauer, D. Sutter, Z. Wei, A. Apolonski, O. Pronin, and F. Krausz, "260-megahertz, megawatt-level thin-disk oscillator," *Opt. Lett.* 40, 1627 (2015)
- *J. Brons*, V. Pervak, E. Fedulova, D. Bauer, D. Sutter, V. Kalashnikov, A. Apolonskiy, O. Pronin, and F. Krausz, "Energy scaling of Kerr-lens mode-locked thin-disk oscillators," *Opt. Lett.* 39, 6442–6445 (2014)

- H. Fattahi, H. G. Barros, M. Gorjan, T. Nubbemeyer, B. Alsaif, C. Y. Teisset, M. Schultze, S. Prinz, M. Haefner, M. Ueffing, A. Alismail, L. Vámos, A. Schwarz, O. Pronin, *J. Brons*, X. T. Geng, G. Arisholm, M. Ciappina, V. S. Yakovlev, D.-E. Kim, A. M. Azzeer, N. Karpowicz, D. Sutter, Z. Major, T. Metzger, and F. Krausz, "Third-generation femtosecond technology," *Optica* 1, 45–63 (2014)
- V. Pervak, O. Pronin, O. Razskazovskaya, *J. Brons*, I. B. Angelov, M. K. Trubetskov, A. V. Tikhonravov, and F. Krausz, "High-dispersive mirrors for high power applications," *Opt. Express* 20, 4503–4508 (2012)
- O. Pronin, *J. Brons*, C. Grasse, V. Pervak, G. Boehm, M.-C. Amann, A. Apolonski, V. L. Kalashnikov, and F. Krausz, "High-power Kerr-lens mode-locked Yb:YAG thin-disk oscillator in the positive dispersion regime," *Opt. Lett.* 37, 3543–3545 (2012)
- O. Pronin, *J. Brons*, C. Grasse, V. Pervak, G. Boehm, M.-C. Amann, V. L. Kalashnikov, A. Apolonski, and F. Krausz, "High-power 200 fs Kerr-lens mode-locked Yb:YAG thin-disk oscillator," *Opt. Lett.* 36, 4746–4748 (2011)

#### **Selected conference talks**

- *J. Brons*, V. Pervak, M. Seidel, D. Bauer, D. Sutter, O. Pronin, and F. Krausz, "Amplification-free, 145 MW, 16 MHz Scalable Ultrafast Light-source for XUV and MIR Generation," *Advanced Solid State Lasers* ATh3A.1 (2015) postdeadline
- *J. Brons*, V. Pervak, E. Fedulova, M. Seidel, D. Bauer, D. H. Sutter, V. L. Kalashnikov, A. Apolonskiy, O. Pronin, and F. Krausz, "Power-scaling of Kerr-lens mode-locked Yb:YAG thin-disk oscillators," *Europhoton* (2014) invited

## Data archiving

The experimental data, evaluation-files and figures can be found on the data archive server of the Laboratory for Attosecond Physics at the Max Planck Institute of Quantum Optics. The root directory contains folders named after each figure in the thesis (`/figure1.1`, `/figure1.2`, ...). Each folder contains the original data, the figure-image as included in the thesis and evaluation-files where applicable. A text-file named after the sub-figures (`figureX.x.txt`, `figureX.x_right.txt` ...) is included with instructions for each figure.



## Danksagung

Zuallererst muss ich mich bei Prof. Ferenc Krausz bedanken, der mir die Möglichkeit geboten hat, mich mit so einem interessanten Thema in einer großartigen Arbeitsumgebung und mit top Ausrüstung zu beschäftigen.

Gleich zunächst folgt natürlich Oleg Pronin, der mich seit dem Beginn meiner Arbeit zu jeder Zeit unterstützt und mir die Grundlagen beigebracht hat, Teflonband und Spiegelputztücher inbegriffen. Ohne seinen Rat und seine Erfahrung hätte diese Arbeit nicht erfolgreich sein können.

Auch besonders erwähnen muss ich Vladimir Pervak, der mich seit Beginn begleitet und stets mit Spiegeln unterstützt hat.

Großer Dank geht auch an meinen langjährigen Kollegen Markus Seidel für die vielen hilfreichen Einsichten, Gespräche und seinen außerordentlich gut organisierten Geburtstagskalender. Dem ganzen Oszillatorteam für die angenehme Atmosphäre in unserer Kleinstadt im zweiten Stock und die regelmäßigen Kuchen, die ihr gezwungen wart, mit mir zu teilen (Danke Kalender). Ich stehe auch besonders in der Schuld von Kilian Fritsch und Tobias Rumpf, die mir bei den spektralen Verbreiterungsversuchen und vielen anderen Dingen geholfen haben.

Vielen Dank an Hanieh für die vielen Erklärungen und den steten Wunsch unseren Alltag zu erheitern.

Danke dem Verstärkerteam, besonders Martin, Thomas und Moritz, dass sie mich in ihre hohen Hallen gelassen und mir gezeigt haben, wie man die Türe auch ohne Mondlicht aufmacht. Insbesondere möchte ich Moritz danken, dass er stets bereit war, seine Erfahrung, Platz und Equipment mit mir zu teilen. Auch bei Florian Saran möchte ich mich bedanken, für seine ständige Bereitschaft, den Kran zu bedienen und im Labor zu helfen.

Danken möchte ich ebenfalls Simon Holzberger, Henning Carstens, Tobias Saule und Nikolai Lilienfein, die stets bereit waren, meine Fragen zu beantworten und mit dem einen oder anderen Spiegel auszuweichen.

Auch Dirk Sutter und Dominik Bauer möchte ich für ihre stete Hilfsbereitschaft und ihre Geduld mit kurzfristigen Manuskriptrevisionen danken.

Den größten Dank von allen bin ich allerdings meinen Kindern und meiner Frau schuldig, die mich während dieser ganzen Arbeit getragen haben.